論文 / 著書情報
Article / Book Information

題目(和文)	伸展可能な折り紙の部材の干渉と変形を考慮した運動特性解析と伸展機構への応用
Title(English)	Kineto-elasto-static characterization of a deployable origami and its application to extendable mechanisms
著者(和文)	松尾博史
Author(English)	Hiroshi Matsuo
出典(和文)	学位:博士（工学）, 学位授与機関:東京工業大学, 報告番号:甲第11980号, 授与年月日:2021年3月26日, 学位の種別:課程博士, 審査員:武田 行生,菅原 雄介,岩附 信行,遠藤 玄,坂本 啓,松浦 大輔
Citation(English)	Degree:Doctor (Engineering), Conferring organization: Tokyo Institute of Technology, Report number:甲第11980号, Conferred date:2021/3/26, Degree Type:Course doctor, Examiner:,,,,,
学位種別(和文)	博士論文
Type(English)	Doctoral Thesis

Kineto-elasto-static characterization of a deployable origami and its application to extendable mechanisms

伸展可能な折り紙の部材の干渉と変形を考慮した運動特性解析と伸展機構への応用

Hiroshi Matsuo

DISSERTATION

Presented to
The Graduate major of Engineering Sciences and Design,
The Department of Mechanical Engineering,
The School of Engineering of Tokyo Institute of Technology
in partial fulfillment of the requirements
for the degree of

DOCTOR OF ENGINEERING

Tokyo Institute of Technology

March 2021

Approved by:

Dr. Nobuyuki Iwatsuki
Professor
Department of Mechanical Engineering
School of Engineering

Dr. Gen Endo
Associate Professor
Department of Mechanical Engineering
School of Engineering

Dr. Hiraku Sakamoto
Associate Professor
Department of Mechanical Engineering
School of Engineering

Dr. Daisuke Matsuura
Associate Professor
Department of Mechanical Engineering
School of Engineering

Dr. Yusuke Sugahara
Associate Professor
Department of Mechanical Engineering
School of Engineering

Dr. Yukio Takeda
Professor [Academic Supervisor]
Department of Mechanical Engineering
School of Engineering

Abstract

Soft-deployable origami structure is one of the types of deployable origami structure and can generate a multiple degree-of-freedom (DOF) motion with the deformation of components. It is expected to be applied to extendable devices, but its kinematic and mechanical characteristics have not been sufficiently revealed. A soft-deployable origami structure: Origami Spring is selected as the subject in this research, which can be modelled as a three DOF mechanism but performs like a single DOF mechanism. The objective of this research is to reveal the kineto-elastostatic characteristics of Origami Spring by modelling it with rigid and compliant components and revolute joints to consider the collision and deformation of components, which enables its design for extendable applications. Based on the revealed characteristics, to propose design strategies of extendable mechanisms inspired by a deployable origami beyond the characteristics of the original origami through the design of extendable mechanisms for two applications and their experimental studies is also the objective of this research. This thesis consists of 6 chapters.

In chapter 1 “Introduction”, the background and related researches of this research, the objective and contribution of this thesis, and thesis overview were introduced.

In chapter 2 “Origami Spring”, the basic definition and features of Origami Spring were introduced. Origami Spring consists of the right-angled triangles. The side of right-angled triangles which must deform due to the collision between other sides was identified, and the models of Origami Spring were fabricated by replacing the sides with rigid materials except the identified side. The extension motions of the fabricated models were compared with that of a paper model, and the validity of the structure was shown. In addition, the modifications of the folding diagram were introduced and their effects on the motion and shape were discussed.

In chapter 3 “Characterization with Consideration to Collision and Deformation of Components”, the three DOF spatial mechanism was proposed as the kinematic model of Origami Spring, consisting of the rigid and compliant components and revolute joints, based on the models which were fabricated in chapter 2. The con-

figuration space of the mechanism was derived with consideration to the collision between each rigid component, and the following were theoretically revealed; the thickness of components affects the range of extension motion, and the shape of Origami Spring is bending along the extension. In addition, the effect of the deformation of compliant components, which is caused by the collision between each compliant component, was evaluated by the strain energy of compliant components. It was revealed that the observed single DOF motion of Origami Spring can be explained by the magnitude and distribution of the strain energy with the deformation of components.

In chapter 4 "Application to an Extendable Arm for Working in a Narrow Space", assuming an application to an extendable arm for working in a narrow space, the multiple DOF extendable mechanism was designed inspired by Origami Spring, which has a large extension ratio and a sufficient load capacity and can generate various configurations, including a large curvature configuration. Based on the result in the chapter 3, the extendable mechanism was modified to remove the deformation of components, reduce the collision between each component, and enable the mechanism to generate a large curvature configuration. The actuated prototype of the extendable arm with five DOF was fabricated, and the motion experiments showed that the extendable arm can generate a desired configuration. In addition, the tapered extendable arm was fabricated based on the modification of the folding diagram which was introduced in the chapter 2, and its positional stability and static performance were revealed by the experiments and the theoretical analysis.

In chapter 5 "Application to an Assistive Device for Fall Prevention", assuming an application to an assistive device for older people to prevent a fracture by a fall, the actuation strategy of the extendable mechanism inspired by Origami Spring to achieve rapid extension and high load capacity in one mechanism was proposed focusing on the difference of the velocity ratio of output to input depending on where the mechanism is actuated. Based on the strategy, the prototype was fabricated where the pneumatic actuators for rapid extension and the lock elements to fix the extended configuration were installed. Through the experimental studies with this prototype, the desired rapid extension was achieved and the impact load

characteristic assuming fall prevention was revealed.

In chapter 6 “Conclusions and Future Work”, the conclusions of this thesis, the outlook for the future, and the obtained and remaining problems were discussed.

Contents

1 Introduction **1**

1.1 Background 1

1.1.1 Deployable origami structures 1

1.1.2 Potential application of a deployable origami to extendable mechanisms 5

1.2 Objective and Contribution of the Thesis 10

1.3 Thesis Overview 12

2 Origami Spring **13**

2.1 Folding Diagram 13

2.2 Motion and Structure 14

2.3 Modification of Folding Diagram 16

2.4 Summary 19

3 Characterization with Consideration to Collision and Deformation of Components **20**

3.1 Degrees of Freedom and Kinematic Model 20

3.2 Extension Characteristic with Consideration to Collision of Components 23

3.2.1 Restraint condition of configuration 25

3.2.2 Configuration space 26

3.2.3 Workspace 29

3.3 Investigation of the Motion with Consideration to Deformation of Components 31

3.4 Summary 35

4 Application to an Extendable Arm for Working in a Narrow Space 37
4.1 Mechanism Design and Modeling 37
4.1.1 Improvement for performance maximization as a multiple-DOF extendable mechanism 37
4.1.2 DOF of one segment 40
4.2 Displacement Analysis 41
4.2.1 One segment 41
4.2.2 Multiple segments 44
4.3 Proof of Concept 47
4.3.1 Actuation method 47
4.3.2 Motion experiment 50
4.4 Tapered Extendable Arm with Modified Folding Diagram 53
4.4.1 Modification of the folding diagram 54
4.4.2 Observation of prototypes' behavior 55
4.4.3 Quasi-static analysis 57
4.5 Summary 59

5 Application to an Assistive Devise for Fall Prevention 60
5.1 Specification of the Device 60
5.2 Idea for Implement Rapid Extension and High Load Capacity 63
5.2.1 Difference of velocity ratio of output to input depending on where the mechanism is actuated 63
5.2.2 Suitable inputs set to actuate the distances between longitudinal sides 66
5.2.3 Examples of actuation methods 69
5.3 Experimental Study with the Early Prototype 70
5.3.1 Rapid extension by airbag 70
5.3.2 Relation between impact force and tensile force in lock element 73
5.4 Summary 75

6 Conclusions and Future Work 77
6.1 Conclusions 77

6.2 Future Work 80
6.2.1 Outlook for the future 80
6.2.2 Remaining problems of each application 80

Bibliography **84**

Appendix **92**
A.1 Displacement analysis of Origami Spring 92

List of Tables

3.1 Parameters and contraction/extension limits of each type of Origami Spring 27
3.2 Maximum ranges of θ_2 and θ_3 during extension 29
3.3 Example of two portions A and B of $e_i \neq 0$ 32

4.1 Metrics of the configurations at the workspace boundary 43
4.2 Relation between the inputs condition and extension direction 44
4.3 Range of the length $\|\overrightarrow{U_1U_{10}}\|$ 45
4.4 Relation between the inputs and extension direction 48
4.5 Mass and extension ratio 56

5.1 Result of the simplified fall simulation 61
5.2 Target specifications of the assistive device 63

6.1 Summary of extendable devices 79

List of Figures

1.1 Representative deployable cylindrical origami structures 2
1.2 Summary of two types of deployable origami structures 3
1.3 Motion of Origami Spring by reducing its circumference 4
1.4 Summary of two types of extendable devices 6
1.5 Conceptual design of the extendable arm 7
1.6 Conceptual design of the assitive device for fall prevention (a story board) 9
1.7 Flow of this thesis with features of Origami Spring and inspired mechanism 11

2.1 Folding diagram and unit right-angled triangle 14
2.2 Detail of Origami Spring motion 15
2.3 Planes made by lateral sides between each segment 15
2.4 Extension limit because of collision between paper edges 15
2.5 Two types of hyperboloids consisting of Origami Spring 16
2.6 Wood-stick models of Origami Spring 16
2.7 Examples of Origami Spring with different number of sides of the regular polygon 17
2.8 Folding diagram where some rows are removed 18
2.9 Contracted shapes of rows-removed Origami Spring examples 18
2.10 Difference of full-extended lengths based on the number of rows . . . 18
2.11 Difference of folding diagrams depending on the unit triangle types . 18
2.12 Difference of contracted shapes depending on the unit triangle types . 18
2.13 Difference of extended shapes depending on the unit triangle types . . 19

3.1 Kinematic diagram of elemental mechanism of Origami Spring 21
3.2 Spherical 6R linkage as the kinematic model of Origami Spring 21
3.3 Posture of Origami Spring during extension 21
3.4 Angles between the plane B and the unit triangles 22
3.5 Arranged kinematic diagram of Origami Spring 22
3.6 Independent variables of Origami Spring 23
3.7 Configuration of Origami Spring obtained by displacement analysis . 23
3.8 Simplified unit structure of Origami Spring 24
3.9 Result of displacement analysis when thickness of components and collision among components are ignored 24
3.10 Determination of each point in the spiral shapes composed of the lateral sides of the unit triangle 25
3.11 Restraint condition of the longitudinal sides 26
3.12 Configuration space derived from theoretical analysis 28
3.13 Visualization of ranges of θ_2 and θ_3 based on Table 3.2 29
3.14 Relative position vector $\overrightarrow{R}$ in Origami Spring 30
3.15 Workspace of each type of Origami Spring 30
3.16 Overlapping order and deformation of hypotenuses 31
3.17 Definition of e_i, magnitude of relative deformation of hypotenuses . . 32
3.18 Color maps of stability index E in cross-section $\theta_1 = 47.5$deg 33
3.19 Configuration line derived with consideration to the deformation of hypotenuses 33
3.20 1 DOF motion of Origami Spring along the input line of Fig. 3.19(a) . 34
3.21 Symmetry of spiral shapes of the lateral sides of the unit triangle . . 34
3.22 Comparison of spiral shapes 34

4.1 One segment folding diagram of the 12- and 9-sided mechanisms . . . 38
4.2 Vertical and tilting extension motions achieved by decreasing the number of lateral sides from 12 to 9 39
4.3 Initial prototype of the novel mechanism. The kinematic chain 39
4.4 Kinematic model for the loop closure analysis 40
4.5 Definition of points 42

4.6 Definition of inputs for one segment: θ_4, θ_5, and θ_6 42
4.7 Cross section of the configuration space at $\theta_5 = 25$ deg 42
4.8 Configurations at the boundary of the workspace 43
4.9 Definition of tilt angle ψ and curvature radius ρ 43
4.10 Two inputs in the lower lateral chain 44
4.11 Comparison of possible configurations 45
4.12 Example of the entire configuration of the mechanism with three segments obtained via displacement analysis 47
4.13 Arrangement of four lateral chains for three segments 48
4.14 Design of the base lateral chain 49
4.15 Design of the upper lateral chain 49
4.16 Experimental setup 50
4.17 Extension and contraction 51
4.18 Swinging from right to left and vice versa 51
4.19 Fully extended shape and load trial 52
4.20 Example of an S-shape configuration with inflection points 52
4.21 Generation of maximum tilting configurations 52
4.22 Big head shape during sequential extension 54
4.23 Idea to implement a tapered shape in Origami Spring 55
4.24 Ratio of lower to upper diameters r_D 55
4.25 Modified folding diagram 55
4.26 Design of each prototype 56
4.27 Extension of each prototype 56
4.28 Comparison of maximum tilting configurations to each direction . . . 57
4.29 Kinematic model in GIM® for quasi-static analysis 58
4.30 Target motions for quasi-static analysis 58
4.31 Ratio of F_{Tap} to F_{Cyl} in each piston 58

5.1 Definition of parameters for the simulation 61
5.2 Inverted pendulum models for the simulation 61
5.3 Dimension of the proposed assist device 62

5.4 Change of the distance between each longitudinal side l_i during 1 DOF extension of the zero thickness model 64
5.5 Two inputs l_6 and l_{1-9}, and output point C_U 64
5.6 Velocity ratios of inputs l_6 and l_{1-9} to output during 1 DOF extension of the zero thickness model 65
5.7 Functional requirements in each phase of the storyboard 65
5.8 Unfolded prototype 66
5.9 Kinematic model of the extendable mechanism. The actuators to extend l_i are modelled as a C-C-C kinematic chain and the active joints are shown in red. 66
5.10 Change of the distance between each longitudinal side l_i during 1 DOF extension of the wood-stick model 67
5.11 Velocity ratios of inputs l_6 and l_{1-9} to output during 1 DOF extension of the wood-stick model 67
5.12 Two types of airbags made by PVC 69
5.13 Prototype which has the airbags for extension and the zip ties to hold the extended configuration 70
5.14 Experimental setup for extension 71
5.15 Extension motion by airbags 71
5.16 Example of time change of acceleration $\ddot{\zeta}$ during the extension motion 71
5.17 Example of time change of velocity during the extension motion . . . 71
5.18 Airbag made by polyethylene sheet 72
5.19 Example of time change of force F_z and moment M_y during the extension motion 72
5.20 An idea to improve the extension ratio 73
5.21 Experimental setup for impact force 74
5.22 Example of time changes of the impact and tensile forces 75
5.23 Relation between the impact and tensile forces 75

6.1 Prototype of the extendable mechanism which consists of 3 segments 82
6.2 Extendable mechanisms placed in parallel following the concept in Fig. 1.6 82

A.1 Definition of each point, angle and vector 92
A.2 Definition of ω_i 92

Chapter 1

Introduction

1.1 Background

1.1.1 Deployable origami structures

Origami is the art of paper folding to make a sculpture from a flat square sheet. Typical origami is a sculpture enjoyed by looking at after folded. On the other hand, there are some origamis which can change their shapes after folded by moving a part, and their unique motions are enjoyable. Among them, deployable origami structures have attracted attention recently as base structures of transformable devices for several reasons. Many deployable origamis can change their shapes dramatically from very compact to largely deployed ones. Their shapes and motions can be designed by creating and modifying their folding diagrams. In addition, their shapes can be changed, like a large curvature, by adding external force thanks to the flexibility of components. Based on the features above, numerous types of deployable origami structures have been applied to transformable devices like the deformable wheel [1], the worm robot [2], the solar sail [3] and the extendable manipulators [4–7].

Deployable origami structures are roughly divided into two types: rigid-foldable origami and soft-deployable origami. The former is foldable without any deformation in its components, such as the famous Miura-ori [8]. The structure of rigid-foldable origami is relatively simple, such that there are four facets around one intersection of foldings in many cases, to consist of rigid materials. Specifically, the number of foldings tends to be small, which overlap each other in contracted configuration. In

the rigid-foldable origami, facets were regarded as rigid links and foldings were regarded as revolute joints [9,10]. This means that an origami structure was regarded as a mechanism. In many cases, origami structures can be modelled as spherical linkages and their characteristics were analyzed, for example, degree of freedom (DOF) [11], rigid foldability [12,13], kinematic and geometric compatibility conditions [14]. Several methods have been developed to fold the structure as small as possible with thick panels [10,15,16]. Most rigid-foldable origamis have only a single DOF and their two configurations were mainly focused on; fully contracted and extended ones [17,18]. As other examples, the modular origami robot was developed with a equilateral triangle [19] and the fluid-driven artifical muscles was developed by covering a rigid origami structure with airbag [20].

The latter, soft-deployable origami, is deployable and transformable, such as the examples shown in Fig. 1.1. The structure of soft-deployable origami is relatively complex, such that there are more than six facets around one intersection of foldings, to take various configurations with thin materials. Several types of extendable devices have been developed with thin materials based on such origami structures as the assitive devices for daily living activities [4–7]. However, their deployment and large curvature shapes, which look like a multiple DOF motion, are considered being achieved thanks to their material flexibility, not only to their kinematic structure. In other words, deformation occurs in the foldings and facets [21,22]. Because of the deformation of components, soft-deployable origami cannot be kinematically modelled as a mechanism directly from its structure.

(a) Helix Tower (b) Bellows fold (Yoshimura pattern)

Figure 1.1: Representative deployable cylindrical origami structures. These structures can be extended by pulling them along the longitudinal direction and/or rotating each segment.

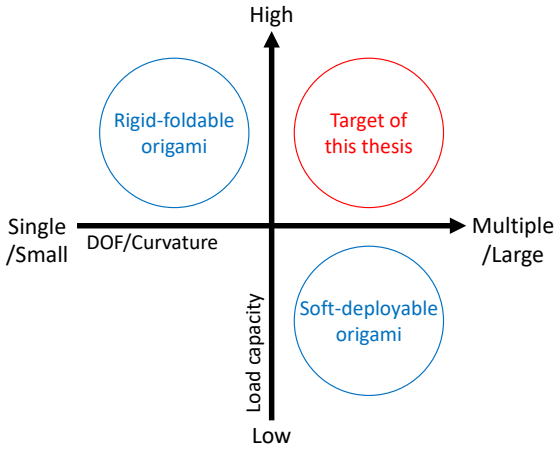

Figure 1.2: Summary of two types of deployable origami structures

Let's summarize the features of two types of deployable origami structures. Rigid-foldable origami tends to have high stiffness thanks to material rigidity, but it has only a single DOF. Soft-deployable origami tends to have multiple DOF thanks to material flexibility, but its load capacity is low. Here, I have come to an idea that novel extendable mechanisms can be obtained by taking the advantages of both types of deployable origami structures as shown in Fig. 1.2. In detail, if a soft-deployable origami structrue, which can be modelled as a multiple DOF mechanism, consists of rigid components without deformation, extendable mechanisms inspired by a deployable origami can have characteristics which are difficult to be implemented at the same time by conventional origami structures, such as compactness, largely bendable, and high load capacity. The problem to realize this idea is how a soft-deployable origami can be modelled as a mechanism with consideration to the deformation of components. The deformation of components occurs due to the collision between each component or the change of the length of foldings during transformation. In the related researches, the deformation of components was introduced in a rigid-foldable origami to consider the misalignment of foldings [23, 24] or to develop a desired soft origami [25]. In addition, the distortion of components when the structure is folded was considered [26]. They considered the deformation of components adding to a rigid-foldable origami or in a soft-deployable origami, and the deformation of components is considered in a mechanism based on a soft-deployable origami in this thesis.

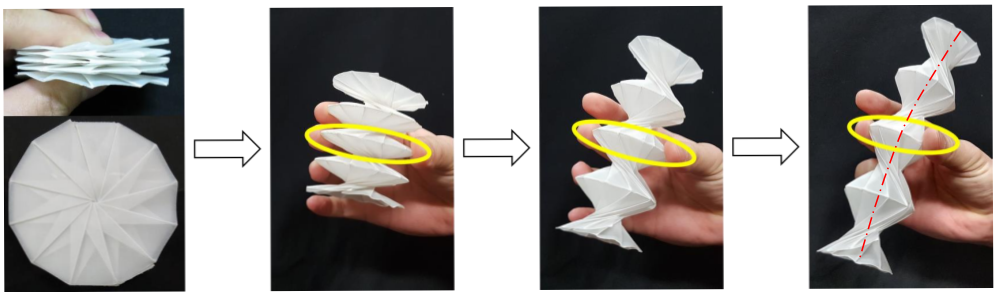

Figure 1.3: Motion of Origami Spring by reducing its circumference

Among soft-deployable origami structures, Origami Spring [27] is selected as the subject of this thesis because of its ease of actuation and multiple DOF. Regarding the actuation, most deployable origami structures need to be pulled along a deployment direction and/or rotated in an axis as shown in Fig. 1.1. Compared to them, Origami Spring can be easily extended by reducing only one circumference as shown in Fig. 1.3 and this is the unique feature. Its relevant applications were discussed and its features of behavior were compared with similar deployable origami structures [28], and it was applied directly with thin materials to a reconfigurable antenna [29] and considered as an option of a worm robot's base structure [2]. However, its kinematic and mechanical characteristics have not been sufficiently revealed. For example, when the deformation is ignored, Origami Spring can be modelled as a 3 DOF mechanism by regarding the foldings as revolute joints and the facets as rigid links based on its folding diagram. However, the motion of Origami Spring looks like a single DOF motion as shown in Fig. 1.3. To apply Origami Spring to extendable mechanisms, the discrepancy between the observed motion and DOF needs to be investigated, which has never been studied. In the structure of Origami Spring, especially near the center of it, collision and deformation of components are observed and these could be a clue to explain the discrepancy. The key idea to reveal the characteristic of Origami Spring is modelling a soft-deployable origami with combination of rigid and compliant components while keeping the mechanism equivalence.

In this thesis, to enable applications of Origami Spring to extendable mechanisms, a model of Origami Spring with a combination of rigid and compliant components is proposed by identifying the components which must deform, and the

characteristics of Origami Spring's extension are revealed with the proposed model. In addition, the effect of deformation on the configuration of Origami Spring is investigated. Based on the above, Origami Spring is applied to extendable mechanisms for two applications expanding its characteristics.

1.1.2 Potential application of a deployable origami to extendable mechanisms

In this thesis, two applications of origami-inspired extendable mechanisms are considered: A) extendable arm to perform some tasks in a narrow space instead of humans in heavy industries manufacturing processes, and B) assistive device for older people to prevent a serious injury with a fall. The reasons why these two applications are considered are mentioned respectively.

As related studies of two applications, there are a lot of products and researches about extendable devices. These extendable devices can be roughly divided into two types: linear extendable device and free-form extendable device. As examples of the former, Spiralift [30] is a compact lifting system and extends by inserting a sheet metal between spiral wide springs. It is used as industrial lifting solutions because of its high load capacity, high precision and high extension ratio. Collins and Yim [31] proposed an extendable arm with the spiral zipper which can extend by connecting the zipper belts each other in the spiral shape. It provides high extension ratio with lightweight. Zip chain actuator [32] and Zippermast [33] are extendable mechanisms which consist of metal zip chains or sheets, and these have also high extension ratio, high rigidity and high speed motion. Linear extendable robot arm [34] and CORO [35] can extend by connecting blocks which are stored in the pole with a sufficient load capacity. These are intended to collaborate with humans. Teshigawara and Asada developed a massive extendable arm with scissor mechanisms for inspection and maintenance of equipment inside buildings [36]. As mentioned above, there are a lot of linear extendable devices and most of them have high load capacity with high extension ratio, and some of them can extend rapidly.

The examples of the latter, free-form extendable devices which can generate curved shapes, include the origami-inspired extendable arms with thin materials

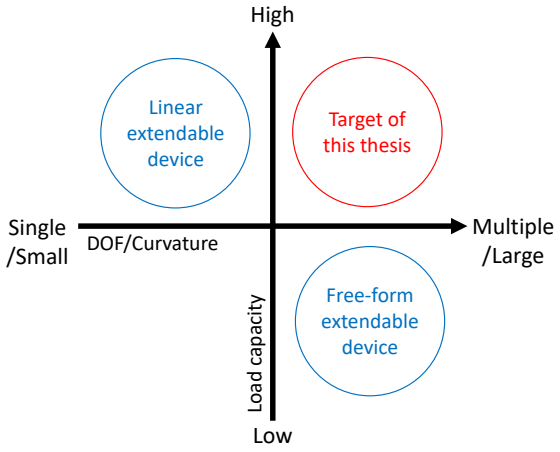

Figure 1.4: Summary of two types of extendable devices

as mentioned above [4–7]. Pneumagami uses three origami-based rigid chains in parallel [37]. As other examples, a deployable truss for space crane arm [38], a parallel mechanism based lightweight deployable binary manipulator for a space robotic mission [39], a triple scissor extender robot arm [40] and an indian-ball based arm [41] were proposed as multiple-DOF extendable arms with rigid components. As pneumatic approaches, the parallel bellows [42], the parallel artificial muscle [43], the pressure driven eversion [44], the fabric actuator [45, 46] were developed. Free-form extendable devices have multiple DOF but their load capacity are not as high as the linear extendable devices.

Let's summarize the features of two types of extendable devices. Linear extendable device tends to have high load capacity, but it has only a single DOF. Free-form extendable device has multiple DOF, but its load capacity is low as shown in Fig. 1.4. Here, Fig. 1.4 corresponds to Fig. 1.2. It can be said that an origami-inspired extendable mechanism which has the advantages of both types of deployable origami structure is also novel in the field of extendable mechanism.

A) Extendable Arm for Working in a Narrow Space

In heavy industries, such as the automobile and aviation industries, a majority of the manufacturing processes is automated. However, a few heavy tasks, such as assembly, inspection, and maintenance, occur in narrow spaces where workers may

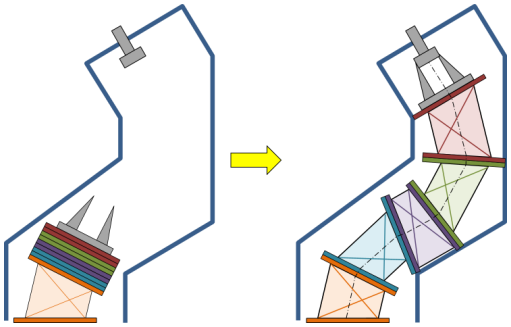

Figure 1.5: Conceptual design of the extendable arm that can bear reaction forces and perform heavy labor by exploiting the contact forces with narrow spaces. This arm is extended from the bottom sequentially for a simple control.

be unable to view the workspace. Such tasks, which were called as "the last one foot problem" [40], have been manually performed by workers and involve inconvenient postures that may lead to injuries.

As a solution to this problem, I propose a concept of an extendable arm that can bear reaction forces and perform heavy tasks by exploiting the contact forces with narrow spaces. This concept is depicted in Fig. 1.5 and this arm is extended from the bottom sequentially for a simple control. To work in a narrow space, the primary requirements of the extendable arm are high extension ratio to reach a far point and large curvature shape to avoid obstacles. In addition, a sufficient load capacity is required when performing such tasks. These requirements correspond to the target in Figs. 1.2 and 1.4, and this is the reason why Origami Spring can be a base structure.

To develop this extendable arm, a practical mechanism which has a potential to satisfy the primary requirements mentioned above is needed, and the usability of such a mechanism needs to be validated. In this thesis, a design of a novel extendable mechanism is introduced where characteristics of inspired origami structures are expanded with consideration to the effect of collision and deformation on the workspace, and the basic motion of the proposed mechanism is verified through displacement analysis and motion experiments, using an actuated prototype.

B) Assistive Devise for Fall Prevention

Aging society is one of the big problems for many countries. In Japan, among the causes of that older people need long-term assistance, fracture/fall is the fourth cause and only an accident [47]. To keep older people' health is an important measure against aging society, and the number of older people who need long-term assistance can be decreased by preventing serious injuries with a fall such as fracture of femur and hip joint with engineering approaches. The major measure is the hip protector to prevent a fracture by a fall. Hip protectors are used with underwear. Their effectiveness was investigated by many researchers [48,49]. As a novel hip protector, Hip'Safe was invented which detects a fall in 200 ms and the airbags inflate in 80 ms at the side of hip joints [50]. There is a similar approach to protect hip by a short skirt shape airbag [51]. Hip protectors are effective in the reduction of force applying to hip at the instance of contact with the ground. However, fall postures include the cases in which knee contacts with the ground first [52].

To prevent a fracture by a fall, it is better to consider the force which is applied to bones through the first contact part with the ground. Therefore, other solutions are needed and two approaches can be considered: dynamic assistance to keep or recover the user's balance, and supporting the user's body before no parts of the body contact with the ground except feet. Regarding the former solution, there were some researches which use tail-inspired devices to keep human balance [53,54]. As for the latter solution, some wearable devices to support humans' weight can be referred, for examples, supernumerary robotic limbs [55] and wearable chairs [56,57].

Here, I propose a concept of an assistive device for fall prevention by supporting the user's body before no parts of the body contact with the ground as shown in Fig. 1.6. The structure of the proposed device is inspired by a crinoline which is a structure to hold out a woman's skirt around the mid-19th century. The proposed device is a tensegrity structure where extendable mechanisms are connected by elastic materials, which are the blue lines in Fig. 1.6, to support heavy load as a compressive force in the extendable mechanisms and a tensile force in the elastic materials. With consideration to that a fall happens when older people are walking regardless of inside or outside, extendable mechanism needs to extend rapidly and

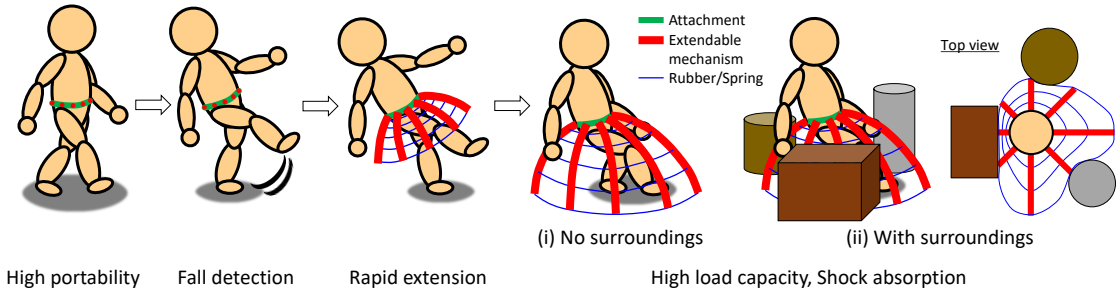

Figure 1.6: Conceptual design of the assitive device for fall prevention and functional requirements in each phase (a storyboard). Compactness of this device does not interfere with user's daily activity. When the user is going to fall down, the device extends rapidly and supports user's body with a tensegrity structure where extendable mechanisms are connected by elastic materials.

stop its extension when it contacts with surroundings. The target users are older people who can walk by themselves in healthy walking speed [58], then the proposed device should not interfere with user's daily activity when it is contracted. The functional requirements of the proposed device are rapid extension, high load capacity, high shock absorption, high portability, and rapid fall detection. Among related studies which are introduced above, some extendable devices have rapid extension and high load capacity as their features at the same time, but they are definitely not supposed to be carried and attached to human body. It is considered that whether rapid extension and high load capacity can be implemented or not depends on the base mechanism. After a feasibility study of these two requirements, shock absorption could be implemented while improving portability. Fall detection could be developed apart from other requirements.

In this thesis, as a first step to develop the proposed device, feasibility to implement rapid extension and high load capacity is studied experimentally with an extendable mechanism inspired by a structure which has the potential to achieve high portability: lightweight and small volume with high extension ratio. Deployable origami structure is considered as an option which has the potential. Among them, Origami Spring is selected as the base structure because its whole structure can be extended by actuated only one part (Fig. 1.3) and its configuration can be kept easily. These features are investigated from a perspective of the velocity ratio of output to input.

1.2 Objective and Contribution of the Thesis

Deployable origami structures have been applied to a lot of transformable devices recently. In many cases, the original origami structures were directly used with flexible materials to keep their high transformability. On the other hand, some origami structures were regarded as 1 DOF mechanisms with rigid materials and their structures tend to be simpler.

The key idea of this thesis is that novel extendable mechanisms can be obtained by applying a kinematic perspective, which was applied to simple deployable origami structures, to a complex deployable origami structure with consideration to collision and deformation of components. With this idea, extendable mechanisms inspired by a deployable origami can have characteristics which are difficult to be implemented at the same time by conventional origami structures. Among soft-deployable origami structures, Origami Spring is selected as the subject of this thesis because of its unique features as shown in Fig. 1.7, for example, its motion looks like a single DOF motion but it can be modelled as a 3 DOF mechanism when the deformation of components is ignored.

The objective of this research is that Kineto-elasto-static characterization of a deployable origami with consideration to collision and deformation of components and to enable to design an extendable mechanism inspired by a deployable origami beyond the limit of a conventional deployable origami. The objectives of each chapter are following:

2. Identify the components which must deform in the structure of Origami Spring and get a clue to model Origami Spring

3. Reveal the characteristics of Origami Spring's extension with a kinematic model where the collision and deformation of components are considered

4. Design an extendable arm while maximizing the performance of the extendable mechanisms and verify the basic motion of the designed extendable arm

5. Verify the feasibility of an idea experimentally to develop an assistive device for older people to prevent a fall

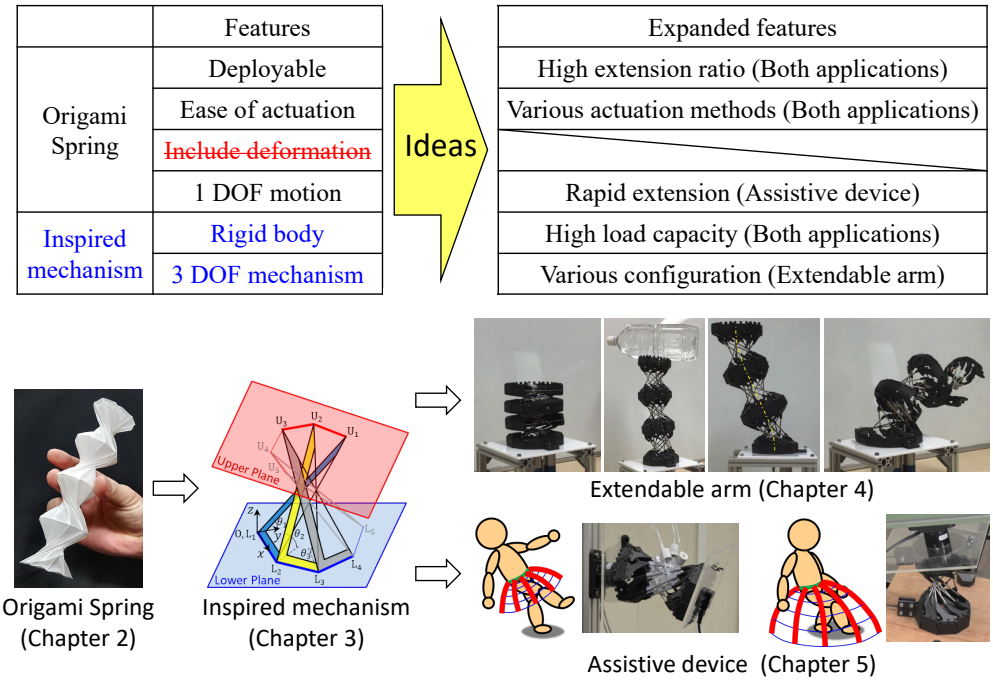

Figure 1.7: Flow of this thesis with features of Origami Spring and inspired mechanism. Functional requirements of two applications are implemented by expanding and beyond their features.

The flow of this thesis is summarized in Fig. 1.7 and the ideas and main contents in each chapter are as follows.

In chapter 2, to identify the components which must deform in the structure of Origami Spring, its structure is simplified and the physical models of Origami Spring are fabricated with rigid and compliant components. Based on the observation of the models' motions, the clue to model Origami Spring as a mechanism is obtained.

In chapter 3, to enable applications of Origami Spring to extendable mechanisms, a kinematic model of Origami Spring with a combination of rigid and compliant components is proposed based on chapter 2 and the characteristics of Origami Spring's extension are revealed with the proposed model considering the collision between rigid components. In addition, the effect of compliant components' deformation on the configuration of Origami Spring is investigated. By regarding Origami Spring as a mechanism, its features are expanded as shown in Fig. 1.7.

In chapter 4, to maximize the performance of an extendable mechanism inspired by Origami Spring beyond that of the original origami structure, the deformation of

components is removed and the collision between components is reduced, which give a large effect to constrain its motion. Through these improvements, the extendable arm is designed and its basic motion, such as vertical extension and generation of various configuration including a large curvature configuration, is verified through the displacement analysis and motion experiment.

In chapter 5, the actuation strategy of the extendable mechanism inspired by Origami Spring to achieve rapid extension and high load capacity in one mechanism is proposed focusing on the difference of the velocity ratio of output to input depending on where the mechanism is actuated. Through the experimental studies with a prototype, the feasibility of this strategy is verified experimentally.

The contribution of this research is that characterization of a deployable origami which includes collision and deformation of components in its structure is enabled by modelling it with combination of rigid and compliant components, and analyzing the model kinematically. In addition, it is enabled that the design strategies of novel extendable mechanisms are proposed which are beyond the limit of conventional deployable origami structures and the features of the original origami structure by applying a kinematic perspective with consideration to collision and deformation of components.

1.3 Thesis Overview

This thesis focuses on kinematic modelling and analysis of a deployable origami structure, and proposes two extendable mechanisms with different functional requirements. The subject of this thesis: Origami Spring is introduced with its features and structure. Modeling and displacement analysis of Origami Spring is carried out considering collision and deformation of components. A design of a novel mutliple-DOF extendable arm with rigid components inspired by Origami Spring is proposed, which can generate a large curvature configuration and provide a sufficient load capacity. A feasibility study of extendable mechanism inspired by Origami Spring is demonstrated experimentally while focusing on the implementation of rapid extension and high load capacity. The conclusions and future work are summarized.

Chapter 2

Origami Spring

In this chapter, basic information and the features of Origami Spring are introduced. In detail, firstly, the folding diagram of Origami Spring is shown with the parameter definition. Secondly, the feature of Origami Spring's motion and structure are explained with paper and wood-stick models. Lastly, several ways to modify the folding diagram are introduced to change the shape and motion of Origami Spring.

2.1 Folding Diagram

As mentioned in chapter 1, Origami Spring is an extendable cylindrical origami invented by Jeff Beynon.

A folding diagram of Origami Spring consists of right-angled triangles, an example is shown in Fig. 2.1. In this thesis, the right-angled triangle is called as the unit triangle, and sides of the unit triangle are called as longitudinal side, lateral side and hypotenuse respectively. Each length in a folding diagram is defined as shown in Fig. 2.1, where a is the length of the longitudinal side, b is the length of the lateral side, m is the number of segments, the example in Fig. 2.1 consists of four segments, and n is the number of sides of the regular polygon when Origami Spring is fully contracted. $\varphi = \pi/n$ is the smallest angle of the unit right-angled triangle. $A = ma$ and $B = nb$ are the lengths of sides of a paper. The original Origami Spring was made with $n = 12$ and this is used as the base structure in this thesis. The reason is explained in section 2.3.

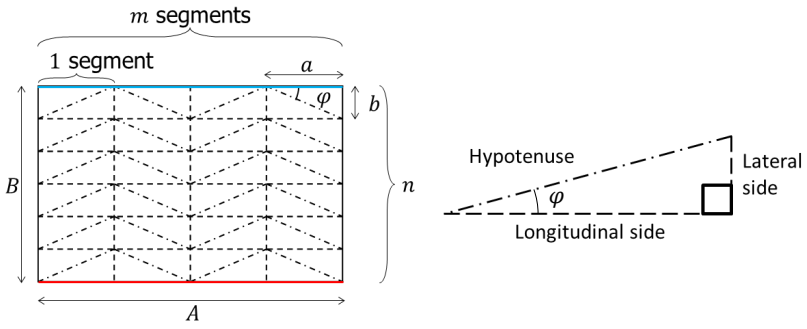

Figure 2.1: Folding diagram and unit right-angled triangle

2.2 Motion and Structure

The whole structure of Origami Spring can be extended by reducing one circumference and its shape changes from flat to cylindrical as shown in Fig. 1.3. Its motion looks like a single DOF one and its whole shape is curved with extension. What the unique behavior of Origami Spring is that one of the paper edges of the folding diagram coils into the inside of the other edge alternately while keeping a mountain folded shape as shown in Fig. 2.2. This coiling motion makes the lateral sides of the unit triangle be in a plane between each segment as shown in Fig. 2.3. There are extension and contraction limitations, as shown in Fig 2.4, because of collision between paper edges although the contraction limitation is hard to be observed because of flexibility of paper. The edges of paper, red and blue lines in Figs. 2.2 and 2.4, always contact each other during extension and contraction motion.

In the configuration of Origami Spring, especially near the center, collision and deformation of paper are observed. The structure of Origami Spring can be simplified as a combination of two hyperboloids as shown in Fig. 2.5. The green line corresponds to the longitudinal side of the unit triangle, and the orange one corresponds to the hypotenuse of that. One is composed of longitudinal sides and the other is composed of hypotenuses. The longitudinal sides do not always collide but hypotenuses intersect at the center of the hyperboloid and this condition is remained consistent during extension and contraction as shown in Fig. 2.5(d). Following this, hypotenuses of the unit triangle must deform due to its thickness.

Looking ahead to apply Origami Spring to a rigid mechanism, two wood-stick

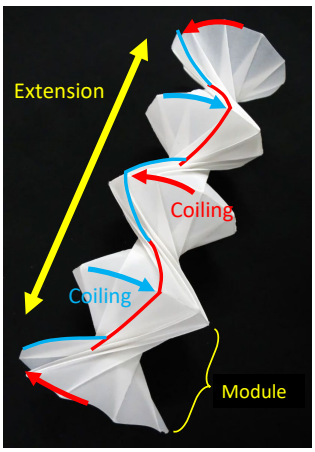

Figure 2.2: Detail of Origami Spring motion. One of the paper edges of the folding diagram coils into the inside of the other edges alternately.

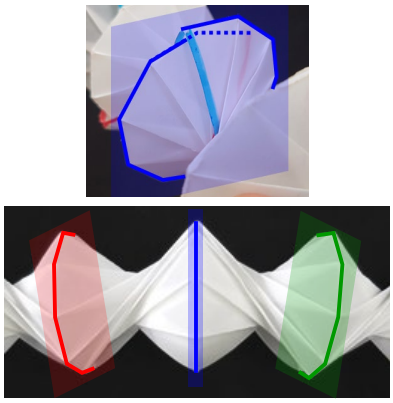

Figure 2.3: Planes made by lateral sides between each segment

Figure 2.4: Extension limit because of collision between paper edges

models, the one and four segments model, were made to observe their motion as shown in Fig 2.6. In both of the wood-stick models, the longitudinal and lateral sides of the unit triangle were replaced by wood sticks. The colored wood sticks correspond to the colored edges in the folding diagram. The hypotenuses were replaced by strings in the one segment model, and removed in the four segments model because the hypotenuses must deform due to their thickness as mentioned above. These wood-stick models behaves similarly to the paper model with extension and contraction functionality as shown in Fig. 2.6. These models showed a clear sign of the contraction limit compared to the paper model. Based on these models, the kinematic model of Origami Spring is proposed in the next chapter.

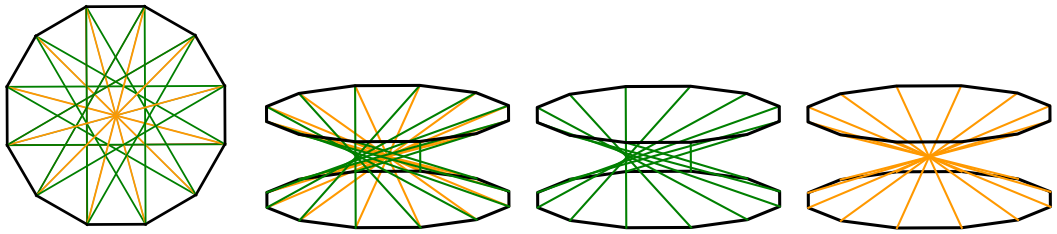

(a) Top view (b) Bird view (c) Longitudinal side (d) Hypotenuse

Figure 2.5: Two types of hyperboloids consisting of Origami Spring

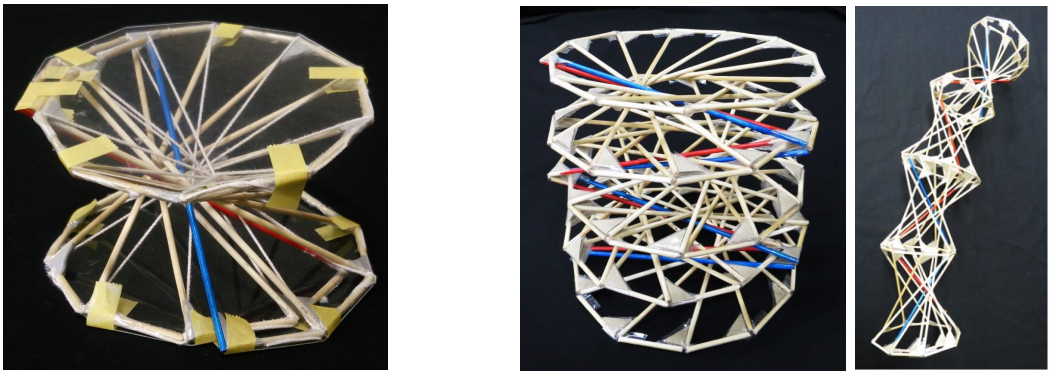

(a) One segment (b) Four segment

Figure 2.6: Wood-stick models of Origami Spring

2.3 Modification of Folding Diagram

In this section, three ways to modify the folding diagram of Origami Spring were tried and their effects on the motion and shape of Origami Spring were observed to apply these modifications to design of extendable mechanisms.

The first way for modification is the change of the number of sides of the regular polygon n. n can be any positive integer, as some examples, Origami Spring with $n = 6, 9, 12, 16$ are shown in Fig. 2.7. When n becomes smaller, the difference of two distances between the center and a side/vertex of the regular polygon becomes larger so that it is difficult for a vertex to coil into inside of a side and the coiling motion is not smooth. When n becomes larger, more papers pile up near the center of the structure so that it is hard to be folded and reach a flat shape when contracted. For the reasons above, Origami Spring with $n = 12$ was used as the base structure in this thesis unless otherwise noted, as mentioned in section 2.1.

(a) $n = 6$ (b) $n = 9$

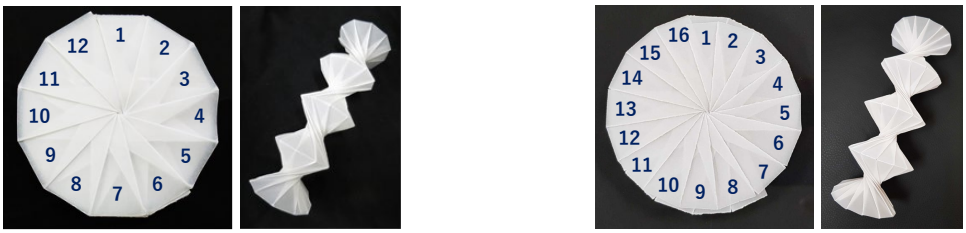

(c) $n = 12$ (d) $n = 16$

Figure 2.7: Examples of Origami Spring with different number of sides of the regular polygon

The second way for modification is the change of the number of rows while keeping the dimensions of the unit triangle φ, a and b as the same. By removing some rows from the folding diagram as shown in Fig. 2.8, the contracted shape becomes such as shown is Fig. 2.9. The less rows are in the folding diagram, the less collisions happen in the structure and its extension limit is expanded as shown in Fig. 2.10. This modification is applied in section 4.1.

The third way for modification is the change of the unit triangle types. In the original folding diagram, the unit triangle is a right-angled triangle. Generally, there are three types of triangle: right-angled triangle, acute-angled triangle, obtuse-angled triangle. When the type of unit triangle is changed, the folding diagrams, the contracted and extended shapes are changed as shown in Figs. 2.11, 2.12, and 2.13. In the case of acute-angled triangle, it can not be folded because foldings need to go through each other. In the case of obtuse-angled triangle, it can be folded and has a hole around the center of the structure while decreasing collisions between hypotenuses. As a special folding diagram, a combination of acute-angled and obtuse-angled triangle can be used. The shape of the folding diagram becomes a fan shape and folded Origami Spring shape becomes tapered shape as shown in

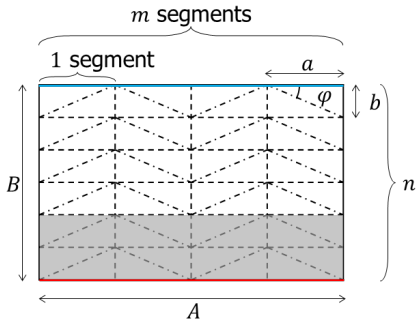

Figure 2.8: Folding diagram where some rows are removed

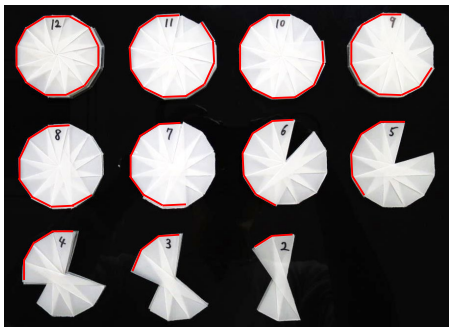

Figure 2.9: Contracted shapes of rows-removed Origami Spring examples

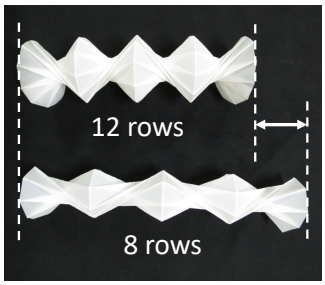

Figure 2.10: Difference of full-extended lengths based on the number of rows

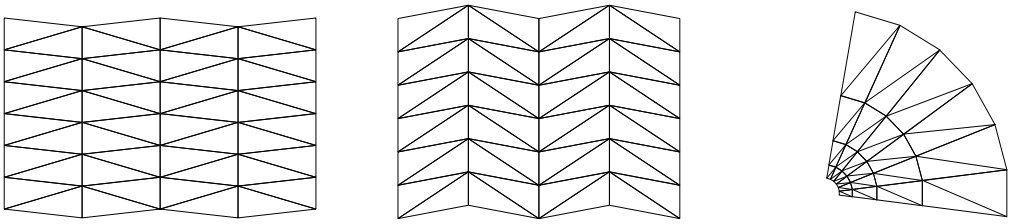

(a) Acute triangle (b) Obtuse triangle (c) Combination

Figure 2.11: Difference of folding diagrams depending on the unit triangle types

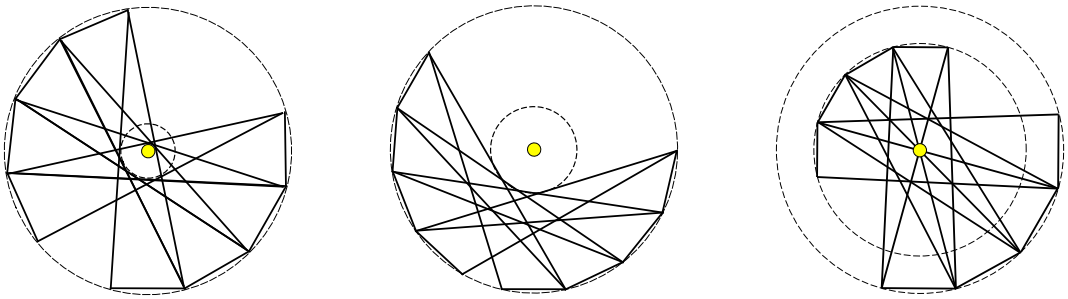

(a) Acute triangle (b) Obtuse triangle (c) Combination

Figure 2.12: Difference of contracted shapes depending on the unit triangle types

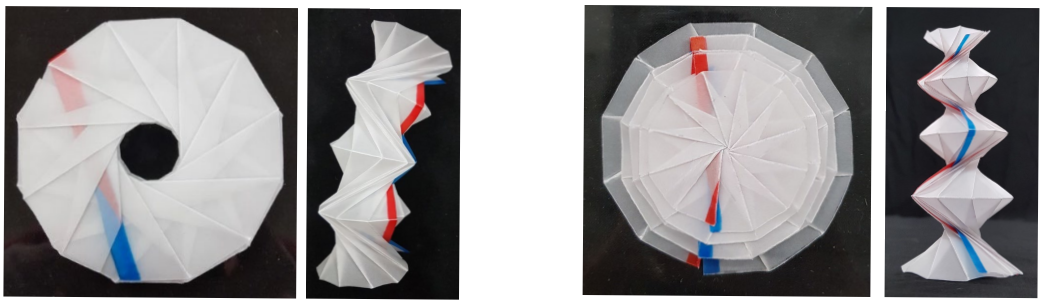

(a) Obtuse triangle (b) Combination

Figure 2.13: Difference of extended shapes depending on the unit triangle types

Figs. 2.11(c) and 2.13(b). This modification is applied and the details is explained in section 4.4.

2.4 Summary

In this chapter, basic definition and features of Origami Spring were introduced.

1. Origami spring can be extended by reducing its circumference and its motion looks like a straight motion with a single degree of freedom. During extension motion, one of the paper edges of the folding diagram coils into the inside of the other edge alternately.

2. It is identified that the hypotenuse must deform due to the collision between others, and two wood-stick models were fabricated where rigid and compliant components were used. They behaved similarly to the paper model with extension and contraction functionality.

3. Three ways to modify the folding diagram were introduced to change the shape and motion of Origami Spring: change of the number of sides of the regular polygon, change of the number of rows while keeping the dimension of the unit triangle, change of the unit triangle type, these effects are investigated in the following chapters.

Chapter 3

Characterization with Consideration to Collision and Deformation of Components

In this chapter, Origami Spring is modeled as a link mechanism which is composed of rigid and compliant components, and kinematic analysis is carried out while taking into consideration the collision and deformation of components. In detail, restraint conditions are determined for displacement analysis based on the situation of the real origami. The configuration space of the kinematic model is extracted which satisfies the restraint conditions with consideration to collision of components. In the configuration space, the effect of components' deformation to configuration of Origami Spring is investigated and the discrepancy between the observed motion and DOF of Origami Spring is clarified.

3.1 Degrees of Freedom and Kinematic Model

To consider the DOF of Origami Spring, six unit triangles were derived from the folding diagram of Origami Spring, as shown in Fig. 2.1, around an intersection point of foldings (red point in Fig. 3.1). In a folding diagram of an origami, foldings can be regarded as revolute joints and facets can be regarded as rigid links based on methods to model an origami with rigid panels [9, 10]. Following these methods,

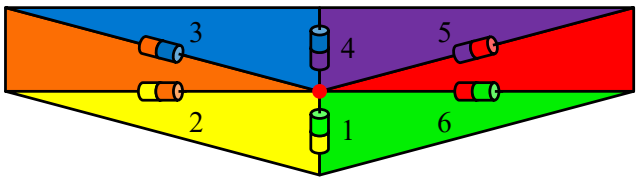

Figure 3.1: Kinematic diagram of elemental mechanism of Origami Spring derived from its folding diagram around an intersection point

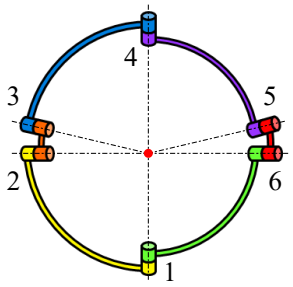

Figure 3.2: Spherical 6R linkage as the kinematic model of Origami Spring

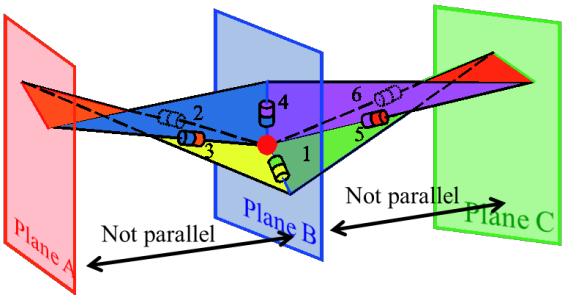

Figure 3.3: Posture of Origami Spring during extension

six unit triangles can be modelled as shown in Fig. 3.1 and it was determined as the elemental mechanism of Origami Spring. The elemental mechanism is a spherical 6R linkage with three DOF because axes of all revolute joints intersect at a point as shown in Figs. 3.1 and 3.2. When the elemental mechanism is folded following the folding diagram and reflecting the geometric restraint that the lateral sides of the unit triangle are in a plane between each segment as mentioned in section 2.2, its configuration becomes symmetric with respect to the plane as shown in Fig. 3.3. This condition can be extended to the whole structure of Origami Spring and each segment becomes symmetric with respect to planes so that only one segment was focused on. In Fig. 3.4, one segment between planes A and B is taken out from Fig. 3.3 and rotated by 90 degree. Figure 3.4 includes not only the unit triangles in Figs. 3.1 and 3.3 but also other unit triangles in the same segment. The angles between the plane B and the unit triangles are denoted as θ_i $(i = 1, 2, \ldots, n, n = 12)$. For a given set of θ_1, θ_2 and θ_3 $(\theta_1 \geq \theta_2 \geq \theta_3)$, positions of the vertices of the unit triangles P_1, P_2 and P_3 are determined and the plane A is determined by three points. Based on the condition where the lateral sides of the unit triangles should be placed in each plane A and B, the postures of other unit triangles are

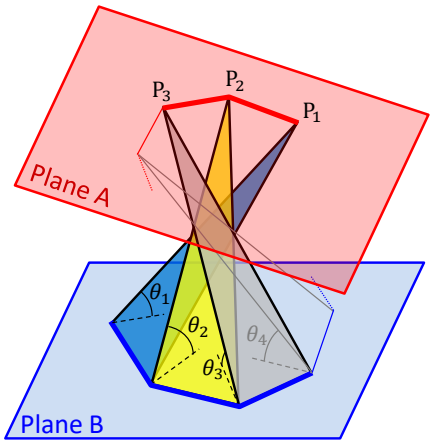

Figure 3.4: Angles between the plane B and the unit triangles

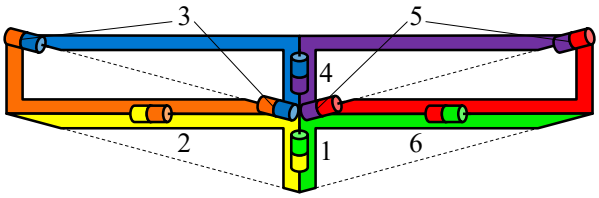

Figure 3.5: Arranged kinematic diagram of Origami Spring

simultaneously determined. Therefore, one segment of Origami Spring has 3 DOF and Origami Spring which consists of multiple segments has also 3 DOF because of the configuration symmetry as mentioned above. However, this DOF does not correspond to the behavior of Origami Spring which is observed like a single DOF. As an idea to investigate this gap between the real behavior and DOF, collision and deformation of components were taken into consideration.

As mentioned in section 2.2, collision and deformation of components are observed in the real Origami Spring, especially hypotenuses of the unit triangles are always deformed to avoid interfering with each other. To reflect the deformation into the kinematic model, the spherical 6R linkage was arranged as shown in Fig. 3.5 while keeping its kinematic equivalence to the elemental mechanism. The revolute joints on the hypotenuses in Fig. 3.1 were moved to the end points of the longitudinal and lateral sides, and the facet links were shaped which do not include hypotenuse. The longitudinal and lateral sides were regarded as rigid links and the hypotenuse were regarded as a compliant component which is depicted with a broken line in Fig. 3.5 [25]. To experimentally confirm that this arrangement does not affect the characteristic of Origami Spring's behavior, the behaviors of the wood-stick models (Fig. 2.6) were observed. As mentioned in section 2.2, wood-stick models behaved similarly to the paper model functionality.

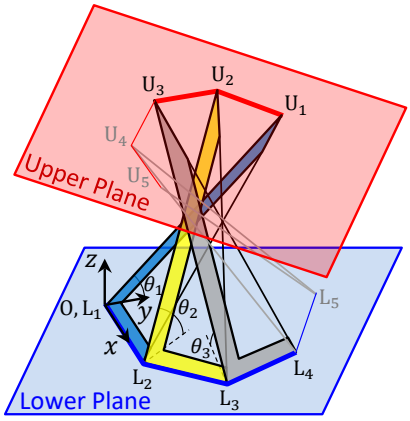

Figure 3.6: Independent variables of Origami Spring

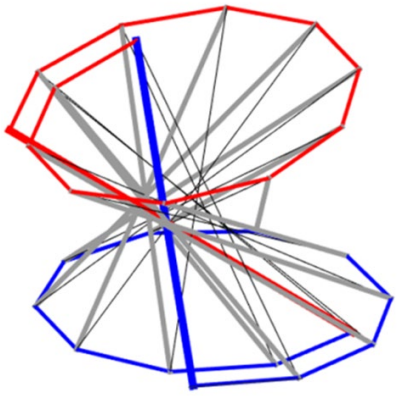

Figure 3.7: Configuration of Origami Spring obtained by displacement analysis

Finally, the kinematic model of Origami Spring is determined as shown in Fig. 3.6. The first three angles θ_1, θ_2 and θ_3 between the lower plane and the unit triangles are determined as variables. The points in the lower plane are denoted as L_i, the points in the upper plane as U_i $(i = 1, 2, \ldots, n+1; n = 12)$. As for the coordinate axes, the origin is located at L_1, the x axis is placed along $\overrightarrow{\mathrm{L_1L_2}}$. With this kinematic model, the configuration of Origami Spring can be determined by displacement analysis (Appx.), as shown in Fig. 3.7. In Fig. 3.7, the red and blue thick lines are the longitudinal sides which correspond to the edges of the paper, and gray lines are other longitudinal sides. Black lines are hypotenuses but they do not reflect the deformation in the real Origami Spring and just connect the edge of longitudinal and lateral sides.

3.2 Extension Characteristic with Consideration to Collision of Components

In this section, as the first step to investigate the motion of Origami Spring, collision of rigid components in the kinematic model was considered. Firstly, the restraint conditions of configuration for a displacement analysis based on the observation of the paper and wood-stick models were set. Secondly, the configuration space with θ_1, θ_2 and θ_3 was derived where the restraint conditions of configura-

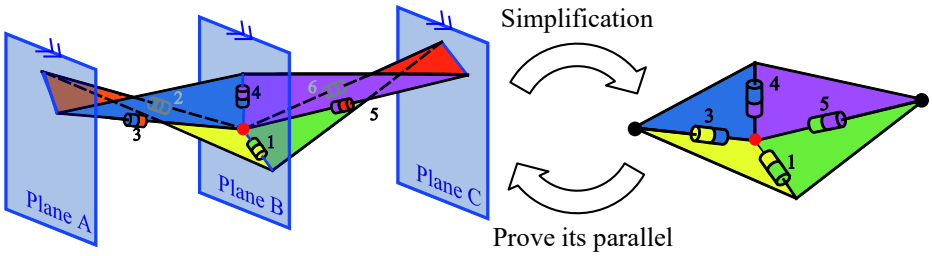

Figure 3.8: Simplified unit structure of Origami Spring

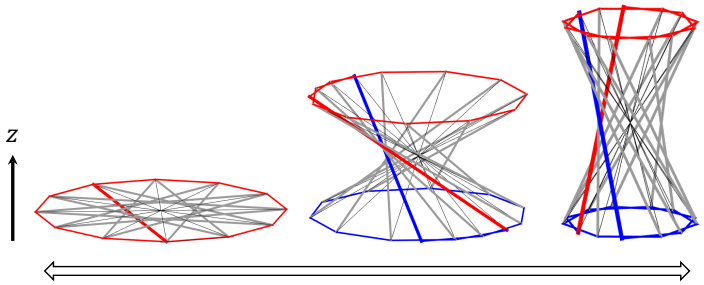

Figure 3.9: Result of displacement analysis when thickness of components and collision among components are ignored

tion were satisfied. Finally, the workspace of Origami Spring based on the derived configuration space was checked and the extension characteristic was discussed.

As a reference, a displacement analysis was done in the case where collision of components was ignored. In this case, the hypotenuses intersect each other at exactly a point without collision and deformation as shown in Fig. 2.5(d) and three variables become $\theta_1 = \theta_2 = \theta_3$. When $\theta_1 = \theta_2 = \theta_3$, the planes between each segment are parallel, and 2^{nd} and 6^{th} revolute joints do not move. Therefore, the spherical 6R linkage can be simplified as a spherical 4R linkage (1 DOF) as shown in Fig. 3.8. In this condition, the black points in Fig. 3.8 move perpendicularly to the planes and the planes become parallel. Figure 3.9 shows the result of displacement analysis when collision of components is ignored. The motion is along z axis which was defined in Fig. 3.6 while the orientation is kept horizontal and this does not correspond to the real motion of Origami Spring where its shape is curved with extension.

3.2.1 Restraint condition of configuration

The observation of paper and wood-stick models revealed that the configuration of Origami Spring needs to satisfy two restraint conditions. The first condition is that the lateral sides of the unit triangle should not interfere with each other and its shape should be a spiral shape as shown in Fig. 3.10. The second condition is that the longitudinal sides of the unit triangle should overlap with each other in a certain order and do not interfere with each other as shown in Fig. 3.11. These two conditions are sufficient conditions where configurations of displacement analysis follow the real configuration, and these two conditions were formulated as follows.

As for the first condition, each coordinate of the points on the lower plane should satisfy the following Eqs. (3.1), (3.2) and (3.3) to avoid collisions. The region with Eq. (3.3) is shown as filled area in Fig. 3.10(a).

$$y_{\mathrm{L}_i} \geq y_{\mathrm{L}_1} \tag{3.1}$$

$$x_{\mathrm{L}_{n+1}} \geq x_{\mathrm{L}_1} \tag{3.2}$$

$$\begin{aligned}(x_{\mathrm{L}_{i+1}} - x_{\mathrm{L}_i})(y_{\mathrm{L}_{n+1}} - y_{\mathrm{L}_i}) > (y_{\mathrm{L}_{i+1}} - y_{\mathrm{L}_i})(x_{\mathrm{L}_{n+1}} - x_{\mathrm{L}_i}) \\ s.t. \|\overrightarrow{\mathrm{L}_1\mathrm{L}_i}\| \geq b\end{aligned} \tag{3.3}$$

Following the lower plane, these conditions are also applied to the upper plane. Then, the local coordinate axes are determined as shown in Fig. 3.10(b) and Eqs.

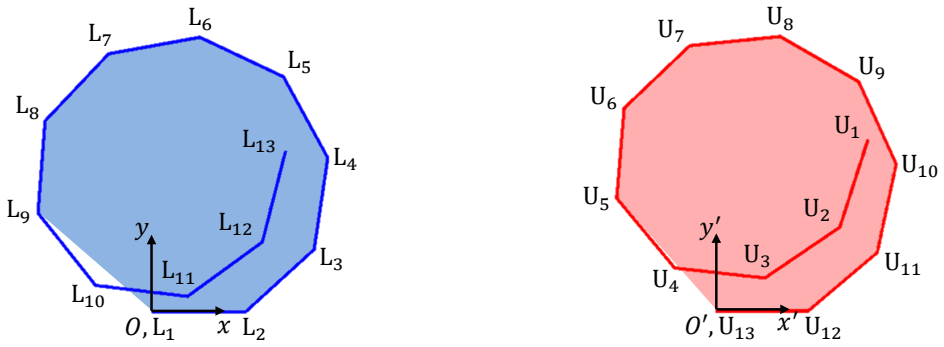

(a) Lower plane

(b) Upper plane

Figure 3.10: Determination of each point in the spiral shape composed of the lateral sides of the unit triangle. As an example, the spiral shapes at $(\theta_1, \theta_2, \theta_3) = (47.5, 43.0, 38.0)$ [deg] are shown.

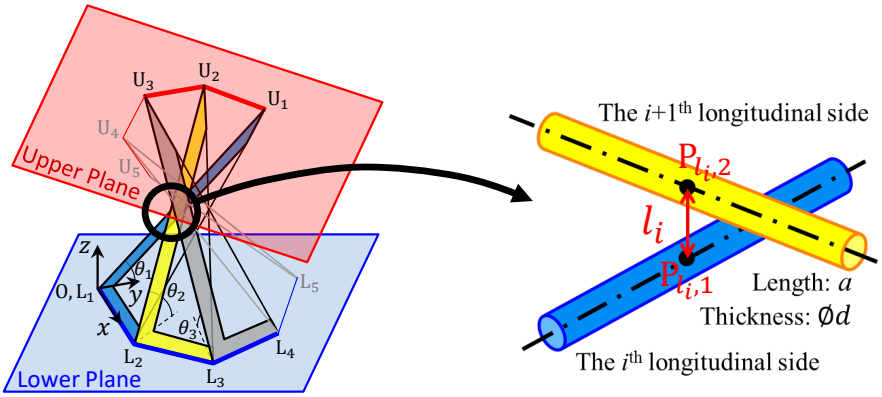

Figure 3.11: Restraint condition of the longitudinal sides

(3.1), (3.2) and (3.3) described with the local coordinate should be satisfied.

As for the second condition, all 13 longitudinal sides should overlap with each other in the order that the $i+1^{th}$ longitudinal side is above the i^{th} longitudinal side ($i = 1, 2, \ldots, n+1$ and when $i = n+1$, $i+1 = 1$), as illustrated in Fig. 3.11. Therefore, the distance between i^{th} and $i+1^{th}$ longitudinal sides notated as l_i should be compared with the thickness of component d and they should satisfy Eq. (3.4). The threshold of numerical comparison l_i and d was set $d \times 10^{-4}$. In addition to this, the order of overlapping is verified with comparison of z coordinates of $\mathrm{P}_{l_i,1}$ and $\mathrm{P}_{l_i,2}$ as shown in Eq. (3.5) which are intersection points of the normal line and longitudinal sides.

$$l_i \geq d \tag{3.4}$$

$$z_{\mathrm{P}_{l_i,1}} < z_{\mathrm{P}_{l_i,2}} \tag{3.5}$$

When Eqs. (3.4) and (3.5) are satisfied with all pairs of longitudinal sides, the second condition is satisfied.

3.2.2 Configuration space

In this thesis, the set of values of the angles θ_1, θ_2 and θ_3 where the output configurations satisfy both of the restraint conditions was defined as configuration space. To derive the configuration space described with θ_1, θ_2 and θ_3, brute-force

search was applied while changing the variable values θ_1, θ_2 and θ_3 and checking if the output configurations satisfy the restraint conditions or not.

A non-dimensional parameter d/a was determined to normalize the thickness of the component d to the length of longitudinal side a because it has a significant influence on the behavior. The configuration spaces of three sets of parameters which represent paper model, wood-stick model and zero thickness model were derived by brute-force search and the results were compared to the experimental results. As for the thickness of the component d of the paper model, the paper thickness is 0.15 mm and it was assumed that the foldings have twice thickness of paper. The increments of each variables were 0.1 deg , while the increments of θ_2 and θ_3 were 0.01 deg for the wood-stick model. The contraction and extension limits were determined as the minimum and maximum values of θ_1. The obtained configuration space is summarized as shown in Table 3.1. Each configuration space is plotted in Fig. 3.12, and the difference of cross-section at a certain θ_1 according to d/a is shown in Fig. 3.12(d) . The color corresponds to each figure of the configuration space in Figs 3.12(a)-(c).

The extension limits obtained by theoretical analysis and the experiment almost match. The difference of the contraction limit between the analysis and the experiment is 12 deg, and one of the factors might be due to the deformation of the wood stick. The contraction limit is more affected than the extension limit by parameter d/a. The influence of parameter d/a can be explained by considering the collisions between longitudinal sides. During extension, there is almost no internal collision occurring, on the other hand, during contraction almost all longitudinal sides collide

Table 3.1: Parameters and contraction/extension limits of each type of Origami Spring

	Type	a [mm]	d [mm]	d/a	Contraction limit (θ_1) [deg]	Extension limit (θ_1) [deg]
Analysis	Zero thickness	10^3	10^{-9}	10^{-12}	2.8	59.4
	Paper	65.3	0.15×2	4.59×10^{-3}	15.1	59.2
	Wood-stick	140	2.5	1.79×10^{-2}	39.0	55.3
Experiment	Paper	65.3	0.15×2	4.59×10^{-3}	-	57
	Wood-stick	140	2.5	1.79×10^{-2}	27	55

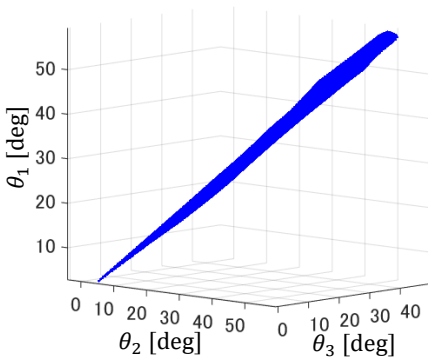

(a) Zero thickness

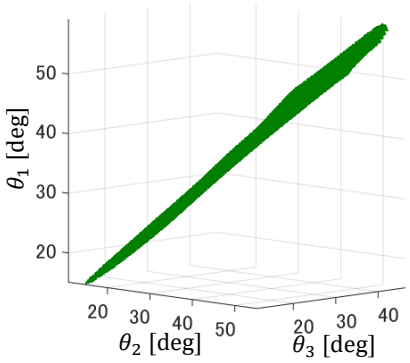

(b) Paper

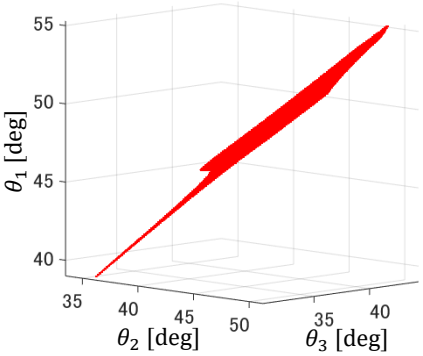

(c) Wood-stick

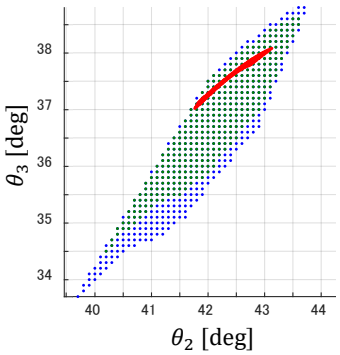

(d) Cross-section of θ_2 and θ_3 at $\theta_1 = 47.5$deg

Figure 3.12: Configuration space derived from theoretical analysis

with each other. As a result, range of motion decreases as the value of parameter d/a increases. Therefore, if the wide range of motion is needed with thick components, an idea to decrease the collision of longitudinal sides is required.

Based on the configuration space, it is confirmed that Origami Spring can extend without deformation of components except the hypotenuse. To clarify the dominant variable, the maximum allowable ranges of θ_2 and θ_3 with respect to θ_1 through all range of θ_1 are obtained and shown in Table 3.2 and Fig. 3.13. In Fig. 3.13, the three unit triangles are aligned with lateral sides in order to visualize range of fluctuation. When θ_1 is a certain angle, θ_2 and θ_3 can be in around 1.2 to 5.3 deg. Following this, it is known that the configuration of Origami Spring is almost determined with one variable, and the other two variables contribute to avoiding the collision between components in a small range. Now, let's look back the result when the collision of components was ignored. In that case, the vertical extension was generated by the spherical 4R linkage. Considering that motion, it can be assumed that the spherical

Table 3.2: Maximum ranges of θ_2 and θ_3 during extension

	Max range of θ_2 with respect to θ_1 [deg]	Max range of θ_3 with respect to θ_1 [deg]
Zero thickness	4.1	5.3
Paper	3.5	4.3
Wood-stick	1.37	1.15

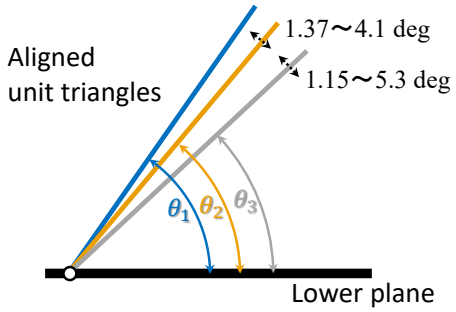

Figure 3.13: Visualization of ranges of θ_2 and θ_3 based on Table 3.2

4R linkage included in the spherical 6R linkage generates rough extension motion and the other revolute joints contribute to avoiding the collision of components.

3.2.3 Workspace

In a configuration of Origami Spring, the components are coiled inside with extension and the shape of lateral sides in a plane changes. By this fact, it is difficult to describe the motion of Origami Spring clearly with a relative motion between certain links. Then, the relative position vector $\overrightarrow{R}$ is defined to describe the workspace of Origami Spring as shown in Fig. 3.14. In Fig. 3.14, spiral shapes of the lateral sides in the lower and upper planes are plotted with blue and red lines. The light blue line connects the center of the circumcircle of the lower spiral shape and the upper one. The side view is defined as shown in Fig. 3.14(b) so that the upper spiral shape can be seen as a line. In this view, ξ axis is the horizontal direction and ζ axis is the vertical direction. The origin of relative coordinates is located at the middle point on η axis between the center of the circumcircle of the lower spiral shape and the upper one. The vector $\overrightarrow{R}$ is defined as the projected light blue line to $\xi - \zeta$ plane. The vector $\overrightarrow{R}$ and $o - \xi\eta\zeta$ coordinate move and rotate following the extension and contraction.

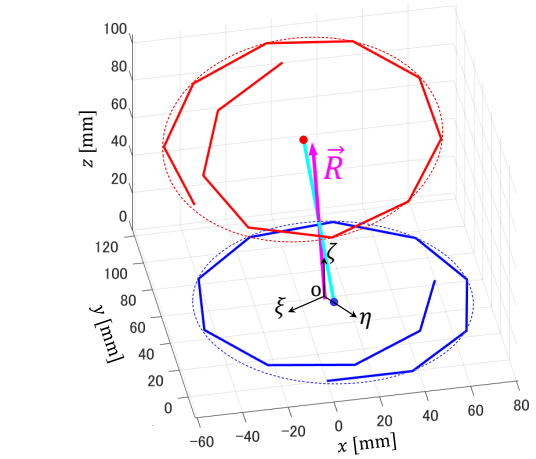

(a) Bird view

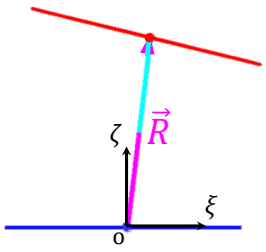

(b) Side view

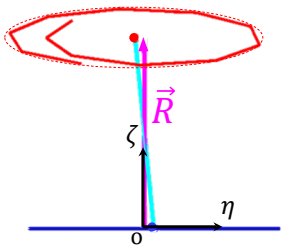

(c) Front view

Figure 3.14: Relative position vector $\vec{R}$ in Origami Spring

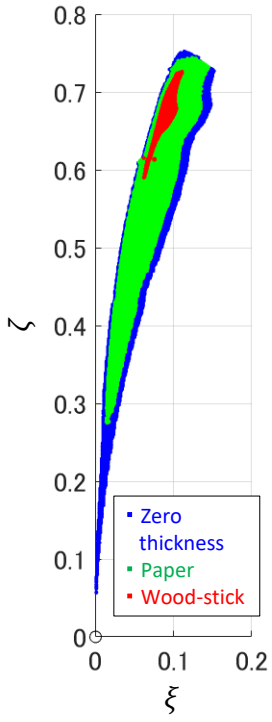

Figure 3.15: Workspace of each type of Origami Spring

The vector $\vec{R}$ of each configuration was used in the workspace analysis. $\|\vec{R}\|$ depends on the longitudinal length a. In Fig. 3.15, workspace normalized with the length of longitudinal side a of each model is shown. The color of workspace corresponds to Fig. 3.12. With extension, the width of workspace becomes wider. Regardless of parameters, ξ cannot be 0. It means that Origami Spring definitely bends during the extension and this can be explained with a spherical 6R linkage but not with a spherical 4R linkage.

In this section, the following were theoretically explained. Among the three variables of Origami Spring, one variable θ_1 contributes to extension mainly and two variables θ_2 and θ_3 take a role to avoid interference of components during the extension and contraction motions even though their ranges are narrow. In addition, the shape of Origami Spring is curved with the narrow range of θ_2 and θ_3. Based on the results above, it can be said that Origami Spring can extend thanks to the thickness and collision of paper.

3.3 Investigation of the Motion with Consideration to Deformation of Components

In the previous section, the configuration space of Origami Spring was proved to be three dimensions, even though the ranges of two DOF were very narrow. In the configuration space where one variable is dominant, the macroscopic motion of Origami Spring with single DOF could be investigated with consideration of strain energy based on the deformation of hypotenuses.

There is the deformation of hypotenuses in paper and wood-stick models with keeping a certain overlapping order. Therefore, all 12 hypotenuses should overlap with each other in the order as same as the longitudinal sides as illustrated in Fig. 3.16. However, the hypotenuses in displacement analysis were just connected the points on the lower and upper planes without deformation so that the hypotenuses were unable to keep their proper order. Based on the distance between the i^{th} and $i+1^{th}$ hypotenuse h_i $(i = 1, 2, \ldots, n-1; n = 12)$ and overlapping order in the configuration, the magnitude of relative deformation of hypotenuse e_i to keep the proper order as shown in Fig. 3.17 was determined and it was normalized with the length of longitudinal side a of each model as same as the previous section. The order of overlapping was verified with comparison of z coordinates of $\mathrm{P}_{h_i,1}$ and $\mathrm{P}_{h_i,2}$ which are intersection points of the normal line and hypotenuses as same as the longitudinal sides in subsection 3.2.1.

The deformation in the perpendicular direction to the hypotenuse was focused on and it was assumed as simple tensile deformation. When the hypotenuses deform

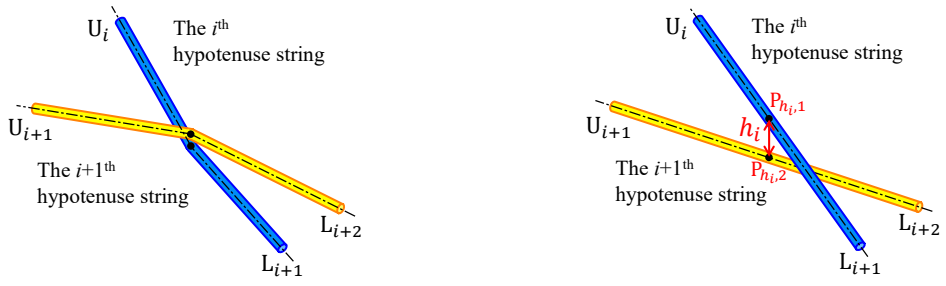

(a) Order in real with deformation

(b) Order reversal in displacement analysis

Figure 3.16: Overlapping order and deformation of hypotenuses

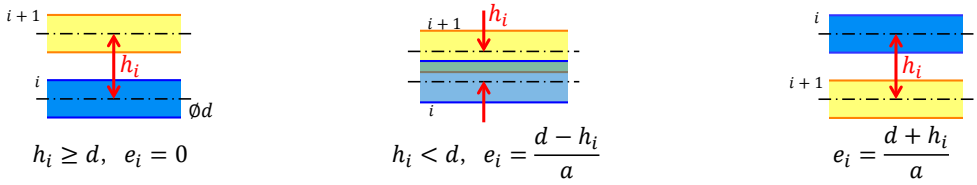

(a) Case1 (b) Case2 (c) Case3

Figure 3.17: Definition of e_i, magnitude of relative deformation of hypotenuses

Table 3.3: Example of two portions A and B of $e_i \neq 0$ when $(\theta_1, \theta_2, \theta_3) = (47.5, 43.0, 38.0)$, $d/a = 10^{-12}$

i	1	2	3	4	5	6	7	8	9	10	11
Target hypotenuses	1, 2	2, 3	3, 4	4, 5	5, 6	6, 7	7, 8	8, 9	9, 10	10, 11	11, 12
e_i	+	+	+	+	0	0	0	0	+	+	+
	A								B		

to keep the proper overlapping order, strain energy was considered to be stored in the hypotenuse. Here, it was assumed that the length and elastic properties of all hypotenuses are the same and the strain energy in the hypotenuse is proportional to ${e_i}^2$. The summation of internal strain energy E_{int} stored in 12 strings was determined as shown in Eq. (3.6). In addition, the bias of strain energy was considered. There are two portions $e_i \neq 0$ as shown in Table 3.3 based on the sign of e_i. The configuration could be assumed as balanced without bias of deformation between two portions. Following this consideration, the difference of the strain energy between two portions E_{dif} was determined as shown in Eq. (3.7).

$$E_{\text{int}} = \sum_{i=1}^{11} {e_i}^2 \tag{3.6}$$

$$E_{\text{dif}} = \left| \sum_{A} {e_i}^2 - \sum_{B} {e_i}^2 \right| \tag{3.7}$$

When both of E_{int} and E_{dif} are small, the configuration is stable without bias of strain energy and such variables set can be found with respect to the dominant variable θ_1. To derive the variables set θ_1, θ_2 and θ_3 which generate stable configurations, the stability index E was considered with E_{int} and E_{dif} as shown in Eq. (3.8).

There was the big difference between the value of E_{int} and E_{dif}, then the weighting coefficient was defined in Eq. (3.9).

$$E = E_{\text{int}} + k \cdot E_{\text{dif}} \tag{3.8}$$

$$k = \frac{\max_{\theta_2,\theta_3} E_{\text{int}}}{\max_{\theta_2,\theta_3} E_{\text{dif}}} \text{ (at a certain } \theta_1) \tag{3.9}$$

In each cross-section with respect to θ_1, the stability index E was calculated and an example is shown in Fig. 3.18. The red points in Fig. 3.18 is that E becomes minimum in the cross-section at a certain θ_1. By picking up a set of θ_2 and θ_3 where E became minimum in each cross-section, the configuration line is derived in the configuration space as shown in Fig. 3.19. Based on the stability of configuration, it can be said that Origami Spring changes its configuration along these configuration lines. Because of that, the macroscopic motion of Origami Spring can be represented

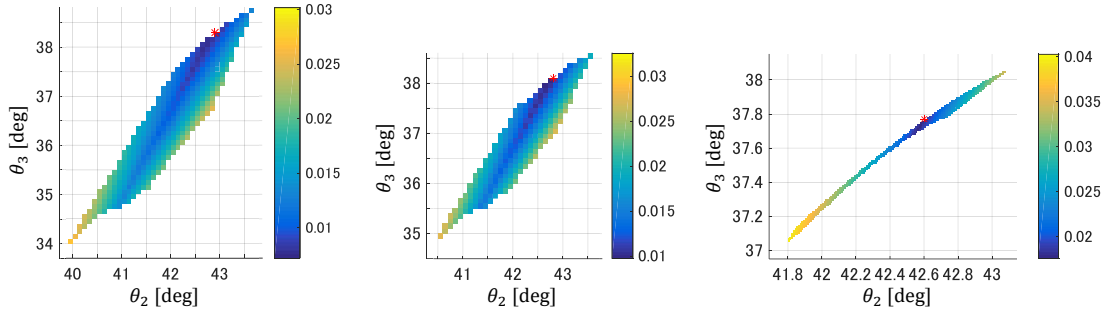

(a) Zero thickness (b) Paper (c) Wood-stick

Figure 3.18: Color maps of stability index E in cross-section $\theta_1 = 47.5$deg

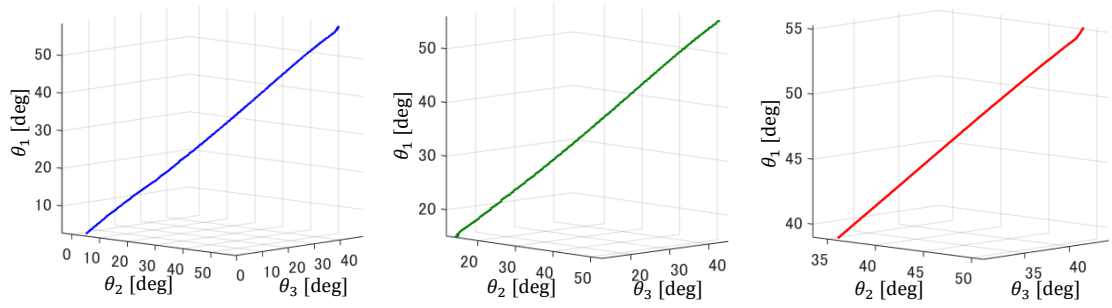

(a) Zero thickness (b) Paper (c) Wood-stick

Figure 3.19: Configuration line derived with consideration to the deformation of hypotenuses

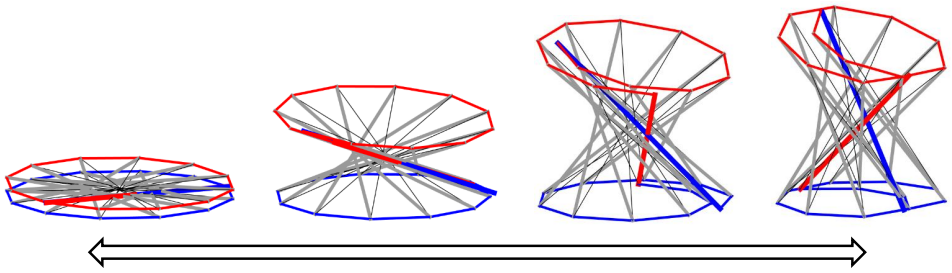

Figure 3.20: 1 DOF motion of Origami Spring along the input line of Fig. 3.19(a)

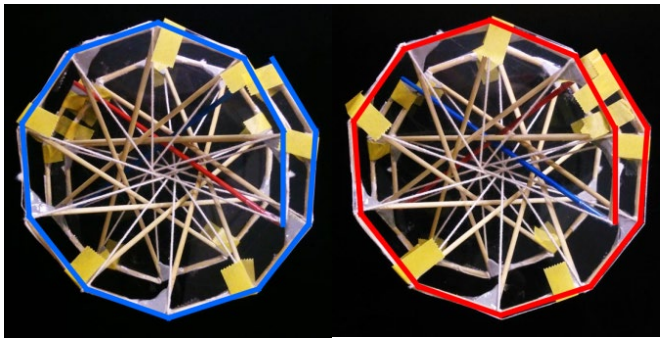

Figure 3.21: Symmetry of spiral shapes of the lateral sides of the unit triangle

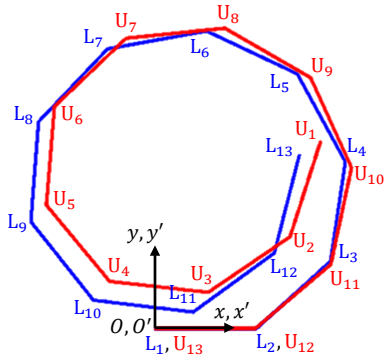

Figure 3.22: Comparison of spiral shapes

as 1 DOF motion as shown in Fig. 3.20 even though it is a 3 DOF mechanism.

To verify the motion along the configuration line corresponds to the motion of Origami Spring, the spiral shapes of the lateral sides of the unit triangles were focused on and compared theoretically. In the observation of motion with both of paper and wood-stick models, the two spiral shapes in lower and upper planes of one segment become symmetric as shown in Fig. 3.21 with the deformation of hypotenuses. Therefore, the two spiral shapes were compared numerically as shown in Fig. 3.22 in all configurations along the configuration line. The lower and upper spiral shapes were overlapped so that $O{-}xy$ and $O'{-}x'y'$ coordinates match as shown in Fig. 3.22. With the distance between L_i and U_{14-i} $(i = 1, 2\ldots, n+1; n = 12)$ normalized with the length of longitudinal side a, a comparison index C was defined.

$$C = \sum_{i=1}^{13} \frac{\left\| \overrightarrow{\mathrm{L}_i \mathrm{U}_{14-i}} \right\|}{a} \tag{3.10}$$

When $C = 0$, the two spiral shapes in the lower and upper planes become symmetric theoretically. Through the calculation of C in all configurations along the three configuration lines, minimum values of C in each cross-section with respect to θ_1 are 0.000 to 0.049. Therefore, in this thesis, the two spiral shapes were regarded as symmetric when $C < 0.05$. As the result, $C < 0.05$ in all configurations along the configuration lines and it can be said that the two spiral shapes in the lower and upper planes of one segment are always symmetric with the configuration lines. This result agrees with the observation of paper and wood-stick models and the motion along the configuration line corresponds to the motion of Origami Spring.

Finally, an explanation of Origami Spring motion was summarized. Origami spring can be kinematically modelled by a spherical 6R linkage and it is a 3 DOF mechanism. Among the three variables of Origami Spring, one variable mainly contributes to extension and the other two variables contribute to the motion to other direction. The ranges of the other two variables are restrained by the collisions of the longitudinal and lateral sides. In addition, with consideration to the deformation of hypotenuses and stability of the configuration, the macroscopic single DOF motion of Origami Spring can be explained.

3.4 Summary

In this chapter, a model of Origami Spring was proposed which consists of rigid and compliant components to consider the collision and deformation of components. The extension characteristic of Origami Spring was clarified as follows with the kinematic model.

1. Origami spring can be modelled as a spherical 6R linkage with three DOF by regarding foldings as revolute joints. The spherical 4R linkage included in the spherical 6R linkage generates rough extension motion and other revolute joints contribute to avoiding the collision of components.

2. Origami Spring can extend without the deformation of components except the hypotenuse. Based on this, an extendable device can be developed with only rigid components.

3. The extension characteristics of Origami Spring, especially configuration space and workspace, are analyzed with the length of longitudinal sides a and the thickness of components d.

4. The hypotenuse limits the motion of Origami Spring, and the single DOF motion of real Origami Spring is the result of the restraint by the hypotenuse.

Chapter 4

Application to an Extendable Arm for Working in a Narrow Space

Based on the concept of an extendable arm which performs some tasks in a narrow space instead of human (Fig. 1.5), this chapter presents a design of a novel rigid extendable arm, which has a large extension ratio, multiple DOF, and can generate a large curvature configuration given by its kinematic structure, beyond those of Origami Spring. Its basic motion is verified through displacement analysis and motion experiments, using an actuated prototype. Kinematic design of the proposed mechanism has been supported by some ideas to maximize its workspace and methods to calculate the actual DOF. An idea for its actuation is also discussed and its validity is confirmed by theoretically and experimentally.

4.1 Mechanism Design and Modeling

4.1.1 Improvement for performance maximization as a multiple-DOF extendable mechanism

As discussed in chapter 3, it is revealed that the actual motion of Origami Spring, a macroscopic single DOF motion, is the result of the constraint by the hypotenuse although it does not have any kinematic role. This fact can be theoretically explained by considering the deformation and potential energy of the hypotenuse string. By removing the hypotenuse, Origami Spring becomes a suitable structure to be ap-

plied to a rigid extendable arm, which has a large extension ratio, multiple DOF, and can generate a large curvature configuration given by its kinematic structure. In addition, it is easier to actuate Origami Spring as compared to other deployable cylindrical origami structures. On the contrary, there are a few disadvantages associated with using an Origami Spring. These disadvantages include the coiling and tilting motions during extension, as shown in Fig. 3.20. These two motions are dependent on each other and caused due to the collision of components, especially the longitudinal sides, thereby leading to a reduction of the workspace volume.

To exploit the features of Origami Spring and achieve maximum performance as an extendable arm, the three issues were addressed by modifying its design: deformation of the hypotenuse, coiling motion, and collision between components.

First, the hypotenuses of the unit triangles were removed, as shown in Fig. 4.1. The deformation of the hypotenuse and the resulting stored potential energy causes the configuration during extension and contraction to be symmetric to the plane between two segments. By removing the hypotenuses, the mechanism can possess complete three DOF and take all configurations in its workspace. Furthermore, the symmetry between segments is also broken.

Second, six unit triangles, which are coiled inside during extension (Fig. 3.20), were removed, as shown in Fig. 4.1, while the value of each dimension being kept identical to that in the original mechanism. As a result, the number of lateral sides was reduced from 12 to 9. On using this modification, coiling does not occur during

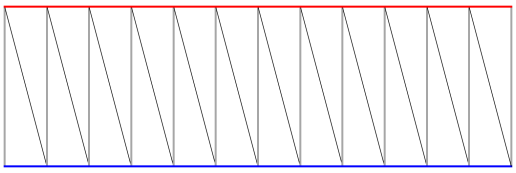

(a) The original 12-sided mechanism - unfolded

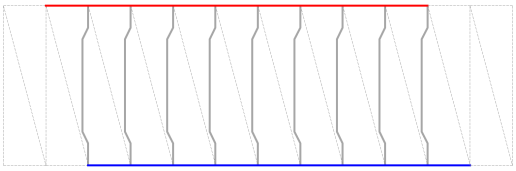

(b) The modified 9-sided mechanism with offset - unfolded

Figure 4.1: One segment folding diagram of the 12- and 9-sided mechanisms

extension, and the mechanism can generate tilting extension motion in all directions as well as pure vertical extension, as shown in Fig. 4.2. These motions cannot be generated by the original 12-sided mechanism.

Third, an offset of the longitudinal sides was introduced, as shown in Figs. 4.1 and 4.2. In the original structure, collisions often occur between longitudinal sides. In addition, the thickness of the components has a significant effect on these collisions, and the workspace narrows as the thickness increases. To decrease collisions while maintaining an adequate thickness of the components to ensure sufficient stiffness, an offset to the longitudinal sides was introduced in the outward direction, even though this would require idle revolute joints.

The novel mechanism was fabricated as a result of these improvements, as shown in Fig. 4.3. The dimensions were $a = 140$ mm, $b = 37.5$ mm, $m = 1$, $n = 12$, and $\varphi = \pi/12$. The revolute joints corresponded to the mountain folded edges in the

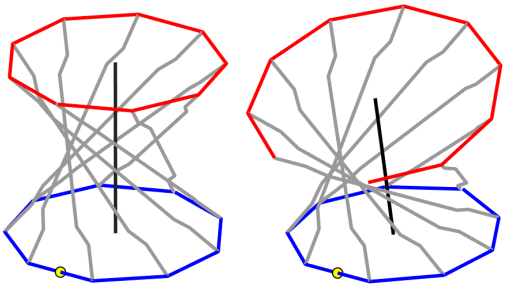

Figure 4.2: Vertical and tilting extension motions achieved by decreasing the number of lateral sides from 12 to 9. The figure also reflects the offset of the longitudinal sides and the deformations of the longitudinal sides.

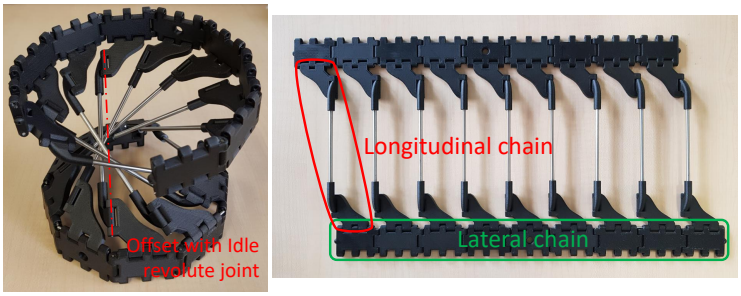

Figure 4.3: Initial prototype of the novel mechanism. The kinematic chain, which consists of lateral side parts, is known as the lateral chain and is similar to the longitudinal chain. A majority of the parts are fabricated using 3D printers (Onyx One, Markforged), and stainless steel is used for the longitudinal parts to ensure high stiffness.

folding diagram and were physically realized using hinges of sufficient thickness and stiffness. These were unlike previous joints composed of thin materials such as paper, film, and cloth. To eliminate the revolute joints corresponding to the hypotenuses, components were added to connect that lateral sides using hinges. After these improvements, the mechanism was still considered to be equivalent to the kinematic model in the previous chapter 3. To introduce the offset in the longitudinal sides, freely rotating idle revolute joints were added, thereby decreasing the collisions between each longitudinal side. As depicted in Fig. 4.3, one segment consists of two lateral chains and nine longitudinal sides. The lateral chain has hinges on both sides; therefore, additional segments can be connected by sharing these lateral chains.

4.1.2 DOF of one segment

The DOF of the one segment novel mechanism was investigated using the loop closure equation. Regarding its structure without idle revolute joints, there are 43 revolute joints and nine kinematic chains, as indicated by the gray lines in Fig. 4.4, that connect the stationary link and the end effector. The nine equations for the velocity of the end effector are written as follows:

$$\begin{bmatrix} \mathbf{s}_i \\ \overrightarrow{\mathbf{P}_i\mathbf{P}_e} \times \mathbf{s}_i \end{bmatrix} \omega_i + \begin{bmatrix} \mathbf{s}_{i+1} \\ \overrightarrow{\mathbf{P}_{i+1}\mathbf{P}_e} \times \mathbf{s}_{i+1} \end{bmatrix} \omega_{i+1} + \cdots = \mathbf{V}_{\mathbf{P_e}} \tag{4.1}$$

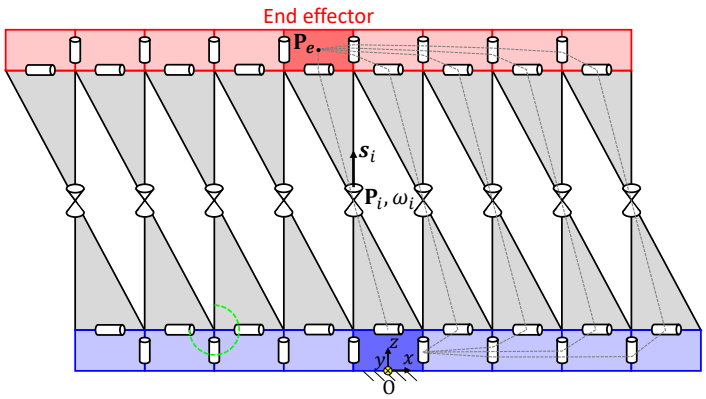

Figure 4.4: Kinematic model for the loop closure analysis. The stationary link is indicated in deep blue, and the end effector is indicated in deep red. There are nine kinematic chains, from the stationary link to the end effector. This kinematic model includes 43 revolute joints.

where $\mathbf{P}_i$ is the position of each revolute joint, $\mathbf{P}_e$ is the reference point of the end effector, $\mathbf{s}_i$ is the unit vector along the axis of each revolute joint, ω_i is the angular velocity of each revolute joint, and $\mathbf{V}_{\mathbf{P_e}} = [\omega; v]$ is the velocity of the end effector. Based on these equations, eight loop closure equations with six dimensions can be derived by eliminating $\mathbf{V}_{\mathbf{P_e}}$ (i.e., 48 scalar equations). By combining them, the following equation is obtained:

$$\mathbf{A} \begin{bmatrix} \omega_1 \\ \omega_2 \\ \vdots \\ \omega_{43} \end{bmatrix} = 0 \tag{4.2}$$

where $\mathbf{A}$ is the 48×43 coefficient matrix. By checking $\dim(\mathrm{Ker}\mathbf{A})$, the number of independent angular velocities and the DOF can be derived. All configurations at the lattice point (angle step: 0.5 deg) $\dim(\mathrm{Ker}\mathbf{A})$ were numerically investigated. The result showed that $\dim(\mathrm{Ker}\mathbf{A})$ was always equal to three. Therefore, the DOF of the one segment novel mechanism was confirmed to be three, which is identical to that of the original design.

4.2 Displacement Analysis

4.2.1 One segment

To demonstrate the improvement of the workspace of the novel mechanism, a displacement analysis was performed. The definition of each point in the mechanism is shown in Fig. 4.5. L_j and U_j $(j = 1, 2, ..., 10)$ are the points in each lower and upper lateral chain, respectively, and $\mathrm{C_L}$ and $\mathrm{C_U}$ are the start and end points of $\overrightarrow{R}$ defined in subsection 3.2.3, Fig. 3.14. In the displacement analysis, the variables are θ_4, θ_5, and θ_6 (angle step: 0.5 deg) because the 5^{th} lateral side is the middle of the lateral chain and θ_4 and θ_6 are useful to represent the tilting configuration. The output is the position and orientation of coordinate $\mathrm{O}' - x'y'z'$ at the middle of U_5 and U_6. These are shown in Figs. 4.5 and 4.6. In the displacement analysis, it is assumed that the longitudinal side is given the offset in the direction of the bisector

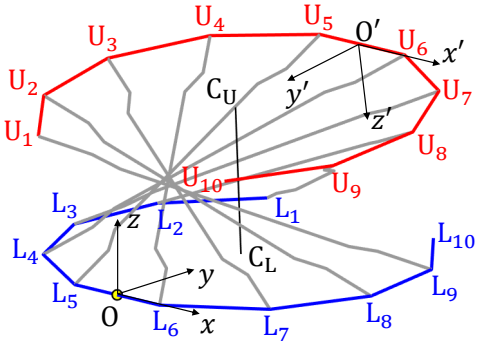

Figure 4.5: Definition of points

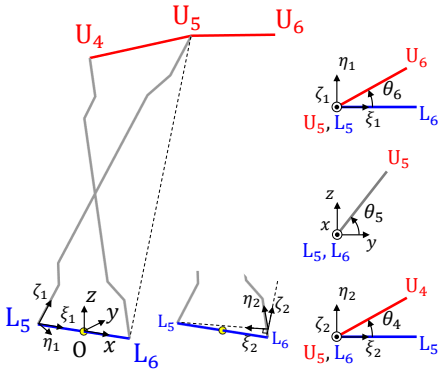

Figure 4.6: Definition of inputs for one segment: θ_4, θ_5, and θ_6

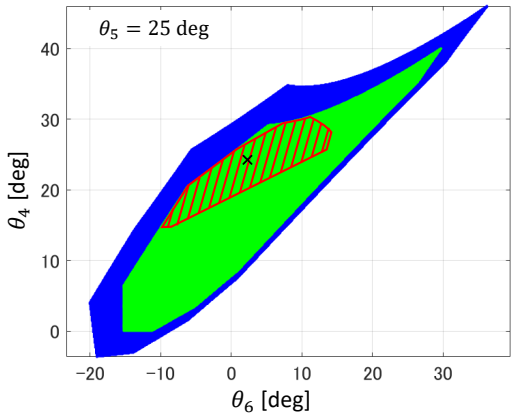

Figure 4.7: Cross section of the configuration space at $\theta_5 = 25$ deg. The red area indicates the cross section of the original version with 12 lateral sides. The green area represents the cross section of the version with nine sides, without an offset. The blue area indicates the cross section of the novel mechanism. The configuration space becomes wider with the modification.

of θ_6. The configuration space was defined as the region of θ_4, θ_5, and θ_6 at which the condition was satisfied; the condition was that the components do not interfere with each other. As a result, the configuration space of the novel mechanism was larger than that of the original mechanism for all cross sections of θ_5, as shown in Fig. 4.7. This indicates that its workspace is much larger than that of the original, as shown in Table 4.1 and Fig. 4.8, where the definitions of the tilt angle ψ and curvature radius ρ are depicted in Fig. 4.9.

The right tilt angle was greater than the other angles by a factor of two, because there were fewer longitudinal chains in the right as compared to those in the other

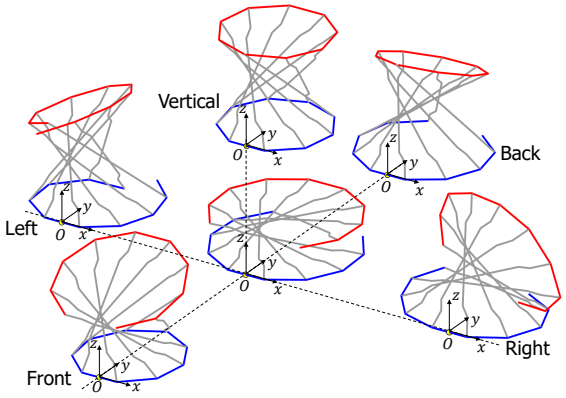

Figure 4.8: Configurations at the boundary of the workspace. The figure shows the maximum tiling configuration along each direction and the maximum vertical extension.

Table 4.1: Metrics of the configurations at the workspace boundary

Direction	Max tilt angle ψ [deg]	Min curvature radius ρ [mm]
Front	21.6	114
Back	21.2	112
Left	24.6	210
Right	**46.9**	**75.0**
(Original)	(17.2)	(345)

*Initial radius: $a/\cos\varphi = 72.5$ mm

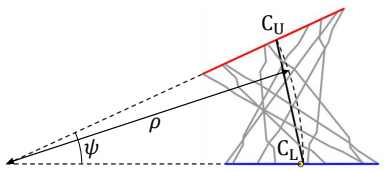

Figure 4.9: Definition of tilt angle ψ and curvature radius ρ

directions, as can be seen in Fig. 4.8. It is remarkable that the minimum curvature radius in the right direction can be as small as the initial radius of this mechanism. In addition, the minimum curvature radius and the largest tilt angle can be simultaneously generated. Thus, the novel mechanism can generate a configuration with a large curvature, using a few segments. This is a distinct advantage of this mechanism.

Here, three inputs of a segment can be redefined as $\|\overrightarrow{L_1L_{10}}\|$, $\|\overrightarrow{U_1U_{10}}\|$, and θ_l; the angle of $\overrightarrow{L_1L_{10}}$ against x axis is shown in Fig. 4.10 because the condition

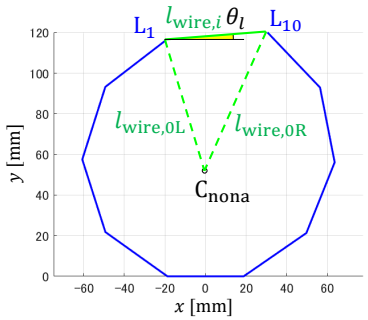

Figure 4.10: Two inputs in the lower lateral chain: $\|\overrightarrow{\mathrm{L_1L_{10}}}\|$ and θ_l. The relation between $l_{\mathrm{wire},i}$, θ_l, $l_{\mathrm{wire,0L}}$, and $l_{\mathrm{wire,0R}}$ is also shown which is mentioned in subsection 4.3.1. $\mathrm{C_{nona}}$ is the center of the nonagon when the mechanism is fully extended.

Table 4.2: Relation between the inputs condition and extension direction

Direction	Condition of θ_4 and θ_6	Condition of $\|\overrightarrow{\mathrm{L_1L_{10}}}\|$
Front	Small θ_4, $\theta_6 = 0$	$\|\overrightarrow{\mathrm{L_1L_{10}}}\| < \|\overrightarrow{\mathrm{U_1U_{10}}}\|$
Back	Large θ_4, $\theta_6 = 0$	$\|\overrightarrow{\mathrm{L_1L_{10}}}\| > \|\overrightarrow{\mathrm{U_1U_{10}}}\|$
Left	Small θ_4, $\theta_6 < 0$	$\theta_l > 0$
Right	Large θ_4, $\theta_6 > 0$	$\theta_l < 0$
Vertical	$\theta_6 = 0$	$\|\overrightarrow{\mathrm{L_1L_{10}}}\| = \|\overrightarrow{\mathrm{U_1U_{10}}}\|$, $\theta_l = 0$

of variables θ_4, θ_5, and θ_6 for each extension direction cannot be expressed with equation as shown in Table 4.2. Among the redefined inputs, the difference in the two distances $\|\overrightarrow{\mathrm{L_1L_{10}}}\|$ and $\|\overrightarrow{\mathrm{U_1U_{10}}}\|$ generates the tilting motion in the front/back, and the positive/negative angle θ_l generates the tilting motion in the left/right as summarized in Table 4.2.

4.2.2 Multiple segments

To perform the displacement analysis corresponding to the motion of the prototype, the DOF of the novel mechanism with multiple segments is considered.

To reveal the extent of change in the configurations of the novel and original mechanisms where the lower point's positions are almost fixed, the possible configurations were explored. For comparison, the ranges of the normal vector of the upper plane and the length $\|\overrightarrow{\mathrm{U_1U_{10}}}\|$ were analyzed for the condition where 10% of the representative length a is the maximum change in the position of the lower point. The middle point of the configuration space of the 12-sided version shown in Fig. 4.7 was

considered as an example. In Fig. 4.11, the black line represents the normal vector of this configuration, and the three areas depict the range of the normal vector of the upper plane. As shown in Fig. 4.11, the normal vector range of the novel mechanism is wider than that of the original mechanism, especially along the direction of the y axis. The range of $\|\overrightarrow{U_1U_{10}}\|$ is presented in Table 4.3. The range of $\|\overrightarrow{U_1U_{10}}\|$ of the novel mechanism is 88 mm; this is 86% of the maximum range and exceeds the range of the original mechanism by a factor of 2.4.

These results revealed that the novel mechanism has additional possible configurations and the potential to dramatically change its configuration with small errors

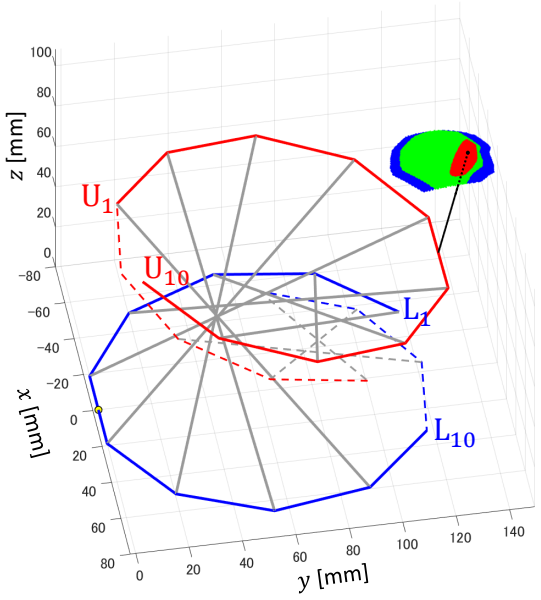

Figure 4.11: Comparison of possible configurations. This configuration corresponds to the inputs of the point in Fig. 4.7. The black line represents the normal vector of the upper plane. The three areas around the end of the black line represent the movement of the normal vector within the permissible change in the shape of the lower lateral side. Similar to Fig. 4.7, each color represents a different version of the mechanism.

Table 4.3: Range of the length $\|\overrightarrow{U_1U_{10}}\|$

Type of mechanism	Range of distance [mm]
12 sides ver.	36
9 sides ver.	83
9 sides offset ver.	88

*Maximum range: 102mm

at the lower positions of each segment. Therefore, when the configuration of a segment is decided using three inputs (i.e., $\|\overrightarrow{\mathrm{L_1L_{10}}}\|$, $\|\overrightarrow{\mathrm{U_1U_{10}}}\|$, and θ_l), its two adjacent segments need another input to decide each of their configurations in a mechanism with multiple segments. Each lateral chain is shared by the two adjacent segments, except the base and top segments, as shown in Fig. 4.12. With respect to a lateral chain, the two inputs of the upper segment, $\|\overrightarrow{\mathrm{L_1L_{10}}}\|$ and θ_l, are already determined by the lower segment. Therefore, the bottom segment requires three inputs, and the other segments require a single input $\|\overrightarrow{\mathrm{U_1U_{10}}}\|$ to determine their configurations. To summarize, a mechanism with m segments has $m+2$ DOF, and practical examples of the input variables are the lengths $l_{\mathrm{wire},i}$ $(i = 0, 1, ..., m)$ and θ_l in the base lateral chain.

Displacement analysis of the multiple segments can be performed using the input variables; however, it is complicated to directly derive a configuration based on the lengths $l_{\mathrm{wire},i}$ and angle θ_l. Therefore, for simplicity, the lookup table method was employed. The table for one segment was created as follows:

1. Provide the three input angles for the displacement analysis of one segment: θ_4, θ_5, and θ_6;
2. Gather configurations that satisfy the restraint conditions;
3. Calculate $l_{\mathrm{wire},i}$, $l_{\mathrm{wire},i+1}$ and θ_l for each configuration;
4. Create a table with the relationships between (θ_4, θ_5, θ_6) and ($l_{\mathrm{wire},i}$, $l_{\mathrm{wire},i+1}$, θ_l).

Based on the input variables: lengths $l_{\mathrm{wire},i}$ and the angle θ_l, the configuration of each segment can be selected from the table, from the bottom segment to the top segment. As an example, a configuration of the three-segment mechanism is presented in Fig. 4.12 with five inputs variables: $l_{\mathrm{wire},0}$, $l_{\mathrm{wire},1}$, $l_{\mathrm{wire},2}$, $l_{\mathrm{wire},3}$, and θ_l.

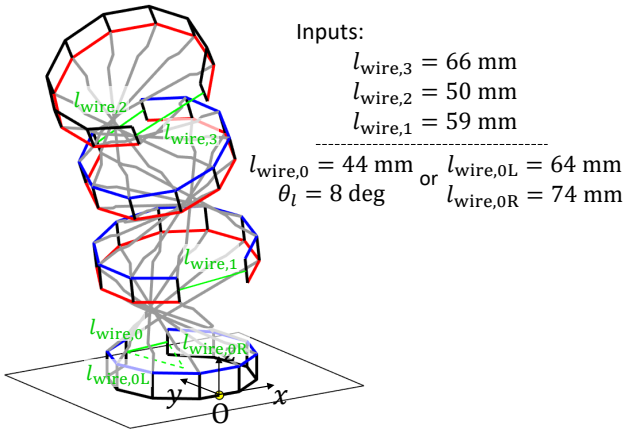

Figure 4.12: Example of the entire configuration of the mechanism with multiple segments obtained via displacement analysis. The lookup table method is applied with five input values for the mechanism.

4.3 Proof of Concept

4.3.1 Actuation method

To develop an actuated prototype based on the example of the input variables presented in subsection 4.2.2, a number of design principles were considered: the actuators must be placed at the center of the lateral chain and symmetry should be maintained, the input values should be observable, and the actuators on the upper segments should be sufficiently small to fit in the inner space. Moreover, the torque output of the actuator is related to, and limited by, the size of the actuator. Consequently, the wire driven strategy by a rotary actuator was introduced, because the output torque of the rotary actuator can be adjusted by changing the pulley diameter. Similar to the general wire driven strategy, a leaf spring was inserted to apply tension on the wire for the counter actuation.

The prototype with three segments consists of four lateral chains, as shown in Fig. 4.13, and requires five inputs based on the discussion of DOF in previous section: $l_{\mathrm{wire},0}$, $l_{\mathrm{wire},1}$, $l_{\mathrm{wire},2}$, $l_{\mathrm{wire},3}$, and θ_l. About two inputs in the base lateral chain: $l_{\mathrm{wire},0}$ and θ_l, it is much more effective and simpler to change two wire lengths than one wire length and its angle. Therefore, $l_{\mathrm{wire},0}$ and θ_l were replaced by $l_{\mathrm{wire},0\mathrm{L}}$ and $l_{\mathrm{wire},0\mathrm{R}}$, as shown in Fig. 4.10. $\mathrm{C}_{\mathrm{nona}}$ is the center of the nonagon when the mechanism is

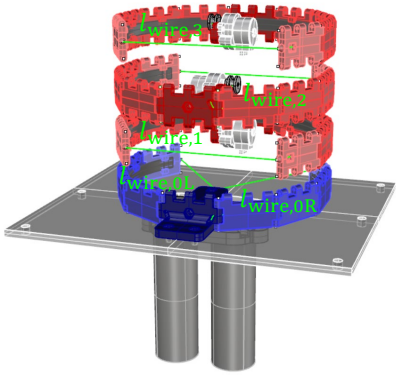

Figure 4.13: Arrangement of four lateral chains for three segments. The five inputs are $l_{\mathrm{wire,0L}}$, $l_{\mathrm{wire,0R}}$, $l_{\mathrm{wire,1}}$, $l_{\mathrm{wire,2}}$ and $l_{\mathrm{wire,3}}$.

Table 4.4: Relation between the inputs and extension direction

Direction	Condition of $\|\overrightarrow{\mathrm{L_1L_{10}}}\|$, $\|\overrightarrow{\mathrm{U_1U_{10}}}\|$, and θ_l	Condition of $l_{\mathrm{wire},i}$, $l_{\mathrm{wire},i+1}$, $l_{\mathrm{wire,0L}}$, and $l_{\mathrm{wire,0R}}$
Front	$\|\overrightarrow{\mathrm{L_1L_{10}}}\| < \|\overrightarrow{\mathrm{U_1U_{10}}}\|$	$l_{\mathrm{wire},i} < l_{\mathrm{wire},i+1}$
Back	$\|\overrightarrow{\mathrm{L_1L_{10}}}\| > \|\overrightarrow{\mathrm{U_1U_{10}}}\|$	$l_{\mathrm{wire},i} > l_{\mathrm{wire},i+1}$
Left	$\theta_l > 0$	$l_{\mathrm{wire,0L}} < l_{\mathrm{wire,0R}}$
Right	$\theta_l < 0$	$l_{\mathrm{wire,0L}} > l_{\mathrm{wire,0R}}$
Vertical	$\|\overrightarrow{\mathrm{L_1L_{10}}}\| = \|\overrightarrow{\mathrm{U_1U_{10}}}\|$, $\theta_l = 0$	$l_{\mathrm{wire},i} = l_{\mathrm{wire},i+1}$, $l_{\mathrm{wire,0L}} = l_{\mathrm{wire,0R}}$

fully extended. By using $l_{\mathrm{wire,0L}}$ and $l_{\mathrm{wire,0R}}$ instead of $l_{\mathrm{wire,0}}$ and θ_l, the condition of inputs for each extension direction can be expressed with lengths as shown in Table 4.2 and the configuration of the prototype can be imagined more intuitively. According to this replacement, the information regarding $l_{\mathrm{wire,0L}}$ and $l_{\mathrm{wire,0R}}$ was added to 3^{rd} and 4^{th} steps of the table creation mentioned in subsection 4.2.2 for the displacement analysis of multiple segments, and the same configuration can be represented by the two inputs sets as shown in Fig. 4.12. The blue lateral chain represents the base lateral chain, which includes the stationary part, and the red lateral chain represents the upper lateral chains. The base lateral chain (Fig. 4.14) includes two actuators (FAULHABER, Brushless DC motor, 3042W036C) to pull two wires and change $l_{\mathrm{wire,0L}}$ and $l_{\mathrm{wire,0R}}$. To ensure that the lengths of the input wire are observable regardless of the configuration, the wires pass through the corners of the polygon. The leaf spring was fixed only to the stationary part to ensure that it can slide against the other lateral side parts, when the shape of the lateral chain

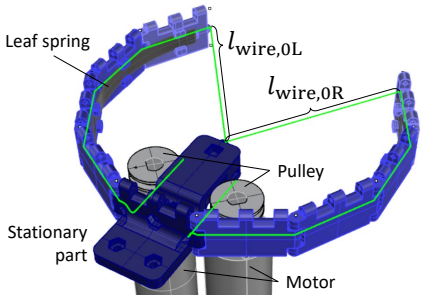

Figure 4.14: Design of the base lateral chain. The distance and angle between the two edges are determined based on the length of the two wires. The end of two wires are fixed to the stationary part. To measure the input lengths, regardless of the configuration, the wires pass through the corners of the polygon, where the path length is constant.

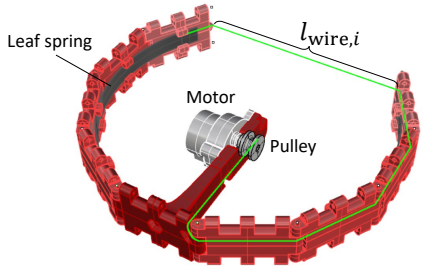

Figure 4.15: Design of the upper lateral chain. Similar to the base lateral chain, the wires pass through the corners of the polygon.

changes. In addition, the upper lateral chain (Fig. 4.15) has one actuator (Copal Electronics, Stepping motor, SPG20-1332, max torque: 75 mN·m) that fits in the inner space. The wire path and leaf spring are identical to those in the base lateral chain. To support the payload on the end effector by the small actuator shown above, the radius of the small pulley was determined to be 3.2 mm for actuating the upper two segments (one segment: 169 g).

The loop closure equation as same in subsection 4.1.2 was used to confirm that this actuation method gives proper inputs to the mechanism, with the following equation;

$$\mathbf{A}_{\mathrm{a}}\omega_{\mathrm{a}} + \mathbf{A}_{\mathrm{p}}\omega_{\mathrm{p}} = 0 \tag{4.3}$$

where ω_{a} is the 3×1 vector with angular velocities of three chosen active revolute joints, ω_{p} is the 40×1 vector with angular velocities of 40 passive revolute joints, $\mathbf{A}_{\mathrm{a}}$ is the 48×3 coefficient matrix, and $\mathbf{A}_{\mathrm{p}}$ is the 48×40 coefficient matrix. The

matrix $\mathbf{A}$ in (4.2) is divided into $\mathbf{A}_\mathrm{a}$ and $\mathbf{A}_\mathrm{p}$ according to distinction of joints between active and passive. When the three chosen revolute joints are independent, $\dim(\mathrm{Ker}\mathbf{A}_\mathrm{p})$ is 0; these joints are appropriate as active joints. All combinations of three joints among 43 joints were investigated. When three joints are chosen from the same spherical chain as shown by the green line in Fig. 4.4, $\dim(\mathrm{Ker}\mathbf{A}_\mathrm{p})$ becomes 1, which means that one active joint is dependent on the others. However, for every combination except the combinations above, $\dim(\mathrm{Ker}\mathbf{A}_\mathrm{p})$ is equal to 0. The introduced actuation method, which changes the distance between two ends of each lateral chain, is not the exception and gives appropriate inputs to the mechanism.

4.3.2 Motion experiment

The setup for the prototype motion experiment is presented in Fig. 4.16. 13 V and 2.00 A were applied to each DC motor and 13 V and 0.30 A were applied to each stepping motor. The prototype was manually controlled using five analog switches. The extension ratio was 290 %, increasing from 135 mm to 392 mm. Actually, the extension ratio was significantly influenced by the width of the lateral side part. If the width were to be decreased to zero, the extension ratio could be a maximum value of 592 %, increasing from 48 mm to 284 mm.

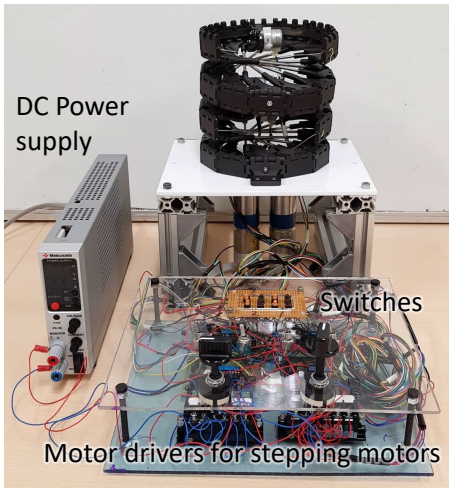

Figure 4.16: Experimental setup. The prototype includes two DC motors (FAULHABER, Brushless DC motor, 3042W036C) and three Stepping motors (Copal Electronics, SPG20-1332, max torque: 75 mN·m) and they are manually controlled using five analog switches.

To validate the availability of the actuation method, extensional and contractional motions (Fig. 4.17, duration: 96 sec.), swing motions from right to left and vice versa (Fig. 4.18, duration: 56 sec.), and full extensional (392 mm height) and load trials (Fig. 4.19) were conducted. First, the prototype could successfully go back to the fully contracted configuration through the extension and contraction. Second, the prototype approximately achieved the desired configuration (inputs: $l_{\mathrm{wire,0L}} = 64$, $l_{\mathrm{wire,0R}} = 74$, $l_{\mathrm{wire},1} = 59$, $l_{\mathrm{wire},2} = 50$, $l_{\mathrm{wire},3} = 66$ [mm]) compared with the displacement analysis, although a discrepancy was observed. The discrepancy is mainly attributed to the compliance of the mechanism. Third, the expected swing motion was achieved, owing to the difference in the input length between $l_{\mathrm{wire,0L}}$ and $l_{\mathrm{wire,0R}}$. Fourth, when the prototype is fully extended, it has a moderate stiffness exceeding 19.6 N (2 kg) against the vertical load. In addition, various configurations were generated, including S-shapes (Fig. 4.20), and maximum tilting configurations to the front (Fig. 4.21a) and to the right (Fig. 4.21b) were also achieved. The achievable, minimum curvature radius for the S-shape configuration is 114 mm. The tilt angle ψ and curvature radius ρ of each segment in the maximum tilting configurations are corresponding to the values in Table 4.1.

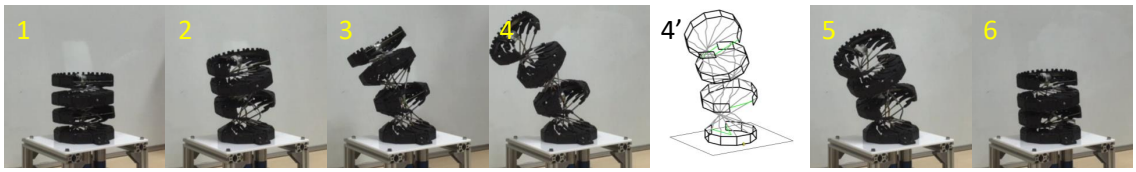

Figure 4.17: Extension and contraction. The output configuration at the 4th frame is compared with the result of the displacement analysis. This configuration is based on the following inputs: $l_{\mathrm{wire,0L}} = 64$, $l_{\mathrm{wire,0R}} = 74$, $l_{\mathrm{wire},1} = 59$, $l_{\mathrm{wire},2} = 50$, and $l_{\mathrm{wire},3} = 66$ mm. The prototype approximately achieves the desired configuration, although a few errors exist.

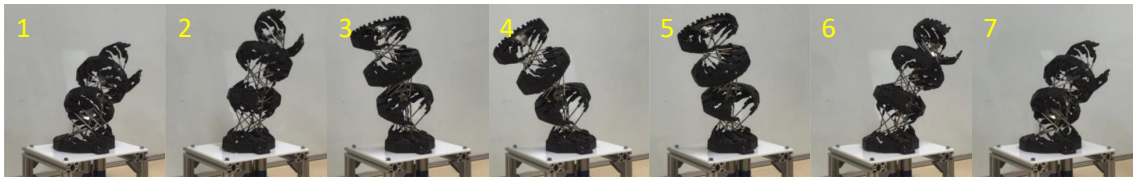

Figure 4.18: Swinging from right to left and vice versa. When $l_{\mathrm{wire,0L}}$ is longer than $l_{\mathrm{wire,0R}}$, the prototype tilts to the right. Conversely, when $l_{\mathrm{wire,0R}}$ is longer than $l_{\mathrm{wire,0L}}$, the prototype tilts to the left.

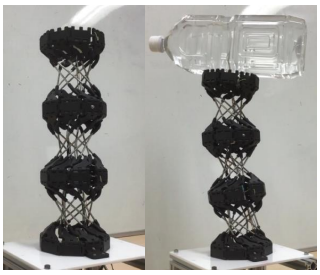

Figure 4.19: Fully extended shape and load trial, using a 2-L plastic bottle filled with water (2 kg) as the vertical load

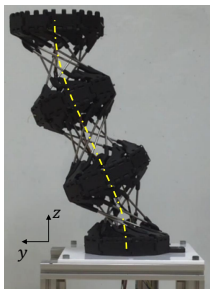

Figure 4.20: Example of an S-shape configuration with inflection points

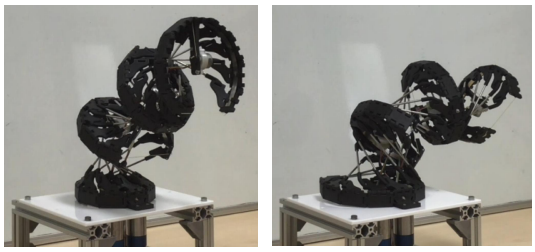

(a) Front (b) Right

Figure 4.21: Generation of maximum tilting configurations at the workspace boundary corresponding to Fig. 4.8. (b) In this configuration, the curvature attains its maximum value.

These motion experiments confirmed the validity of the design and the actuation methods presented in this chapter. About the method of actuating the base lateral chain, it is appropriate to ensure a difference between $l_{\mathrm{wire,0L}}$ and $l_{\mathrm{wire,0R}}$, which is equal to the angle θ_l, as shown in Fig. 4.10. Furthermore, it is also appropriate to shorten the length $l_{\mathrm{wire,0}}$, except the end of the extension in which the base lateral chain needs to be completely closed such that $l_{\mathrm{wire,0}} = 0$. This insufficiency leads to the displacement discrepancy mentioned above. To address this issue, an additional wire having the same path as the upper lateral chain can be introduced as a possible solution in the future. In addition, the configuration of the lateral chain is kept by the tension of the wire and the counter force of the leaf spring, but this actuation cannot deal with an external force which is applied to close the lateral chain. To develop the proposed extendable arm (Fig. 1.5) which performs heavy labor by exploiting the contact forces with narrow spaces, the actuation method for the contraction motion needs to be reconsidered.

For the real use of this extendable arm, the strategy to control its configuration along a target narrow space needs to be considered. A target narrow space can be described with the length between each inflection point and the bending angle at inflection points. Based on these information, the configuration of the extendable arm needs to be decided. The configuration of each segment is dependent on the configurations of next segments. To generate a desired configuration along a target

narrow space, the table which was created in subsection 4.2.2 is not sufficient, and the position and orientation of the coordinate $O' - x'y'z'$ in the coordinate $O - xyz$ (Fig. 4.5), the extension length, the tilting angle and the tilting direction of each configuration need to be added to the table. A system needs to be developed to show the possible configuration of each segment when the configuration of one segment is decided, using the table.

When the configuration of prototype was compared with the configuration derived by the displacement analysis, the discrepancy was observed. The discrepancy is attributed to the joint clearance, the deformation of components, and the difference of the posture of the longitudinal side, which was given an offset and rotates with idle revolute joints, between the prototype and the displacement analysis. The discrepancy between the prototype and the displacement analysis will be decreased by reflecting the rotation of the longitudinal side in the displacement analysis with the collision between other longitudinal sides.

4.4 Tapered Extendable Arm with Modified Folding Diagram

As mentioned in previous subsection 4.3.2, when output configurations were compared with the results of theoretical analysis, there was a discrepancy mainly related to the compliance of the mechanism. Configuration discrepancy caused by the compliance was attributed to two aspects. The first one is the issue of an overconstrained mechanism. An origami inspired mechanism is an overconstrained mechanism generally, then the force analysis of the overall mechanism is indeterminate and its behavior is sensitive to joint clearance and dimensional errors. As the first step to analyze its compliance, the static analysis has been performed and the non-overconstrained kinematically equivalent mechanism has been proposed which has superior static characteristics [59]. The other aspect is the shape of and the mass distribution in the mechanism. The arm is expected to move into the narrow space by sequential extension from the bottom to top segments for simple control, as shown in Figs. 1.5 and 4.22, and it means that the diameters of lower segments become short earlier

Figure 4.22: Big head shape during sequential extension

than those of upper segments. With such big head shape, its static performance is significantly influenced by the pose of the upper segments. A possible simple solution to this problem is to give a tapered shape by modifying the folding diagram of Origami Spring. With a tapered shape, the mass at distal segment becomes smaller, and these would improve the stability of configuration.

In this section, to improve static performance of the origami inspired extendable arm as the first step for practical use, a tapered shape was given to it by modifying the folding diagram of the original origami, and its effect on the static performance was verified with experiments and a quasi-static analysis.

4.4.1 Modification of the folding diagram

To implement a tapered shape in Origami Spring, diameters of the segments need to decrease according to the height from bottom to top as shown in Fig. 4.23. Here, the two circumcircles of the regular polygons were focused on when one segment is fully contracted. To reflect the idea into the folding diagram, r_D is defined as the ratio of upper circumcircle's diameter D_{U} to lower one D_{L} as shown in Fig. 4.24 and the right triangle was changed to an obtuse-angled triangle and acute-angled triangle. This modification was introduced in section 2.3. As an example, the folding diagram with $r_D = 0.884$ is shown in Fig. 4.25 and the fully-extended shape is shown in Fig. 2.13(b). In this section, this ratio was used as an example applied for prototype and a quasi-static analysis.

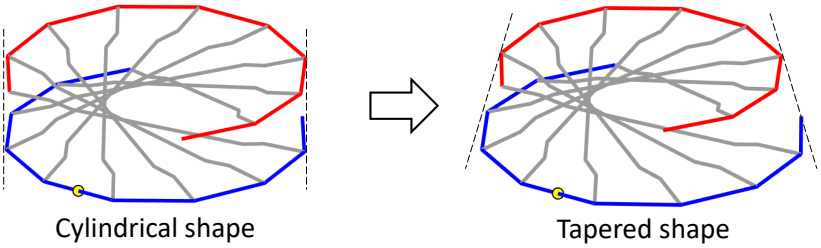

Figure 4.23: Idea to implement a tapered shape in Origami Spring

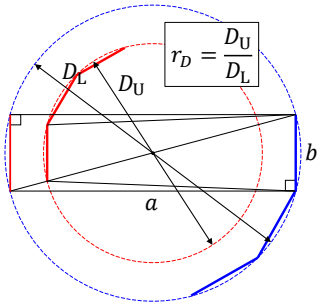

Figure 4.24: Ratio of lower to upper diameters r_D

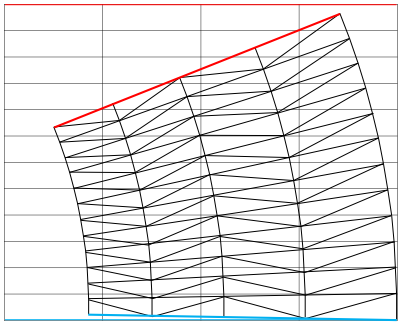

Figure 4.25: Modified folding diagram

4.4.2 Observation of prototypes' behavior

Based on the modified Origami Spring, the tapered prototype is designed as shown in Fig. 4.26(b) and assembled like Fig. 4.27(b) with 3D printed parts by Mark-Two (Markforged). In the design of prototypes, $a = 140$ mm, $b = 37.5$ mm and $r_D = 0.884$. The extendable arm which consists of m segment has $m + 2$ DOF and the prototypes have 6 DOF. As same as in the cylindrical prototype, the wire driven strategy with rotary actuators was introduced, and the inputs are the lengths of wires $l_{\mathrm{wire,0L}}, l_{\mathrm{wire,0R}}$,and $l_{\mathrm{wire,1\sim4}}$ as shown in Fig. 4.26. The leaf springs were inserted to apply tension on the wires for counter actuation.

The specifications of each prototype are shown in Table 4.5. The mass of the tapered prototype was 481 g and the cylindrical one was 676 g resulting in 29 % mass reduction by the improvement. The extension ratio was the ratio of the extended height to the contracted one. The extension ratio of the tapered prototype keeps 2.4 which was 86 % of the cylindrical one even though the representative length of each segment becomes shorter by the modification of the folding diagram.

As the motion experiments, the maximum tilting configurations to each direc-

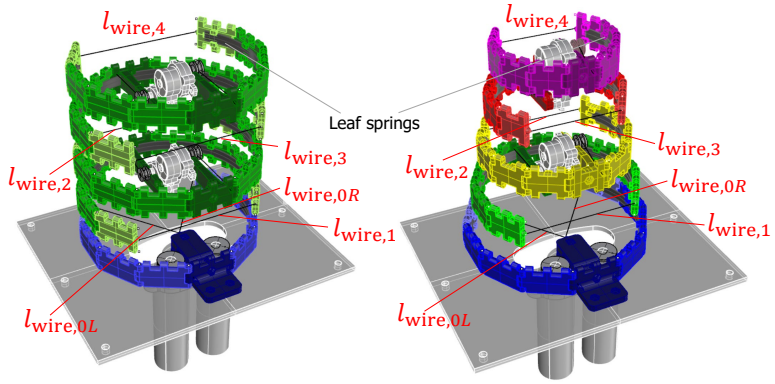

(a) Cylindrical version (b) Tapered version

Figure 4.26: Design of each prototype

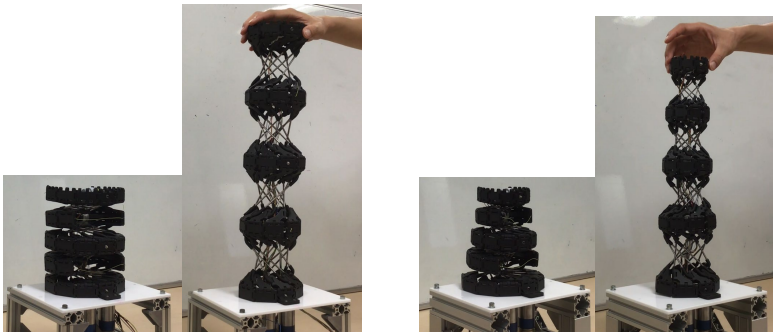

(a) Cylindrical version (b) Tapered version

Figure 4.27: Extension of each prototype

Table 4.5: Mass and extension ratio

	Cylindrical ver.	Tapered ver.
Mass [kg]	**0.676**	**0.481**
Contracted height [mm]	173	175
Extended height [mm]	489	413
Extension ratio	2.8	2.4

tion were compared between the tapered and cylindrical prototypes as shown in Fig. 4.28. The upper pictures are the tapered prototype and the lower pictures are the cylindrical one. Thanks to the reduction of distal segments' mass, the motion and configuration of tapered prototype were seen more stable than those of the cylindrical one while keeping to generate various configurations. Based on this observation, the improvement seems to have a good effect on the static performance.

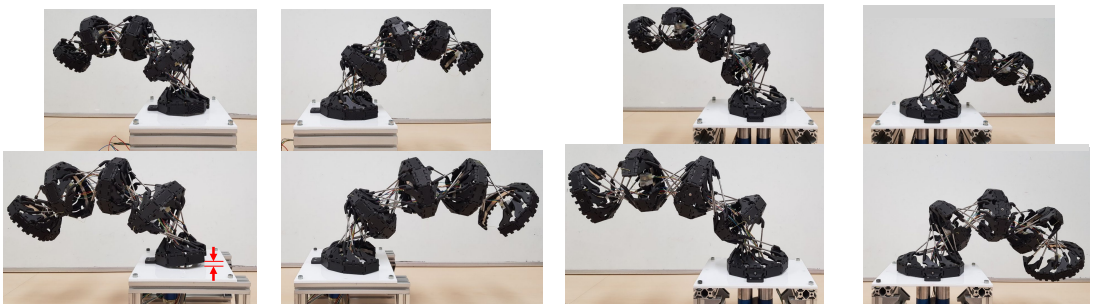

(a) Front (b) Back (c) Left (d) Right

Figure 4.28: Comparison of maximum tilting configurations to each direction. The upper pictures are the tapered prototype and the lower pictures are the cylindrical one

4.4.3 Quasi-static analysis

To theoretically verify the effect of the improvement, the quasi-static analysis of one segment was carried out with the GIM® software [60]. The kinematic model for the analysis is shown in Fig. 4.29, which is based on the non-overconstrained kinematically equivalent mechanism in [59]. The input wires in the prototypes were modelled as pistons and the input forces were determined as $F_{0\mathrm{L}}$, $F_{0\mathrm{R}}$ and F_1. In this analysis, contraction force of the piston was positive force. The geometry of the output link is defined as shown in Fig. 4.29. h corresponds to the height of the center of gravity in the upper three segments and w corresponds to the radius of the inscribed circle of the nonagon at the end of the vertical extension. For the tapered model: $h = 54.0$ mm and $w = 45.6$ mm and for the cylindrical one: $h = 57.5$ mm and $w = 51.5$ mm. Gravitational force at the output link with each mass in Table 4.5 was considered. The target motions ware the maximum extensions to each direction (Fig. 4.30) in 1 sec, and lengths of the pistons $l_{\mathrm{wire},0\mathrm{L}}, l_{\mathrm{wire},0\mathrm{R}}$ and $l_{\mathrm{wire},1}$ changed at a constant speed.

As the result of this analysis, the ratios of the forces in tapered and cylindrical models F_{Tap} and F_{Cyl} in each input force are shown in Fig. 4.31. In the marked areas A and B in Fig. 4.31(a), the values become larger than 1, however, these are not needed to care, since the sign of F_1 changes with small magnitude at area A in the right direction extension and the magnitude of F_1 is almost zero at area B in the vertical extension. About F_1, the ratio is around 70 % and it corresponds to that the mass was reduced to 71 %. What the notable is, about $F_{0\mathrm{L}}$ and $F_{0\mathrm{R}}$ in the

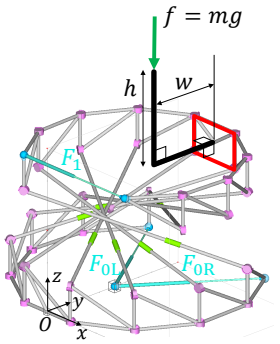

Figure 4.29: Kinematic model in GIM® for quasi-static analysis

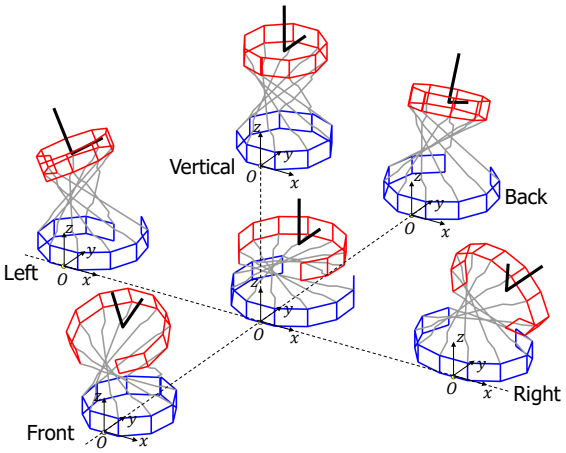

Figure 4.30: Target motions for quasi-static analysis

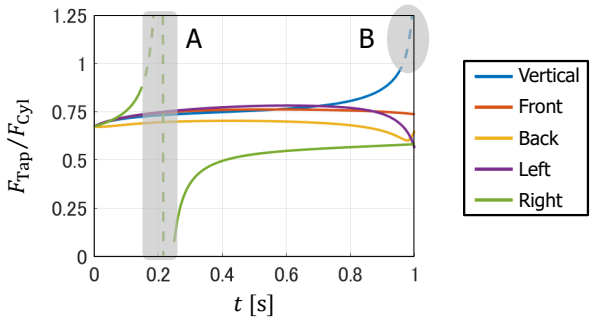

(a) F_1

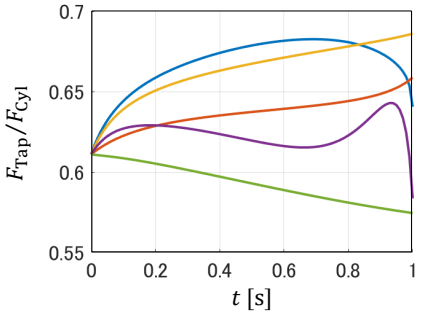

(b) $F_{0\mathrm{L}}$

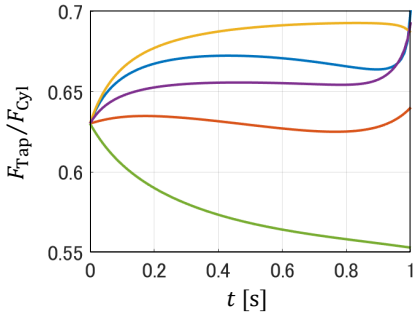

(c) $F_{0\mathrm{R}}$

Figure 4.31: Ratio of F_{Tap} to F_{Cyl} in each piston

base chain, the ratio is less than 70 %, and through the motion, it becomes 60 to 65 % in some configurations. It means that with the given tapered shape, the force transmission efficiency was improved more than the mass reduction (71 %).

4.5 Summary

In this chapter, the design of a novel rigid extendable arm was introduced, which has multiple DOF, while improving the configuration variation of the original origami structure by removing the part at which undesired deformations occur. In addition, to improve the static performance of the extendable arm inspired by Origami Spring, the modification of its folding diagram to give the extendable arm a taper was introduced.

1. The design process of the novel extendable mechanism was demonstrated, and the prototype was fabricated using rigid components. The novel extendable mechanism was proven to be a sophisticated and suitable mechanism that can be implemented in extendable arms.

2. By removing the components which limit the workspace of the mechanism, various configurations, including a configuration with a large curvature, were achieved without deformation of components.

3. Effective actuation was introduced by devising the wire drive with consideration to the characteristics of mechanism.

4. The folding diagram based improvement is valid for the design of the mechanism, and the effect on its static performance was verified by the motion experiments and the quasi-static analysis.

Chapter 5

Application to an Assistive Devise for Fall Prevention

Looking ahead to develop an assistive device for fall prevention, a feasibility study of an origami-inspired extendable mechanism for this application is demonstrated while focusing on the implementation of rapid extension and high load capacity. At first, the specification of the device is determined referring to related studies and based on a simplified fall simulation. Through the observation and kinematic analysis of the motion of Origami Spring, it is found that there is the difference in the velocity ratio of output to input depending on where Origami Spring is actuated. This feature is exploited to implement the functional requirement in each phase: rapid extension from contracted configuration and high load capacity after the mechanism is fully extended. Each example of actuation is studied experimentally, and the problems to be solved are clarified.

5.1 Specification of the Device

As mentioned in Chapter 1, the target users of the proposed assistive device (Fig. 1.6) are older people who are over 65 years old. The data of target users' height and weight were based on the statistical data of Japan [61]. By taking the average and standard deviation of older people, the target user's weight was determined as 40 to 75 kg.

About load capacity, a fracture experiment of femur [62] was referred, and the failure force was 1.2 to 6.5 kN with bones of 62 to 84 years old subjects. When a femur is surrounded by tissues, larger force could be born. In this thesis, target load capacity was as 1.2 kN by taking the minimum value to prevent a fracture.

To determine shock reduction ratio, it needs to be considered that the magnitude of force when a human body contacts with the ground after a fall. Based on a simulation of contact force with a fall [63], it became 25 to 50 kN with 2.75 m/s walking speed. In addition to this, a simplified fall simulation was performed with the GIM® software [60] about a fall during walking. The fall postures in the simulation were based on [52] which divided fall postures into two types: hip-grounding fall and knee-grounding fall. These two fall postures were simplified as inverted pendulums as shown in Figs. 5.1 and 5.2 assuming a stumbling fall. The mass and height of the inverted pendulums were based on the older men's statistics data and study of COG [64] as shown in Table 5.1, and the initial velocity was based on the healthy walking speed of older people [58]. In this simulation, an additional situation was considered based on the lean angle 24° from where older people can recover their balance [65]. In Table 5.1, time and velocity are shown when the pendulum contacts with the ground from hip or knee. t_{end} and v_{end} show the values when hip or knee contact with ground. Here, the impulse-momentum theorem was considered with 10 ms time interval which is taken from [63], and the contact forces are revealed

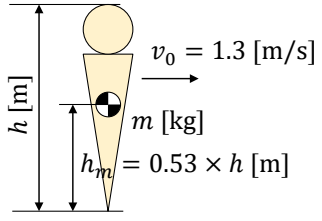

Figure 5.1: Definition of parameters for the simulation

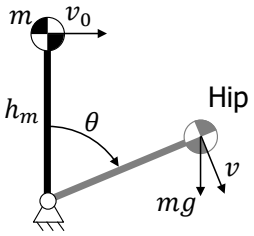

(a) Hip-grounding fall

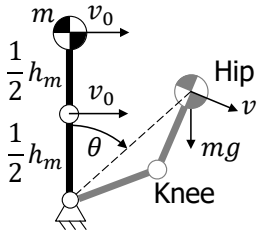

(b) Knee-grounding fall

Figure 5.2: Inverted pendulum models for the simulation

Table 5.1: Result of the simplified fall simulation

Type	h [m]	m [kg]	t_{end} [s]	v_{end} [m/s]	$t_{\theta=24^\circ}$ [s]	$v_{\theta=24^\circ}$ [m/s]
Hip	1.6	63	0.60	4.1	0.25	1.7
Knee			0.32	3.1	0.22	2.3

to be 26 kN with hip-grounding fall and 20 kN with knee-grounding. This result is consistent by comparing with the result in [63]. Therefore, 26 kN contact force needs to be reduced to 1.2 kN which is the minimum failure force and 95 % reduction by shock absorption.

To determine the extension time at the situation of a fall, the result of the simplified fall simulation was referred again. In Table 5.1, $t_{\theta=24^\circ} = 0.22$ s with the knee-grounding fall and this is the minimum time where older people can recover their balance by themselves [65]. To support the user's standing posture, the extension time should be shorter than 0.22 s at least when the fall detection time is assumed as 0 s. Therefore, the extension time was determined as 0.22 s as the first target. Referring to the wearable airbag products, Hip'Safe inflates in 80 ms at the side of hip joints [50]. The wearable airbags for a fall on bicycle [66] and motorcycle [67] can be also referred, and they inflate in about 100 to 250 ms.

As for the fall detection, it will be considered in the future work referring to the fall detection studies [68–70].

Other parameters, such as mass and dimensions of the assist device, were determined referring to specifications of other products [50,66,67] and assuming that the assist device fully extends at the maximum lean angle [65] as shown in Fig. 5.3.

The target specifications of the assist device to prevent serious injury with a fall are summarized in Table 5.2 except the detection time. Among the target specifications of the assistive device, extension time and load capacity were focused on in this thesis as the primary requirements as mentioned in subsection 1.1.2.

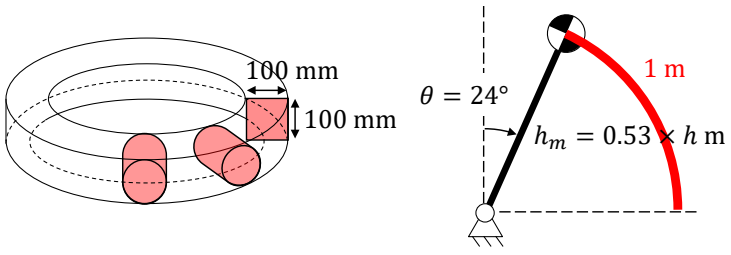

Figure 5.3: Dimension of the proposed assist device

Table 5.2: Target specifications of the assistive device

Functional requirement	Specification	
Rapid extension	Extension time	220 ms
High load capacity	User's weight	40-70 kg
	Load capacity	1.2 kN
Shock absorption	Shock reduction	95 %
High portability	Mass	1 kg
	Dimension in stored	100 × 100 mm
	Max. extended length	1 m
	Extension ratio	10
Fall detection	Detection time	-

5.2 Idea for Implement Rapid Extension and High Load Capacity

5.2.1 Difference of velocity ratio of output to input depending on where the mechanism is actuated

Based on the author experience playing with Origami Spring, the change of distance between each longitudinal side is small with its extension motion. As mentioned in chapter 3, many longitudinal sides contact with each other at the contraction limit configuration, and their distance become wider during the extension motion. On the other hand, the change of distance between certain lateral sides is large because there is the coiling during the extension motion, and Origami Spring can support some external load easily by keeping this distance, which is applied along the extension direction. Getting an idea from these behavior, the difference of velocity ratio of output to input depending on where the mechanism is actuated was investigated.

The change of distance between each longitudinal side l_i, which was defined in subsection 3.2.1 and Fig 3.11, is shown in Fig 5.4 during the 1 DOF extension motion along the configuration line of the zero thickness model (Fig. 3.19(a)) with the kinematic model in chapter 3. The length of longitudinal side a was 140 mm as same as in chapter 4. To describe the extension motion of the kinematic model, θ_1 was used as the representative input. Among them, the distance l_6 between 6^{th} and 7^{th} longitudinal sides was chosen as an example of input. As another input, the

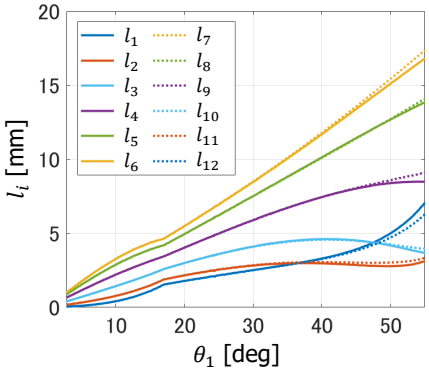

Figure 5.4: Change of the distance between each longitudinal side l_i during 1 DOF extension of the zero thickness model

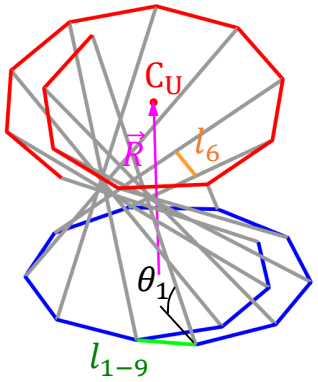

Figure 5.5: Two inputs l_6 and l_{1-9}, and output point C_U

distance l_{1-9} between 1^{st} and 9^{th} lateral sides' edges was used because the lateral sides which are outside of the spiral shape make a nonagon at the extension limit. The end point of the relative position vector $\overrightarrow{R}$ which was determined in subsection 3.2.3, which was called as C_U in subsection 4.2.1, was used as the output point. These are summarised in Fig. 5.5.

To compare the velocity ratio of output to input of the two types, the derivatives of l_6, l_{1-9}, and C_U with respect to θ_1 are approximated as rates of change of them to θ_1, and the velocity ratios of output to input are described as Eqs. (5.1) and (5.2) and the result of calculation is shown in Fig. 5.6.

$$\frac{v_{C_U}}{v_{l_6}} = \frac{\frac{dC_U}{d\theta_1}}{\frac{dl_6}{d\theta_1}} \tag{5.1}$$

$$\frac{v_{C_U}}{v_{l_{1-9}}} = \frac{\frac{dC_U}{d\theta_1}}{\frac{dl_{1-9}}{d\theta_1}} \tag{5.2}$$

As shown in Fig. 5.6, when the distance l_6 between 6^{th} and 7^{th} longitudinal sides is chosen as the input, the velocity ratio $\frac{v_{C_U}}{v_{l_6}}$ is always bigger than 1 and large near the contraction limit. On the other hand, when the distance l_{1-9} between 1^{st} and

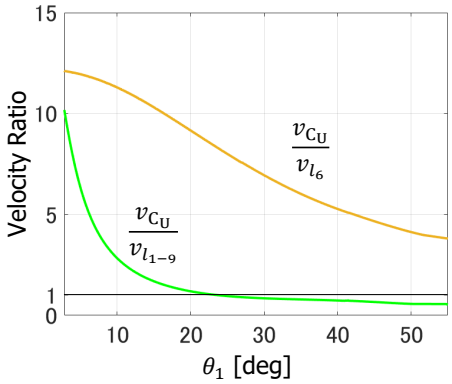

Figure 5.6: Velocity ratios of inputs l_6 and l_{1-9} to output during 1 DOF extension of the zero thickness model

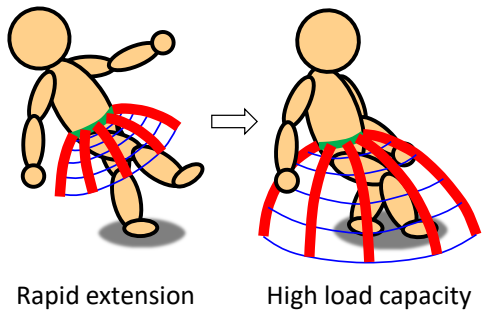

Figure 5.7: Functional requirements in each phase of the storyboard

9^{th} lateral sides' edges is chosen as the input, the velocity ratio $\frac{v_{C_U}}{v_{l_{1-9}}}$ becomes 0.5 to 0.8 after extension. Here, the velocity ratio of output to input is equal to the force ratio of input to output and it means that an external force applied to the output point can be supported by a small input force in l_{1-9}. Therefore, the input l_6 is suitable to implement a rapid extension from the contracted configuration and the input l_{1-9} is suitable to implement a high load capacity after extension.

Here, let's look back the functional requirements in each phase of the storyboard. As shown in Fig. 5.7, rapid extension and high load capacity are not needed to be displayed at the same time. In detail, rapid extension is needed after fall detection and during the extension motion, then the force which related the mechanism's mass is only applied to the mechanism. High load capacity is needed after the mechanism is fully extended. Therefore, the input l_6 can be used for rapid extension and l_{1-9} can be used for high load capacity respectively by keeping its distance. The two inputs are switched to display two functional requirements in one mechanism, and this is the key idea of this chapter. For rapid extension, the distance between other vertices will be considered as input and the velocity ratio will be calculated in the future work.

5.2.2 Suitable inputs set to actuate the distances between longitudinal sides

To decide which distances l_i between longitudinal sides should be actuated to extend the mechanism, suitable inputs set were selected with consideration to inputs' independence, singularity, and direction of actuation force. The prototype of the extendable mechanism is shown in Fig. 5.8 and the dimensions are the same in chapter 4, $a = 140$ mm, $b = 37.5$ mm, $n = 12$, and $d = 3$ mm. In this prototype, the hypotenuse was removed as same in chapter 4, but the offset of longitudinal side was not introduced. For this application, the compliant component as the hypotenuse and the offset of longitudinal side in the opposite direction in chapter 4 could be installed to limit the motion range and achieve a desired extension motion in the future work. This mechanism was modelled by the same way in subsection 4.1.2 and the chains of cylindrical joints were added as the actuators, as shown in Fig. 5.9, to change the distances between longitudinal sides based on the following assumptions: l_i is the length of normal line between two longitudinal sides, the foots of the normal

Figure 5.8: Unfolded prototype

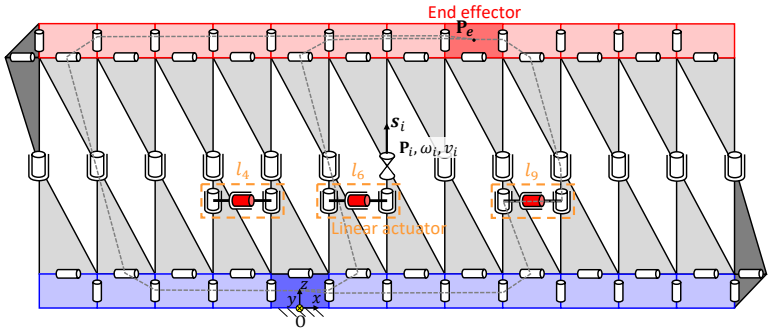

Figure 5.9: Kinematic model of the extendable mechanism. The actuators to extend l_i are modelled as a C-C-C kinematic chain and the active joints are shown in red.

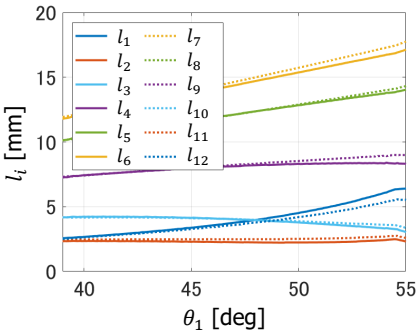

Figure 5.10: Change of the distance between each longitudinal side l_i during 1 DOF extension of the wood-stick model

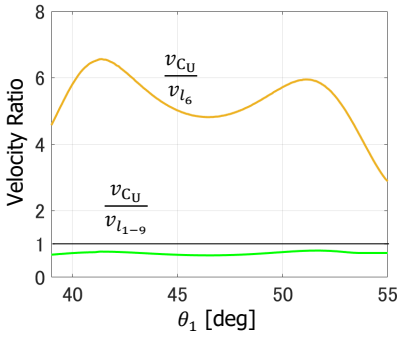

Figure 5.11: Velocity ratios of inputs l_6 and l_{1-9} to output during 1 DOF extension of the wood-stick model

line slide along the longitudinal side during the extension. In the C-C-C kinematic chain, only the translational motion of the cylindrical joint in the middle is active. As an example, l_4, l_6, and l_9 are actuated in Fig. 5.9. With the condition of $a = 140$ and $d = 3$ mm, there is no set of the variable values θ_1, θ_2 and θ_3 which satisfies the restraint conditions in subsection 3.2.1, but the prototype can extend and contract. This gap might be due to the joint clearance and the deformation of components. Therefore, the configuration line of the wood-stick model (Fig. 3.19(c), $a = 140$, $d = 2.5$ mm) was used in the following analyses and the change of distance between each longitudinal side l_i and the velocity ratios of output to input are shown in Figs. 5.10 and 5.11.

First, the inputs' independence were investigated using the loop closure equation as same in subsection 4.1.2 and 4.3.1. There are 51 revolute joints, 21 cylindrical joints and 16 kinematic chains, some of them are indicated by the gray lines in Fig. 4.4, that connect the stationary link and the end effector. The 16 equations for the velocity of the end effector are written as follows:

$$\begin{bmatrix} \mathbf{s}_i \\ \overrightarrow{\mathbf{P}_i\mathbf{P}_e} \times \mathbf{s}_i \end{bmatrix} \omega_i + \cdots + \begin{bmatrix} 0 \\ \mathbf{s}_i \end{bmatrix} v_i + \cdots = \mathbf{V}_{\mathbf{P_e}} \tag{5.3}$$

where $\mathbf{P}_i$ is the position of each joint, $\mathbf{P}_e$ is the reference point of the end effector, $\mathbf{s}_i$ is the unit vector along the axis of each joint, ω_i is the angular velocity of each joint, v_i is the translational velocity of each joint along $\mathbf{s}_i$, and $\mathbf{V}_{\mathbf{P_e}} = [\omega; v]$ is the

velocity of the end effector. Based on these equations, 15 loop closure equations with six dimensions can be derived by eliminating $\mathbf{V_{P_e}}$ (i.e., 90 scalar equations). By combining them, the following equation is obtained:

$$\mathbf{A}\left[\omega_1 \ \cdots \ \omega_{72} \ v_1 \ \cdots \ v_{21}\right]^T = \mathbf{0} \tag{5.4}$$

where $\mathbf{A}$ is the 90×93 coefficient matrix. To check the inputs' independence, Eq. (5.4) is transformed as the following equation:

$$\mathbf{A}_\mathrm{a} v_\mathrm{a} + \mathbf{A}_\mathrm{p} \omega_\mathrm{p} = \mathbf{0} \tag{5.5}$$

where v_a is the 3×1 vector with translational velocities of three cylindrical joints which are red in Fig. 5.9, ω_p is the 90×1 vector with 72 angular velocities of all joints and 18 translational velocities of the passive joints, $\mathbf{A}_\mathrm{a}$ is the 90×3 coefficient matrix, and $\mathbf{A}_\mathrm{p}$ is the 90×90 coefficient matrix. The matrix $\mathbf{A}$ in Eq. (5.4) is divided into $\mathbf{A}_\mathrm{a}$ and $\mathbf{A}_\mathrm{p}$ according to distinction of joints between active and passive. When the translational velocities of three cylindrical joints are independent, $\dim(\mathrm{Ker}\mathbf{A}_\mathrm{p})$ is 0. All combinations to pick up three distances from 12 distances (${}_{12}C_3 = 220$) were investigated. Among 220 combinations of three distances, eight combinations are independent. In this calculation, the singularity of configuration was also checked. There is no singular configuration with eight independent inputs sets.

In addition, the direction of the actuation force was considered. It is assumed that the actuator can generate only the forces in the direction to extend the distances between the longitudinal sides. The static analysis was carried out to check the direction of the actuation force with each configuration during 1 DOF extension assuming that an external force is applied at the point $\mathbf{P}_e$ in the contraction direction of the mechanism. Among eight combinations of three distances between longitudinal sides, the actuation forces are always in the direction to extend the distances with only two combinations: (l_4, l_6, l_9) and (l_4, l_7, l_9).

Finally, the suitable inputs sets to actuate the extendable mechanism were revealed as the distances between the longitudinal sides (l_4, l_6, l_9) and (l_4, l_7, l_9). They are symmetric with respect to the mechanism and (l_4, l_6, l_9) was used in this thesis.

5.2.3 Examples of actuation methods

To give the two inputs to the mechanism as discussed, two actuation methods were introduced.

For actuation of the distances between longitudinal sides, there is a restraint that the initial distance at the contraction limit is almost zero, then the actuator needs to change its width from thin to thick. Therefore, airbags were chosen as an example in this thesis to actuate the distances between longitudinal sides. At the extension limit of the mechanism, the the distances l_4, l_6, and l_9 become $l_4 = 8, l_6 = 17$, and $l_9 = 9$ mm. To obtain these distances, two types of airbags were designed as 1 mm larger than the target distance and fabricated with PVC as shown in Fig. 5.12. The longitudinal shaft passes through the center hole of the airbag. The desired distance can be obtained by inflating two adjacent airbags as shown in Fig. 5.8.

To keep the distances l_{1-9} after the extension of the mechanism, a lock element is needed. A lock element should not disturb the smooth extension motion and lock distance l_{1-9} when the mechanism nearly moves to be contracted by an external force. A ratchet, especially a zip tie, was considered as an option and it was attached to the mechanism as shown in Fig. 5.13. At the extension limit, only one set of θ_1, θ_2 and θ_3 in Fig. 3.12, then two zip ties were enough to hold the configuration. In the future work, the teeth of zip tie will be removed to make a friction lower except where the zip tie needs to be locked after extension.

The extendable mechanism is shown in Fig. 5.13 which has the airbags to actuate the distances between longitudinal sides and the zip ties to lock the distance between certain lateral sides and hold the configuration after the extension.

Figure 5.12: Two types of airbags made by PVC

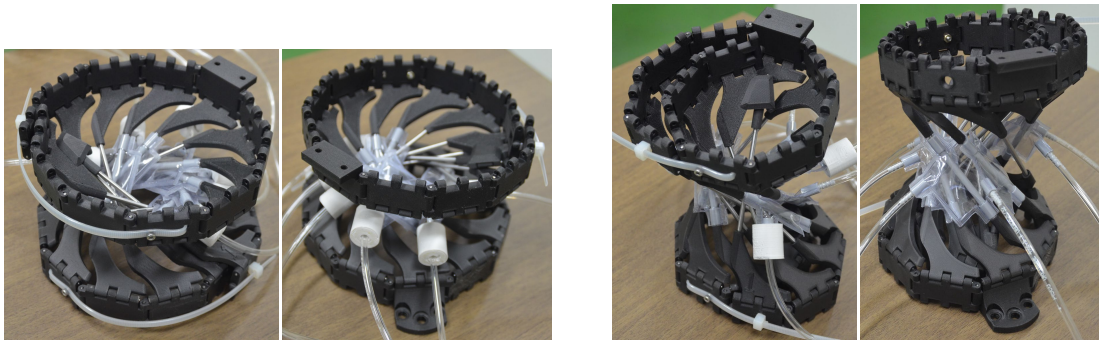

(a) Contracted (b) Extended

Figure 5.13: Prototype which has the airbags for extension and the zip ties to hold the extended configuration

5.3 Experimental Study with the Early Prototype

Two experiments were carried out to verify the feasibility of the actuation strategy to implement rapid extension and high load capacity

5.3.1 Rapid extension by airbag

This experiment was carried out to verify that the extendable mechanism can be extended with the airbags, and to check the extension time.

The experimental set up is shown in Fig. 5.14. The 6-axis force sensor (TL6F04-5KN, Tec Gihan Co., Ltd) was attached to the prototype to measure the force and moment which is applied to the attached part of user's body. The 6-axis force sensor was fixed to the frame and the airbags were connected to the air compressor (ACP-10A, EARTH MAN) whose volume is 10L. The airbags were inflated when the switch was pressed. The accelerometer (3DM-GX5-25, LORD) was attached to the plate which was connected to the end effector in Fig. 5.9. The axes of the 6-axis force sensor and the accelerometer are shown in Fig. 5.14. With this experimental setup, the extension motion was tested. The extension motion by airbags is shown in Fig. 5.15, and it can be said that the extendable mechanism inspired by Origami Spring extends with the selected arrangement of airbags.

The example of time change of acceleration $\ddot{\zeta}$ during the extension motion is shown in Fig. 5.16. Acceleration $\ddot{\zeta}$ includes the acceleration of gravity. There are

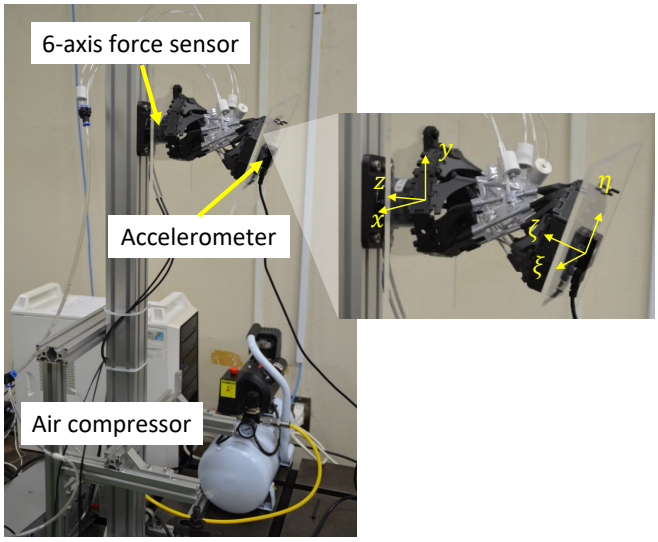

Figure 5.14: Experimental setup for extension

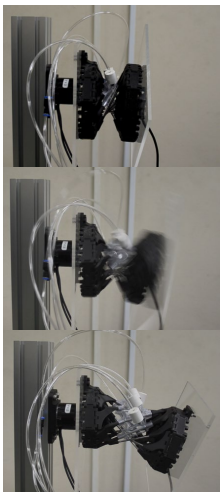

Figure 5.15: Extension motion by airbags

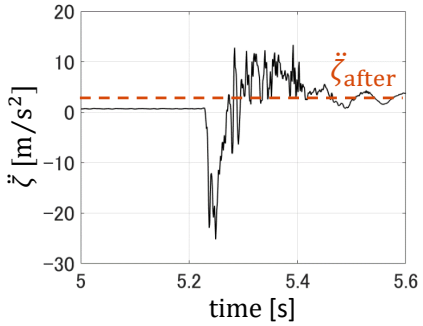

Figure 5.16: Example of change of acceleration $\ddot{\zeta}$ during the extension motion. Acceleration $\ddot{\zeta}$ includes the acceleration of gravity and ζ_{after} is the steady state after extension.

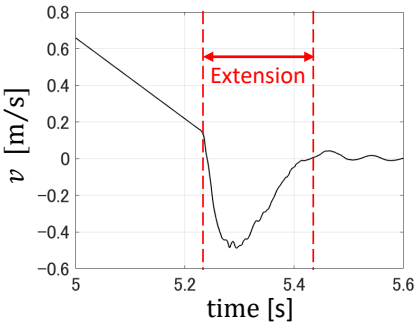

Figure 5.17: Example of time change of velocity during the extension motion. The steady state of velocity after extension is set as 0. The end of extension is when v becomes 0 after the extension.

two steady states before and after extension because the configuration of prototype is changed. To determine the extension period, the time change of velocity during the extension was calculated from the measured acceleration $\ddot{\zeta}$ while removing the effect of the acceleration of gravity by subtracting the value of the steady state after extension ζ_{after} from $\ddot{\zeta}$. The result of calculation is shown in Fig. 5.17 where the steady state of velocity after extension is set as 0. The time when v becomes 0 after the extension was regarded as the end of extension. The average of the extension time with 10 times extension experiments was 217 ms when the airbags were in-

flated with 0.6 MPa in the pressure gauge of air compressor. It was found that the extension time is shorter than the target specification 220 ms. This extension time will change depending on the air supply, the number of the extendable mechanisms and segments, and the material of the airbags. For the wearable airbag products such as [50, 66, 67], a CO_2 cylinder is often used and the pressure is lower than the air compressor. When the number of the extendable mechanisms and segments is increased to develop the assist device as shown in Fig. 5.7, the sum of the volume of airbags is increased and more air is needed. As for the material of airbag, PVC is used in this experiment for its durability but it is not much soft and its flexibility depends on the room temperature (this experiment was done in Dec. and Jan.). For this reason, the pressure which needs to inflate the PVC airbags is as high as 0.6 MPa comparing to the airbags made by a polyethylene sheet (Fig. 5.18) which needs 0.14 MPa to be inflated but is too weak to do experiment several times. The suitable material would be nylon which is used for the airbag of a car and a parachute. Based on these three points, a further experiment will be done in the future.

As for the force and moment which are applied to the attached part, the examples of time changes of force F_z and moment M_y during the extension motion are shown in Fig. 5.19. The forces and moments in other axes were almost zero. The averages of maximum values of $|F_z|$ and $|M_y|$ with 10 times extension experiments were $|F_z| = 2.301$ N and $|M_y| = 0.129$ Nm with 485 g mass of the prototype. The force and moment will become larger when more segments are connected.

Figure 5.18: Airbag made by polyethylene sheet

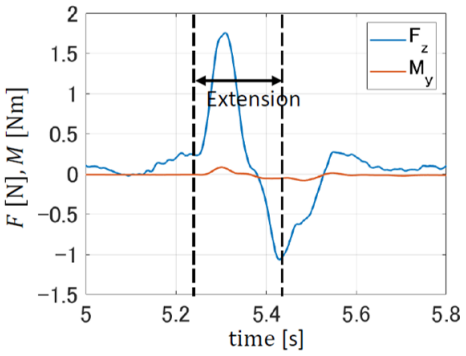

Figure 5.19: Example of time change of force F_z and moment M_y during the extension motion

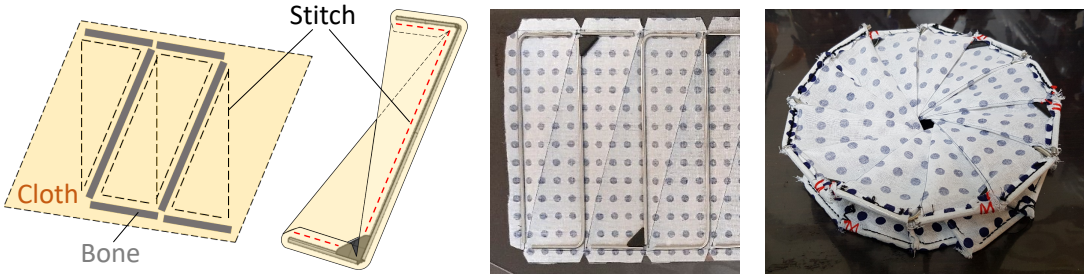

Figure 5.20: An idea to improve the extension ratio. The bones of structure are covered with cloth to hold the bones

The extension ratio of one segment is only 1.6 (98 mm to 157 mm), and 8 segments are needed to satisfy the dimension of the device but its extension ratio is 1.7 (609 mm to 1025 mm) with this design. The purpose of this experiment is to verify that the desired extension motion can be done with the airbags, then the prototype was made to have the kinematic characteristics of the mechanism and became massive and bulky. The main reason why the extension ratio is low is that the lateral sides have a width to make hinges compare to the original Origami Spring. To improve the extension ratio, the mechanism can consist of bones of the structure and a material like a cloth which covers and holds the bones as shown in Fig. 5.20. The offset of the longitudinal side in chapter 4 can be also applied to achieve more contracted configuration. In addition, an elastic material can be used for some of the longitudinal sides in the mechanism for the same purpose of the offset, and it would add the shock absorption to the mechanism.

5.3.2 Relation between impact force and tensile force in lock element

This experiment was carried out to verify that the impact force which is applied to the mechanism when the mechanism contacts with the ground can be supported as the tensile forces in zip ties which keep the distance and hold the extended configuration. For this purpose, the relation between the impact and tensile forces was investigated. With this experiment, the magnitude of tensile force when the impact force in a fall is applied can be assumed and it will be used as the required load capacity of the lock element.

The experimental set up is shown in Fig. 5.21. The same 6-axis force sensor in

previous experiments was attached between the prototype and the frame to measure the impact force in a fall. The two 3-axis force sensors (USL08-H6-2KN, Tec Gihan Co., Ltd) were attached between 1^{st} and 9^{th} lateral sides of the lower and upper lateral chains, and the prototype was held in the fully extended configuration. The two 3-axis force sensors measured the tensile force between 1^{st} and 9^{th} lateral sides when the impact force was applied. The axes of force sensors are shown in Fig. 5.21 The frame, which the prototype was attached to, was the inverted pendulum and it fell down to the ground from the angles shown in Fig. 5.21. In each angle, the forces were measured 10 times.

The examples of time changes of the impact and tensile forces are shown in Fig. 5.22 where the value of forces after fall is set as 0. The impact force applied to the mechanism is $F_{\mathrm{impact,z}}$ and the tensile forces between 1^{st} and 9^{th} lateral sides are the negative force of $F_{1,z}$ and $F_{2,z}$. There are two peaks in Fig. 5.22 because the prototype bounded once after the first contact with ground. The values of first peak are gathered in Fig. 5.23. The approximated straight lines were derived by the least squares method. From this result, it can be assumed that the required load capacity of the lock element is about 300 N when the 1.2 kN impact force is applied. 300 N tensile strength can be provided with commercial zip ties. This relation between the impact and tensile forces will change depending on the material of the mechanism's components, the joint clearance, and the material of a floor. As

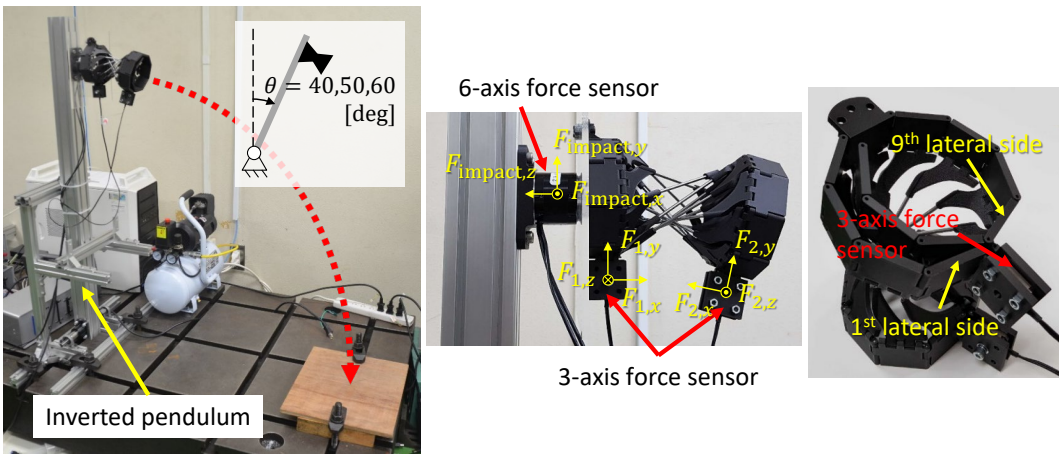

Figure 5.21: Experimental setup for impact force

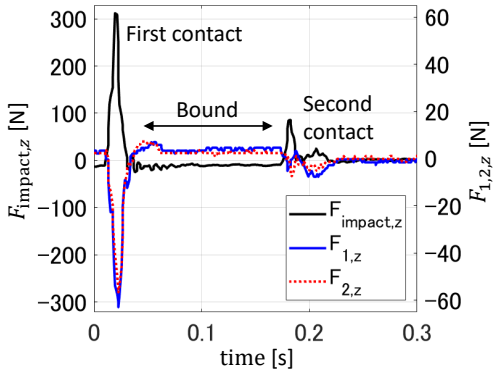

Figure 5.22: Example of time changes of the impact and tensile forces. There are two peaks because the prototype bounded once after the first contact with ground

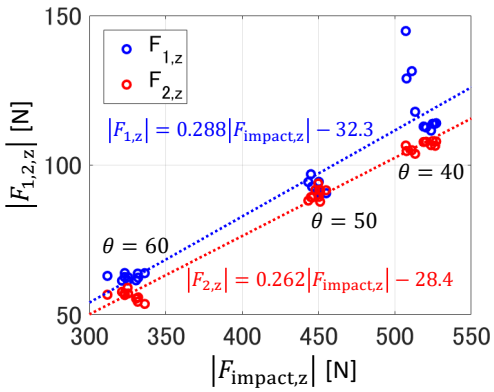

Figure 5.23: Relation between the impact and tensile forces

the first step, the material of a floor will be changed as a carpet, a wood, a tile, a tatami, and asphalt, and the change of the relation between the impact and tensile forces should be checked in the future work.

To verify the result of the experimental studies, the kinetic and static analyses should be carried out in the future work about the force which the airbags need to exert for extension, the force and the moment which are applied to the attached part of user's body by the extension motion, and the tensile forces in the lock elements which hold the extended configuration.

5.4 Summary

In this chapter, a feasibility study of the origami-inspired extendable mechanism for the fall prevention assistive device was studied. The idea was proposed and verified through the experimental study where multiple actuation methods were used in one mechanism corresponding to each functional requirement: rapid extension and high load capacity, by focusing on the difference in the velocity ratio of output to input depending on where the mechanism is actuated.

1. It was revealed that the actuation of the distance between the longitudinal sides is appropriate for rapid extension and the actuation of the distance between the certain lateral sides is appropriate for high load capacity in the extendable

mechanism inspired by Origami Spring from the perspective of the velocity ratio of output to input.

2. The suitable arrangement of airbags to actuate the distance between the longitudinal sides was clarified by the kinematic analyses and it was verified experimentally that the actuation of the distance between longitudinal sides by airbag is effective to implement a rapid extension.

3. Effectiveness of supporting an external impact force as tensile forces between certain lateral sides by lock elements was verified experimentally.

Chapter 6

Conclusions and Future Work

6.1 Conclusions

In this thesis, a soft-deployable origami structure, Origami Spring, was selected as a base structure of extendable mechanisms. The objective of this research was to reveal the kineto-elasto-static characteristics of Origami Spring by modelling it with rigid and compliant components and revolute joints to consider the collision and deformation of components. Based on the revealed characteristics, to propose design strategies of extendable mechanisms inspired by a deployable origami beyond the characteristics of the original origami through the design of extendable mechanisms for two applications, their kinematic analyses and experimental studies was also the objective of this research.

To enable applications of Origami Spring to extendable mechanisms, a kinematic model of Origami Spring with combination of rigid and compliant components was proposed by identifying the component which must deform, and characteristics of Origami Spring's extension have been revealed with the proposed model considering the collision between rigid components. In addition, the effect of compliant components' deformation on the configuration of Origami Spring has been investigated.

Looking ahead to application to an extendable arm working in a narrow space, to maximize the performance of extendable mechanism inspired by Origami Spring for large extension ratio, sufficient load capacity, and generation of large curvature shape, the deformation of components was removed and the collision between com-

ponents was reduced, which give a large effect to constrain its motion as revealed in the kineto-elasto-static analysis of Origami Spring. Through these improvements, the extendable arm was designed and its basic motion has been verified through the displacement analysis and motion experiment.

Looking ahead to application to an assistive device for fall prevention, the actuation strategy of the extendable mechanism inspired by Origami Spring to achieve rapid extension and high load capacity in one mechanism was proposed focusing on the difference of the velocity ratio of output to input depending on where the mechanism is actuated. Through the experimental studies with prototype, the feasibility of this strategy has been verified experimentally.

The conclusions obtained are summarized as follows.

1. It has been enabled to explain the real behavior of a deployable origami by kineto-elasto-static analysis with its kinematic model which can reflect the deformation of components and the restraint conditions about the collision of components based on the observation of a deployable origami.

2. An extendable mechanism has been enabled to be achieved inspired by a soft-deployable origami structure with only rigid components by removing the deformed components from the original structure while keeping its kinematic equivalence.

3. It has been enabled to implement high transformability, including a configuration with a large curvature, to an extendable mechanism inspired by a soft-deployable origami structure even though it consists of only rigid components by reducing the collision of components and expanding the workspace of the extendable mechanism.

4. An idea to achieve both rapid extension and high load capacity has been proposed and verified experimentally, where the multiple actuation strategies are applied in one mechanism by focusing on the difference in the velocity ratio of output to input depending on where the mechanism is actuated.

Based on this thesis work, the features of the proposed mechanisms in this thesis and conventional extendable devices are summarized in Table 6.1. The advantage of

Table 6.1: Summary of extendable devices

	DOF (m segment)	Generated shape	Load capacity	Extension speed
Proposed mechanism for extendable arm	$m+2$	Largely Curved S-shape	Good	-
Proposed mechanism for assistive device	1	Curved (Designable)	Good	Excellent
Spiralift [30]	1	Linear	Excellent	Poor
Zip chain actuator [32]	1	Linear	Excellent	Good
Triple Scissor Extender [40]	$m \times 3$	Curved S-shape	Good	-
Deployable Soft Arm [7]	3	Largely Curved	Poor	-

the proposed mechanism for extendable arm is the large curvature shape generated by rigid components. The advantage of the proposed mechanism for assistive device is rapid generation of the curved shape. By applying appropriate ideas and methods selectively depending on the requirements, desired extendable mechanisms inspired by Origami Spring can be achieved.

The contribution of this thesis is that characterization of a soft-deployable origami which includes collision and deformation of components in its structure has been enabled by modelling it with combination of rigid and compliant components, and analyzing the model kinematically. The key point is the identification of the components which are modelled as compliant components. In this thesis, the deformation of components has been identified based on the observation of the subject and the simplified geometrical structure. This strategy can be applied to other soft-deployable origami. After the identification, the kinematic characteristic of a subject can be revealed with the modelled rigid mechanism, focusing on the collision between rigid components. In addition, the real behavior of a subject can be explained by considering the effect of the deformation of components which are modelled as compliant components. Based on the revealed characteristics of a subject, novel extendable mechanisms are enabled to be proposed which are beyond the features of the original origami structure by removing or reducing the effect of components' collision and deformation.

In addition, the idea switching multiple actuations in one mechanism to achieve

multiple functions based on the difference of the velocity ratio of output to input depending on where the mechanism is actuated is a new approach to implement rapid motion and high power generation in one mechanism. This idea can be applied to any mechanism as long as there is the difference of the velocity ratio of output to input depending on where the mechanism is actuated.

6.2 Future Work

6.2.1 Outlook for the future

The kinematic and mechanical characteristics of a soft-deployable origami structure have been enabled to be revealed based on the contribution of this thesis. In addition, the design of new extendable mechanisms which are beyond the limit of conventional deployable origami structures and the features of the original origami structure has been enabled based on the revealed characteristics of soft-deployable origami. The process to apply a soft-deployable origami to mechanism was built by this research. In this research, Origami Spring was selected as the subject because of its unique features. When a better origami structure is found, it can be applied to a mechanism by using the process which this thesis demonstrated, and new mechanism will be developed.

6.2.2 Remaining problems of each application

A) Extendable Arm for Working in a Narrow Space

As discussed in chapter 4, the actuation of the extendable arm has some problems. About the method of actuating the base lateral chain, the base lateral chain cannot be completely closed because of the path of the wire. This insufficiency leads to the displacement discrepancy. To address this issue, an additional wire having the same path as the upper lateral chain can be introduced as a possible solution. In addition, the configuration of the lateral chain is kept by the tension of the wire and the counter force of the leaf spring, but this actuation cannot deal with an external force which is applied to close the lateral chain. To develop the proposed extendable arm (Fig. 1.5) which performs heavy labor by exploiting the

contact forces with narrow spaces, the actuation method for the contraction motion needs to be reconsidered.

For the real use of this extendable arm, the strategy to control its configuration along a target narrow space needs to be considered. A target narrow space can be described with the length between each inflection point and the bending angle at inflection points. Based on these information, the configuration of the extendable arm needs to be decided. The configuration of each segment is dependent on the configurations of next segments. To generate a desired configuration along a target narrow space, the table which was created in subsection 4.2.2 is not sufficient, and the posture, the extension length, the tilting angle and the tilting direction of each configuration need to be added to the table. A system needs to be developed to show the possible configuration of each segment when the configuration of one segment is decided, using the table.

About the configuration of the extendable arm, there was a position discrepancy when the configuration of the prototype was compared with the configuration derived by the displacement analysis. The discrepancy is attributed to the joint clearance, the deformation of components, and the difference of the posture of the longitudinal side, which was given an offset and rotates with idle revolute joints, between the prototype and the displacement analysis. The discrepancy between the prototype and the displacement analysis will be decreased by reflecting the rotation of the longitudinal side in the displacement analysis with the collision between other longitudinal sides.

B) Assistive Devise for Fall Prevention

The further experiment need to be carried out while changing the condition of the prototype. In the extension experiment, the air supply, the number of the segments, extendable mechanisms and airbags, the material of the airbags need to be changed. Instead of the air compressor, a CO_2 cylinder will be used and the effect of the difference of air flow channel will be investigated. The number of the segments will be increased as shown in Fig. 6.1. This extendable mechanism can be extended theoretically by the airbags which are attached to the first segment, but

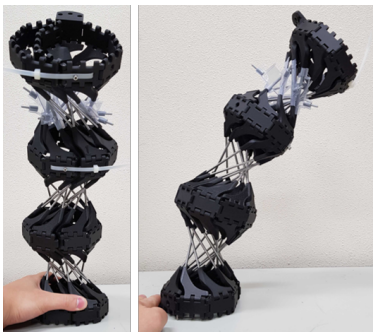

Figure 6.1: Prototype of the extendable mechanism which consists of 3 segments

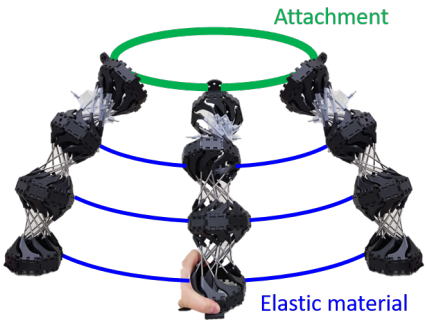

Figure 6.2: Extendable mechanisms placed in parallel following the concept in Fig. 1.6

the airbags can be added to other segments as same as the first segment. Following the concept (Fig. 1.6), the extendable mechanisms will be placed in parallel as shown in Fig. 6.2. With these changes, the sum of the volume of airbags will be increased and more air will be needed. The force and the moment which are applied to the attached part will be also larger because the prototype becomes heavier. As for the material of airbag, nylon will be an appropriate option, which is used for the airbag of a car and a parachute, and a airbag which can be inflated with low pressure will be fabricated. Based on these three points, a further experiment should be done. In the experiment with impact force, the place of the lock element, the material of a floor will be changed. When the number of the segments is increased (Fig. 6.1), the lock element can be attached to all or some lateral chains. The same experiment should be done while changing the place where the force sensors are attached. The material of a floor will be also changed as mentioned in subsection 5.3.2.

To verify the result of the experimental studies, the kinetic and static analyses should be carried out about the force which the airbags need to exert for extension, the force and the moment which are applied to the attached part of user's body by the extension motion, and the tensile forces in the lock elements which hold the extended configuration. In these analyses, the distance between other vertices would be considered as input and the velocity ratio would be calculated for rapid extension.

About the other functional requirements, there are some ideas. To implement high portability, the extension ratio of the extendable mechanism is important. As

idea to improve the extension ratio, the mechanism can consist of bones of the structure and a material like cloth which covers and holds the bones as shown in Fig. 5.20. The offset of the longitudinal side in chapter 4 can be also applied to achieve more contracted configuration or to limit its workspace for better extension motion. In addition, an elastic material can be used for some of the longitudinal sides in the mechanism and it would add the shock absorption to the mechanism. The shock absorption can be also implemented by adding the elastic material between the zip tie and the lateral side. The distance between certain lateral sides can be changed slightly while absorbing the impact force. As for the fall detection, it will be considered referring to the fall detection studies [68–70].

The idea to implement rapid extension and high load capacity, which uses multiple actuation methods in one mechanism corresponding to each functional requirement by focusing on the velocity ratio of input to output, can be applied to other deployable origami structures like [17] and extendable mechanisms like a scissor mechanism. These structure might be other options of the base structure.

Following the discussions above, the remaining problems of each applications would be addressed in the future work.

Bibliography

[1] D.-Y. Lee, J.-S. Kim, S.-R. Kim, J.-S. Koh, and K.-J. Cho, "The deformable wheel robot using magic-ball origami structure," in *ASME 2013 international design engineering technical conferences and computers and information in engineering conference*. American Society of Mechanical Engineers Digital Collection, 2013.

[2] C. D. Onal, R. J. Wood, and D. Rus, "An origami-inspired approach to worm robots," *IEEE/ASME Transactions on Mechatronics*, vol. 18, no. 2, pp. 430–438, 2012.

[3] K. Ikeya, H. Sakamoto, H. Nakanishi, H. Furuya, T. Tomura, R. Ide, R. Iijima, Y. Iwasaki, K. Ohno, K. Omoto, *et al.*, "Significance of 3u cubesat origamisat-1 for space demonstration of multifunctional deployable membrane," *Acta Astronautica*, 2020.

[4] R. V. Martinez, C. R. Fish, X. Chen, and G. M. Whitesides, "Elastomeric origami: programmable paper-elastomer composites as pneumatic actuators," *Advanced functional materials*, vol. 22, no. 7, pp. 1376–1384, 2012.

[5] J. Santoso, E. H. Skorina, M. Luo, R. Yan, and C. D. Onal, "Design and analysis of an origami continuum manipulation module with torsional strength," in *2017 IEEE/RSJ International Conference on Intelligent Robots and Systems (IROS)*. IEEE, 2017, pp. 2098–2104.

[6] D. Jeong and K. Lee, "Design and analysis of an origami-based three-finger manipulator," *Robotica*, vol. 36, no. 2, pp. 261–274, 2018.

[7] J. Fathi, O. V. T. JC, M. S. Runciman, and G. P. Mylonas, "A deployable soft robotic arm with stiffness modulation for assistive living applications," in *2019 International Conference on Robotics and Automation (ICRA)*. IEEE, 2019, pp. 1479–1485.

[8] K. Miura, "The science of miura-ori: A review," *Origami*, vol. 4, pp. 87–100, 2009.

[9] B. G. Winder, S. P. Magleby, and L. L. Howell, "Kinematic representations of pop-up paper mechanisms," *Journal of mechanisms and robotics*, vol. 1, no. 2, 2009.

[10] T. Tachi, "Rigid-foldable thick origami," *Origami*, vol. 5, pp. 253–264, 2011.

[11] J. Cai, Z. Qian, J. Feng, C. Jiang, and Y. Xu, "Mobility and kinematic paths of foldable origami structures," in *International Design Engineering Technical Conferences and Computers and Information in Engineering Conference*, vol. 50169. American Society of Mechanical Engineers, 2016, p. V05BT07A046.

[12] H. Feng, R. Peng, J. Ma, and Y. Chen, "Rigid foldability of generalized triangle twist origami pattern and its derived 6r linkages," *Journal of Mechanisms and Robotics*, vol. 10, no. 5, 2018.

[13] K. Zhang and J. S. Dai, "Classification of origami-enabled foldable linkages and emerging applications," in *International Design Engineering Technical Conferences and Computers and Information in Engineering Conference*, vol. 55942. American Society of Mechanical Engineers, 2013, p. V06BT07A024.

[14] S. Liu, W. Lv, Y. Chen, and G. Lu, "Deployable prismatic structures with origami patterns," in *International Design Engineering Technical Conferences and Computers and Information in Engineering Conference*, vol. 46377. American Society of Mechanical Engineers, 2014, p. V05BT08A037.

[15] B. J. Edmondson, R. J. Lang, S. P. Magleby, and L. L. Howell, "An offset panel technique for thick rigidly foldable origami," in *ASME 2014 International Design Engineering Technical Conferences and Computers and Information in*

Engineering Conference. American Society of Mechanical Engineers, 2014, pp. V05BT08A054–V05BT08A054.

[16] Y. Chen, R. Peng, and Z. You, "Origami of thick panels," *Science*, vol. 349, no. 6246, pp. 396–400, 2015.

[17] E. T. Filipov, T. Tachi, and G. H. Paulino, "Origami tubes assembled into stiff, yet reconfigurable structures and metamaterials," *Proceedings of the National Academy of Sciences*, vol. 112, no. 40, pp. 12 321–12 326, 2015.

[18] M. R. Morgan, R. J. Lang, S. P. Magleby, and L. L. Howell, "Towards developing product applications of thick origami using the offset panel technique," *Mechanical Sciences*, vol. 7, no. 1, pp. 69–77, 2016.

[19] C. H. Belke and J. Paik, "Mori: a modular origami robot," *IEEE/ASME Transactions on Mechatronics*, vol. 22, no. 5, pp. 2153–2164, 2017.

[20] S. Li, D. M. Vogt, D. Rus, and R. J. Wood, "Fluid-driven origami-inspired artificial muscles," *Proceedings of the National academy of Sciences*, vol. 114, no. 50, pp. 13 132–13 137, 2017.

[21] J. Cai, X. Deng, Y. Zhang, J. Feng, and Y. Zhou, "Folding behavior of a foldable prismatic mast with kresling origami pattern," *Journal of Mechanisms and Robotics*, vol. 8, no. 3, p. 031004, 2016.

[22] J.-E. Suh, T.-H. Kim, and J.-H. Han, "New folding concept on the cylindrical structure with yoshimura pattern: Folding pattern analysis," in *AIAA Scitech 2020 Forum*, 2020, p. 0210.

[23] H. Greenberg, M. L. Gong, S. P. Magleby, and L. L. Howell, "Identifying links between origami and compliant mechanisms," *Mechanical Sciences*, vol. 2, no. 2, pp. 217–225, 2011.

[24] K. Saito, A. Tsukahara, and Y. Okabe, "New deployable structures based on an elastic origami model," *Journal of mechanical design*, vol. 137, no. 2, 2015.

[25] C. M. Wheeler and M. L. Culpepper, "Soft origami: Classification, constraint, and actuation of highly compliant origami structures," *Journal of Mechanisms and Robotics*, vol. 8, no. 5, 2016.

[26] H. Sakamoto, M. Natori, S. Kadonishi, Y. Satou, Y. Shirasawa, N. Okuizumi, O. Mori, H. Furuya, and M. Okuma, "Folding patterns of planar gossamer space structures consisting of membranes and booms," *Acta Astronautica*, vol. 94, no. 1, pp. 34–41, 2014.

[27] J. Beynon, "Spring into action, bos magazine, vol. 142," *British Origami Society*, 1990.

[28] C. C. Min and H. Suzuki, "Geometrical properties of paper spring," in *Manufacturing Systems and Technologies for the New Frontier*. Springer, 2008, pp. 159–162.

[29] S. Yao, X. Liu, S. V. Georgakopoulos, and M. M. Tentzeris, "A novel reconfigurable origami spring antenna," in *2014 IEEE Antennas and Propagation Society International Symposium (APSURSI)*. IEEE, 2014, pp. 374–375.

[30] "Paco spiralift - automotive industrial lifting solutions," https://www.pacospiralift.com/ja/, Accessed:2020-11-30.

[31] F. Collins and M. Yim, "Design of a spherical robot arm with the spiral zipper prismatic joint," in *2016 IEEE international conference on robotics and automation (ICRA)*. IEEE, 2016, pp. 2137–2143.

[32] T. Etori, "Engagement chain and movable body movement device," May 21 2019, uS Patent 10,295,018.

[33] C. D. Woodruff and G. E. Woodruff, "Apparatus and methods for providing a retractable mast," Feb. 23 2016, uS Patent 9,267,640.

[34] I. Kawabuchi, W.-K. Yoon, and T. Kotoku, "Linear-motion telescopic mechanism and robot arm having linear-motion telescopic mechanism," Jan. 6 2015, uS Patent 8,925,405.

[35] W.-K. Yoon, "Extensible and retractable arm mechanism, and robot arm," June 26 2018, uS Patent 10,005,189.

[36] S. Teshigawara and H. Asada, "A mobile extendable robot arm: Singularity analysis and design," 2020.

[37] M. A. Robertson, O. C. Kara, and J. Paik, "Soft pneumatic actuator-driven origami-inspired modular robotic "pneumagami"," *The International Journal of Robotics Research*, p. 0278364920909905, 2020.

[38] K. Miura, H. Furuya, and K. Suzuki, "Variable geometry truss and its application to deployable truss and space crane arm," *Acta Astronautica*, vol. 12, no. 7-8, pp. 599–607, 1985.

[39] V. A. Sujan and S. Dubowsky, "Design of a lightweight hyper-redundant deployable binary manipulator," *J. Mech. Des.*, vol. 126, no. 1, pp. 29–39, 2004.

[40] A. Shikari and H. Asada, "Triple scissor extender robot arm: a solution to the last one foot problem of manipulation," *IEEE Robotics and Automation Letters*, vol. 3, no. 4, pp. 3975–3982, 2018.

[41] T. Yokota and N. Takesue, "Development of multi-dof robot arm by wire drive for portability," in *Proceedings of the 2020 JSME Conference on Robotics and Mechatronics*. The Japan Society of Mechanical Engineers, 2020, pp. 1P2–K02.

[42] W. Felt, M. J. Telleria, T. F. Allen, G. Hein, J. B. Pompa, K. Albert, and C. D. Remy, "An inductance-based sensing system for bellows-driven continuum joints in soft robots," *Autonomous robots*, vol. 43, no. 2, pp. 435–448, 2019.

[43] Y. Ansari, M. Manti, E. Falotico, M. Cianchetti, and C. Laschi, "Multiobjective optimization for stiffness and position control in a soft robot arm module," *IEEE Robotics and Automation Letters*, vol. 3, no. 1, pp. 108–115, 2017.

[44] E. W. Hawkes, L. H. Blumenschein, J. D. Greer, and A. M. Okamura, "A soft robot that navigates its environment through growth," *Science Robotics*, vol. 2, no. 8, 2017.

[45] P. H. Nguyen, I. I. Mohd, C. Sparks, F. L. Arellano, W. Zhang, and P. Polygerinos, "Fabric soft poly-limbs for physical assistance of daily living tasks," in *2019 International Conference on Robotics and Automation (ICRA)*. IEEE, 2019, pp. 8429–8435.

[46] ——, "Fabric soft poly-limbs for physical assistance of daily living tasks," in *2019 International Conference on Robotics and Automation (ICRA)*. IEEE, 2019, pp. 8429–8435.

[47] "Older people's fall in daily life," https://www.caa.go.jp/policies/policy/consumer_safety/caution/caution_009/pdf/caution_009_180912_0001.pdf, Accessed: 2020-11-30.

[48] M. J. Parker, W. J. Gillespie, and L. D. Gillespie, "Effectiveness of hip protectors for preventing hip fractures in elderly people: systematic review," *Bmj*, vol. 332, no. 7541, pp. 571–574, 2006.

[49] L. Cianferotti, C. Fossi, and M. L. Brandi, "Hip protectors: are they worth it?" *Calcified tissue international*, vol. 97, no. 1, pp. 1–11, 2015.

[50] "Hip'safe by helite," https://senior.helite.com/en/, Accessed: 2020-11-30.

[51] S. Ahn, D. Choi, J. Kim, S. Kim, Y. Jeong, M. Jo, and Y. Kim, "Optimization of a pre-impact fall detection algorithm and development of hip protection airbag system," *Sensors and Materials*, vol. 30, no. 8, pp. 1743–1752, 2018.

[52] S. Yamamoto, E. Tanaka, Y. Kubouchi, T. Ikeda, K. Mizuno, A. Harada, and H. Okuizumi, "Biomechanical evaluations of hip fracture mechanism in pedestrian fall accident," *Transactions of the JSME*, vol. 72, no. 723, pp. 1799–1807, 2006.

[53] J. Nabeshima, M. Y. Saraiji, and K. Minamizawa, "Arque: artificial biomimicry-inspired tail for extending innate body functions," in *ACM SIGGRAPH 2019 Posters*, 2019, pp. 1–2.

[54] A. Maekawa, K. Kawamura, and M. Inami, "Dynamic assistance for human balancing with inertia of a wearable robotic appendage."

[55] F. Parietti and H. Asada, "Supernumerary robotic limbs for human body support," *IEEE Transactions on Robotics*, vol. 32, no. 2, pp. 301–311, 2016.

[56] "Lex by astride bionix," https://ja.lexbyastride.com/, Accessed: 2020-11-30.

[57] "Chairless chair," https://www.noonee.com/, Accessed: 2020-11-30.

[58] L. Quach, A. M. Galica, R. N. Jones, E. Procter-Gray, B. Manor, M. T. Hannan, and L. A. Lipsitz, "The nonlinear relationship between gait speed and falls: the maintenance of balance, independent living, intellect, and zest in the elderly of boston study," *Journal of the American Geriatrics Society*, vol. 59, no. 6, pp. 1069–1073, 2011.

[59] R. Ando, H. Matsuo, D. Matsuura, Y. Sugahara, and Y. Takeda, "Static analysis and design of extendable mechanism inspired by origami structure based on non-overconstrained kinematically equivalent mechanism," in *Symposium on Robot Design, Dynamics and Control*. Springer, 2020, pp. 521–529.

[60] V. Petuya, E. Macho, O. Altuzarra, C. Pinto, and A. Hernandez, "Educational software tools for the kinematic analysis of mechanisms," *Computer Applications in Engineering Education*, vol. 22, no. 1, pp. 72–86, 2014.

[61] "2018 national health and nutrition survey," https://www.mhlw.go.jp/content/000615344.pdf, Accessed: 2020-11-30.

[62] L. Zani, P. Erani, L. Grassi, F. Taddei, and L. Cristofolini, "Strain distribution in the proximal human femur during in vitro simulated sideways fall," *Journal of Biomechanics*, vol. 48, no. 10, pp. 2130–2143, 2015.

[63] E. Tanaka, S. Yamamoto, S. Ozeki, K. Mizuno, A. Harada, and M. Mizuno, "Biomechanical evaluations of hip fracture prevention by hip protector," *Transactions of the JSME*, vol. 70, no. 697, pp. 1193–1200, 2004.

[64] Y. Kubo, M. Yamaguchi, N. Oono, and T. Fukui, "Investigation of the validity of visual assessment of center of gravity in the analysis of posture and movement," *Journal of Japanese Physical Therapy Association*, vol. 33, no. 3, pp. 112–117, 2006.

[65] D. G. Thelen, L. A. Wojcik, A. B. Schultz, J. A. Ashton-Miller, and N. B. Alexander, "Age differences in using a rapid step to regain balance during a forward fall," *The Journals of Gerontology Series A: Biological Sciences and Medical Sciences*, vol. 52, no. 1, pp. M8–M13, 1997.

[66] "Hövding - airbag for urban cyclists," https://hovding.com/, Accessed: 2020-11-30.

[67] "hit-air - wearable airbag," https://www.hit-air.com/, Accessed: 2020-11-30.

[68] P. Vallabh and R. Malekian, "Fall detection monitoring systems: a comprehensive review," *Journal of Ambient Intelligence and Humanized Computing*, vol. 9, no. 6, pp. 1809–1833, 2018.

[69] N. Lapierre, N. Neubauer, A. Miguel-Cruz, A. R. Rincon, L. Liu, and J. Rousseau, "The state of knowledge on technologies and their use for fall detection: A scoping review," *International journal of medical informatics*, vol. 111, pp. 58–71, 2018.

[70] L. Ren and Y. Peng, "Research of fall detection and fall prevention technologies: A systematic review," *IEEE Access*, vol. 7, pp. 77 702–77 722, 2019.

Appendix

A.1 Displacement analysis of Origami Spring

As shown in Fig. A.1, the angles between lower plane and the unit triangles are defined as θ_i $(i = 1, 2, \ldots, n+1, n = 12)$. The points in the lower plane are denoted as L_i, the points in the upper plane as U_i. As for the coordinate axes, the origin is located at L_1, and the x axis is placed along $\overrightarrow{\mathrm{L}_1\mathrm{L}_2}$. The relation between the length of longitudinal side a and the lateral side b is expressed in the following equation:

$$b = a \tan\varphi \ (\varphi = \frac{\pi}{n}) \tag{A.1}$$

The coordinates of L_1, U_1, and L_2 are expressed with a and b as follows:

$$\mathrm{L}_1 = (0, 0, 0),\ \mathrm{U}_1 = (0, a\cos\theta_1, a\sin\theta_1),\ \mathrm{L}_2 = (b, 0, 0) \tag{A.2}$$

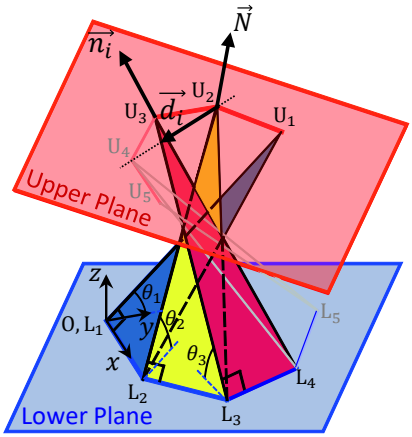

Figure A.1: Definition of each point, angle and vector

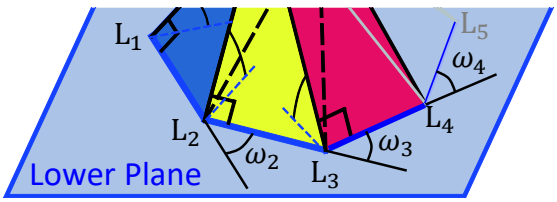

Figure A.2: Definition of ω_i

Here, the external angle between $\mathrm{L}_{i-1}\mathrm{L}_i$ and $\mathrm{L}_i\mathrm{L}_{i+1}$ is defined as ω_i $(i = 2, 3, \ldots, n)$ as shown in Fig. A.2. When $i = 2, 3$, the coordinates of U_i and L_{i+1} are expressed as in the following equations:

$$x_{\mathrm{U}_i} = x_{\mathrm{L}_i} - a\cos\theta_i \sin\left(\sum_{j=2}^{i}\omega_j\right),\ y_{\mathrm{U}_i} = y_{\mathrm{L}_i} + a\cos\theta_i\cos\left(\sum_{j=2}^{i}\omega_j\right),\ z_{\mathrm{U}_i} = a\sin\theta_i \tag{A.3}$$

$$x_{\mathrm{L}_{i+1}} = x_{\mathrm{L}_i} + b\cos\left(\sum_{j=1}^{i}\omega_j\right),\ y_{\mathrm{L}_{i+1}} = y_{\mathrm{L}_i} + b\sin\left(\sum_{j=1}^{i}\omega_j\right),\ z_{\mathrm{L}_{i+1}} = 0 \tag{A.4}$$

From Eq. (A.4) and $\|\overrightarrow{\mathrm{U}_{i-1}\mathrm{U}_i}\| = b$, the following equation is obtained:

$$\tan\varphi\cos\theta_i\sin\omega_i + \cos\theta_{i-1}\cos\theta_i\cos\omega_i = 1 - \sin\theta_{i-1}\sin\theta_i \tag{A.5}$$

The value of ω_i is obtained by solving Eq. (A.5) for ω_i using the R-Alpha method of trigonometric function, and the coordinates of U_i and L_{i+1} are determined. When the values of θ_1, θ_2 and θ_3 are given, the coordinates of L_1, L_2, L_3, L_4, U_1, U_2, and U_3 are determined. When the coordinates of U_1, U_2, and U_3 are determined, the normal vector of the upper plane $\overrightarrow{N}$ is obtained by $\overrightarrow{\mathrm{U}_1\mathrm{U}_2} \times \overrightarrow{\mathrm{U}_2\mathrm{U}_3}$. The other upper points should be in the upper plane. Based on this condition, the coordinates of U_i and L_{i+1} are calculated.

When $i \geq 4$, the coordinates of L_1, L_2, $\cdots$, L_i, U_1, U_2, $\cdots$, U_{i-1} have been already determined. Here, $\overrightarrow{n_i} = \overrightarrow{\mathrm{L}_i\mathrm{U}_{i-1}}$ is defined as shown in Fig. A.1, and this vector is the normal vector of the plane which the circle created by rotating the point U_i around $\overrightarrow{\mathrm{L}_i\mathrm{U}_{i-1}}$ is on. One of the intersections of the circle and the upper plane is the point U_{i-2} and the other is the point U_i. Here, the direction vector $\overrightarrow{d_i} = \overrightarrow{N} \times \overrightarrow{n_i}$ of the line of intersection of the circle and the upper plane is defined. The point T on the line of intersection is expressed with a parameter t as follows:

$$\overrightarrow{\mathrm{OT}} = \overrightarrow{\mathrm{OU}_{i-2}} + t\overrightarrow{d_i} \tag{A.6}$$

When $t = 0$, the point T becomes the point U_{i-2}, then $t \neq 0$. By finding the value of parameter t so that $\|\overrightarrow{\mathrm{TU}_{i-1}}\| = b$, the coordinate of U_i is determined. Using the

coordinate of U_i, Eqs. (A.3) and (A.5), the values of θ_i and ω_i are obtained. The coordinate of L_{i+1} is determined with the values of θ_i and ω_i and Eq. (A.4).

The coordinate of all points is obtained from three given angles θ_1, θ_2 and θ_3 by repeating this calculation process.

Acknowledgements

The author wish to acknowledge Alfonso Hernández, CompMech, Department of Mechanical Engineering, UPVEHU for the permission to use the GIM® software. (www.ehu.es/compmech). Comments, reports on bugs, and suggestions are welcomed here: erik.macho@ehu.es

A part of this work has been supported by the Grants-in-Aid for JSPS Fellows 18J21466, NSK Ltd. and The KAITEKI Institute, Inc.

First and foremost I am extremely grateful to my supervisor, Prof. Yukio Takeda, for his invaluable advice, continuous support, and patience during my six years of study in this laboratory. His immense knowledge and plentiful experience have encouraged me in all the time of my academic research and daily life. In addition, I am grateful to Prof. Yusuke Sugahara and Prof. Daisuke Matsuura for the assistance and inspiration from them in the discussion of my research and daily life.

I would like to thank Prof. Nobuyuki Iwatsuki, Prof. Gen Endo, and Prof. Hiraku Sakamoto for providing helpful feedback throughout the dissertation defenses.

I would also like to thank Prof. Hannes Bleuler and the members of The Laboratoire de Systèmes Robotiques at EPFL, Prof. Harry Asada and the members of The d'Arbeloff Laboratory at MIT, Prof. Alfonso Hernández and the members of CompMech research group at UPV/EHU for accepting my international stay and their hospitality. I learned a lot of things from the discussions and chats with them. Special thanks to Academy of Global Leadership for helping me to have a broader perspective of things.

I would like to thank Hiroko Takano and Taiko Ichinose for providing friendly and calm atmosphere in the Lab. I would also like to thank fellow lab mates for their help in the form of discussions, support and chats in daily life.

At last but most, I would like to thank my family and friends for their understanding and unconditional support.